Doctoral Dissertation

Thermoelectric and mechanical properties of Ag_2Te and $Sb_{1.6}Bi_{0.4}Te_3$

(Ag_2Te と $Sb_{1.6}Bi_{0.4}Te_3$ の熱電特性と機械的特性)

DOYOUNG JUNG

July 2013

Graduate School of Engineering

Osaka University

Thesis Advisors:

Professor Shinsuke Yamanaka, Ph.D.
Associate Professor Ken Kurosaki, Ph.D.

Yamanaka Laboratory, Division of Sustainable Energy and Environmental Engineering,
Graduate School of Engineering, OSAKA UNIVERSITY

Thesis Committee:

Professor Shinsuke Yamanaka, Ph.D.
Professor Takao Yamamoto, Ph.D.
Associate Professor Ken Kurosaki, Ph.D.
Associate Professor Hiroshi Nishikawa, Ph.D.

Graduate School of Engineering
OSAKA UNIVERSITY

TABLE OF CONTENTS

CHAPTER Page

CHAPTER Page

CHAPTER Page

CHAPTER I

Introduction

1.1 Background

As the industrial Revolution was begun in Britain at the middle of 18th century, Britain was transformed from a predominantly agricultural nation into the manufacturing workshop of the world. The emergence of machinery and factories made possible the mass-production of goods more rapidly and easily. Furthermore, rapid scientific and technological innovations, and expanding domestic and international markets led to the vitalization of Europe economy. Since the economic growth and scientific and technological development of Britain, the industrial Revolution was spread in France, Germany and America rapidly.

However, although the industrial Revolution started in Britain had positive effect on the industrial world, there is no doubt that it has wreaked havoc on an environment. For the operation of the steam engines and factories, they had to use a huge amount of coal, oil and natural gas. As a result, in the moment of 21st century, we are facing the serious environmental problems such as the depletion of nature resources, pollution, global warming caused by carbon CO_2 and all that sort of things. On a more serious note, about 90 % of world' energy consumption is still dependent on the fossil fuels even today.[1)]

According to Graus research, the average efficiencies of power generation are only 35% for coal, 45% for natural gas and 38% for oil-fired power generation,[2)] meaning that the rest of the energy is thrown out as a waste energy. Moreover, one of the most serious problems is that the burning of fossil fuels produces CO_2, which is released to the atmosphere. CO_2 concentration in the atmosphere have been increased about 41 % (2006) compared to the pre-industrial age (1870). At the same time the average temperature of the Earth has risen between 0.4 and 0.8 ℃ over the past 100 years. The increased CO_2 in the atmosphere influenced Earth's radiation balance,

resulted in a global warming and climate change.[3,4] The leaders of the main industrialized countries (G8) realized the seriousness of the climate disaster by global warming and held the Hokkaido Toyako Summit in July, 2008. All of the leaders vowed to "consider seriously" cutting greenhouse emissions by at least half by 2050.

The methods for the reduction of greenhouse emission can be broadly classified into two categories: (i) improvement of the efficiency of the existing fossil fuels, (ii) development of alternative energy sources and different types of energy conversion technology. The first method could be preferable plan from the viewpoint of not only but reducing the greenhouse emission also saving the fossil fuels. However, we know that the fossil fuels will be apparently depleted in the near future. According to the research of CIA world facebook, if we carry on at present consumption rate of the fossil fuels without any increase for growing population, oil deposits will be gone by 2052, and gas and coal deposits also will be depleted in 2060 and 2088 year, respectively.[5] Therefore, we should establish a long-term plan for the future by developing sustainable energy sources and different types of energy conversion technology for the environmental problems and the exhaustion of natural resources. In addition, since the meltdown of Fukushima Daiichi nuclear power plant in Japan on 2011 caused by the tsunami disaster, a development of safe and sustainable energy becomes top priority issue worldwide. One of the keys of resolving these problems is thermoelectric (TE) energy conversion technology, which can convert heat directly into electricity using a class of materials known as TE materials.[6-11] Home heating, automotive exhaust and industrial processes generate an huge amount of unused waste heat that could be convert to electricity by using thermoelectrics. Thermoelectrics are also capable of acting as solid state refrigerators or heat pumps which do not use any moving parts and they are silent, reliable, and scalable, making them ideal for small and distributed power generation.[7] For examples, application currently under study is harvesting an waste heat energy from the hot exhaust stream of cars.[12] Another interesting application uses thermoelectrics to enhance the combustion efficiency of wood stoves used in developing countries, decreasing smoke output and reducing the amount of wood needed to cook.[13] Thermoelectrics are also able to generate power from the sun by using solar energy to create a temperature difference across a thermoelectric material; this is known as solar thermal energy conversion.[14-17] Although thermoelectrics have such a great potential to apply in widespread application, practically speaking, TE devices are not used in common because of their low conversion efficiency and economic efficiency. However, thermoelectrics field has been achieved remarkable progress in

the middle of 1990s through nanostructured materials such as superlattices,[18] quantum dots,[19] nanowires,[20,21] and nanocomposites.[22–25] These TE materials could obtain large enhancements in the thermoelectric figure of merit which cannot be achieved in traditional bulk materials.[18–22] At the same time, complex bulk materials such as skutterudites,[26] clathrates[27] and Zintl phases[28] have been explored and found that high efficiencies could be obtained.[29] And the effort to improve TE performance is actively underway in the present.

In the present thesis, TE properties of polycrystalline bulks of Ag_2Te and $Sb_{1.6}Bi_{0.4}Te_3$ which are some of best TE materials known were studied. Moreover, mechanical properties of these materials also were investigated. I explain the details in each chapter.

1.2 Introduction of Thermoelectrics

1.2.1 Thermoelectric Phenomena

Thermoelectric (TE) phenomena were discovered in 1821 by Thomas Johann Seebeck. He described how a temperature gradient between two dissimilar materials induces a voltage difference across the junctions between them.[30] And this phenomena named as a Seebeck effect after that. As shown in Figure 1.1, the Seebeck effect occurs between the junctions of two dissimilar conductors when a temperature gradient is present. The Seebeck effect describes the establishment of a voltage gradient (dV_{12}) across a material in response to a temperature gradient

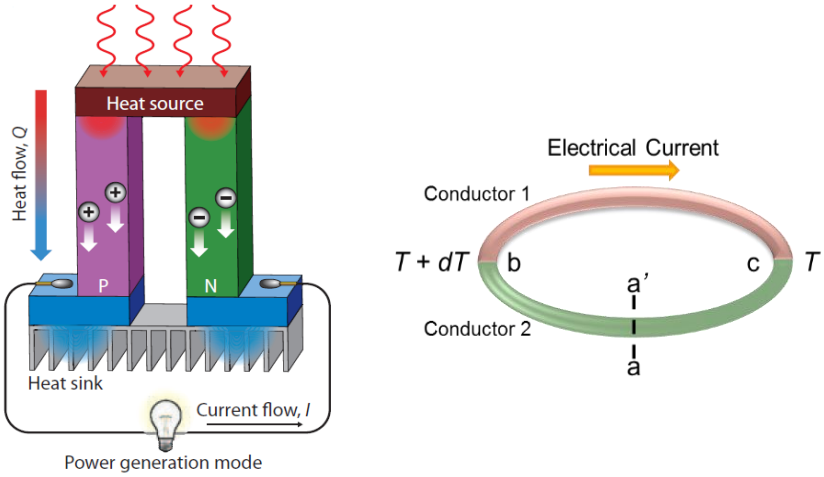

Figure 1.1 Schematic illustrations of a thermoelectric module for power generation and Seebeck effect. An applied temperature difference causes charge carriers in the material (electrons or holes) to diff use from the hot side to the cold side, resulting in current flow through the circuit.[31]

(*dT*) and the relation is described as following equation;

$$S_{12} = \frac{dV_{12}}{dT} \tag{1.1}$$

where S_{12} is the relative thermopower across the junction of the materials, called Seebeck coefficient. The temperature gradient causes a higher concentration of charge carriers at the cold side of the sample, which corresponds to the generation of a voltage differential across the sample. The sign of the Seebeck coefficient is typically negative for *n*-type electrical conduction, where electrons are the primary charge carriers, and positive for *p*-type conduction, where holes are the majority carriers.

Thermoelectric phenomena can be used in solid state cooling systems as another application. Jean Charles Athanase Peltier discovered in 1834 that an electrical current can cause temperature difference at the junction under isothermal conditions,[32] called Peltier effect and an illustration is shown in Figure 1.2. The Peltier coefficient (*Π*) is described as following equation;

$$\Pi_{12} = \frac{1}{I}\frac{dQ_{12}}{dt} \tag{1.2}$$

where, dQ_{12}/dt and I are the rate of heat transfer at the junction and the electrical current, respectively. When the voltage is applied in the right direction in Figure 1.2 across a p-n junction, the junction region is cooled. On the opposite end, energy releasing process occurs and heats the junction region. The dependence of the Peltier effect upon the current suggests a greater degree of control over the performance of a thermoelectric device than does the Seebeck effect, which

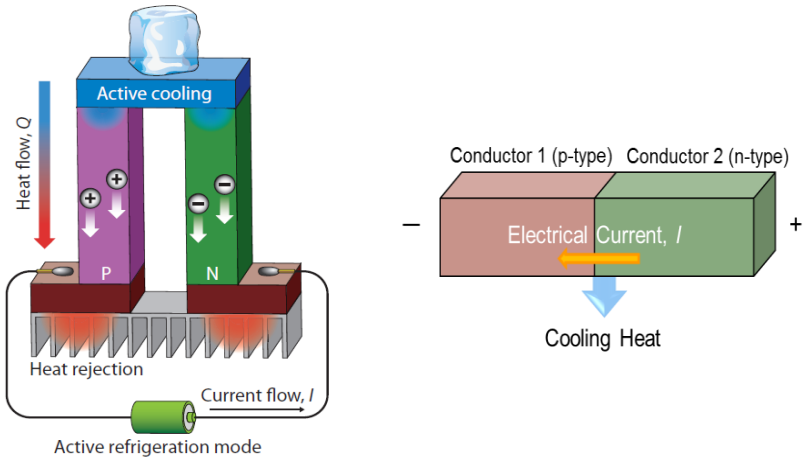

Figure 1.2 Schematic illustrations of a thermoelectric module for active refrigeration and Peltier effect. Heat evolves at the upper junction and is absorbed at the lower junction when a current is made to flow through the circuit.[31]

simply measures the tendency of a material for establishing a voltage gradient in response to a temperature gradient.

Finally, the Thompson effect describes the radiation or absorption of heat energy from a material that has both temperature and voltage gradients. The Thompson effect states that in the absence of Joule heating, the heat gained or lost is given by

$$\tau = \frac{dQ_{\Gamma}}{IdtdT} \tag{1.3}$$

where τ, Q, I, t and T are the Thomson coefficient, heat, electrical current, spatial coordinate and temperature, respectively. It should be noted that while the Seebeck and Peltier coefficients describe heat transfer in a system of two dissimilar materials, the Thompson effect describes heat flow in a single material. From the Thompson effect, it can be shown that

$$\tau_1 - \tau_2 = T\frac{dS_{12}}{dT} \tag{1.4}$$

and consequently that[33)]

$$\Pi_{12} = S_{12}T \tag{1.5}$$

The Thomson effect leads to a direct relationship between the Seebeck and Peltier coefficient.

1.2.2 The Figure of Merit and Conversion Efficiency

The efficiency of refrigeration modules is characterized by the coefficient of performance (C.O.P.) whereas the efficiency of power generation modules is described in terms of the efficiency of a heat engine. In either case, it is possible to relate the expressions describing the efficiency to a parameter that contains the relevant thermal, electrical, and thermoelectric parameters, the tuning of which is at the center of research into thermoelectric materials. The relation of this parameter, the figure of merit, to the coefficient of performance and heat engine efficiency is outlined here. The coefficient of performance, ϕ, is related to the total heat flow, dQ/dt, and the power input, P, as following equation;

$$\phi = \frac{1}{P}\frac{dQ}{dt} \tag{1.6}$$

where Q is the sum of heat flow due to the thermal conductance of the material, Q_{κ}, the Peltier heat flow, Q_{Π}, and the heat loss due to Joule heating, Q_{I}. That is

$$Q = Q_{\kappa} + Q_{\Pi} + Q_I \text{, where } \; Q_{\kappa} = -K\Delta T \text{, } Q_{\Pi} = I\Pi = IST \text{ and } Q_I = -I^2R \tag{1.7}$$

K is the thermal conductance.

The power supplied to the device is given simply by the Joule expression,

$$P = I^2 R \tag{1.8}$$

such that the coefficient of performance (C.O.P.) becomes

$$\phi = \frac{-K\Delta T + IST - I^2 R}{I^2 R} \tag{1.9}$$

Maximizing the C.O.P. requires, by differential calculus, that $d\phi/dt$ goes to zero at some value of I, denoted Imax. The result is that

$$I_{\max} = \frac{2K\Delta T}{ST} \tag{1.10}$$

and substituting this value back into equation (1.12) gives, after some simplification,

$$\phi(I_{\max}) = \frac{\frac{S^2 T^2}{RK} - 4\Delta T}{4\Delta T} \tag{1.11}$$

The only intrinsic material properties that equation (1.11) depends upon are those in the first term of the numerator, namely the thermopower, S, the thermal conductance, K and the resistance, R. It is customary to define a new quantity, the figure of merit, Z, as

$$Z \equiv \frac{S^2}{\rho\kappa} \tag{1.12}$$

replacing resistance and thermal conductance with the dimension-scaled quantities of resistivity, ρ and thermal conductivity, κ. Dimensional analysis of equation (1.12) shows the dimensions to be T^{-1}, and as such it is more common to refer to the dimensionless figure of merit, or ZT, which is given by

$$Z = \frac{S^2}{\rho\kappa} T \tag{1.13}$$

The figure of merit is also found in the expression for the efficiency of a heat engine, although the derivation is not a simple. The efficiency of a heat engine is given by the well-known formula

$$\eta = \frac{W}{dQ/dt} \tag{1.14}$$

where W is the work done by the engine and dQ/dt is the heat flow through the engine. The work done by the device is the contribution from the Seebeck voltage minus a Joule heating term:

$$W = IV_{tot} = I\Delta V_{seebeck} - I\Delta V_R = IS\Delta T - I^2 R \tag{1.15}$$

The expression for heat flow differs from the case of active refrigeration in that heat

flow by diffusion and by the Peltier effect are now cumulative, opposed only by Joule heating effects. That is,

$$Q = K\Delta T + IST - I^2R \tag{1.16}$$

Thus, the efficiency can be expressed as

$$\eta = \frac{IS\Delta T - I^2R}{K\Delta T + IST - I^2R} \tag{1.17}$$

and it will also have a maximum value for some I_{max}, which is obtained by setting the first derivative of η equal to zero and solving for I. After some simplification, the result is that

$$I_{max} = \frac{S\Delta T}{R\left(\sqrt{1+\left(\frac{S^2}{RK}\right)T}+1\right)} \tag{1.18}$$

where the figure of merit, Z, is found in the denominator. Substituting into equation (1.17) yields η (Z), which, after a bit of algebra, can be reduced to

$$\eta_{max} = \frac{T_H - T_C}{T_H}\frac{\sqrt{1+ZT}-1}{\sqrt{1+ZT}+T_C/T_H} \tag{1.19}$$

which again depends on the intrinsic properties of the material entirely through the figure of merit, Z [29]. As $Z \to \infty$, the expression for the efficiency given in equation (1.19) approaches the Carnot limit. Note that while the above derivations are carried out for a single segment of a thermoelectric module, the results will not be changed if the calculation were to be carried out across the entire module. These calculations also assume that there is no heat extraction from the segments due to the Thompson effect.

The relation between η_{max} and ZT is plotted in Figure 1.3 in the case of T_C = 300 K. To reach higher thermoelectric efficiency, larger temperature difference and higher Z value is essential. Devices with ZT > 1 ~ 1.5 have advantage to achieve the efficiency of η > 10 % when the T_H = 500 and 600K, from the view of commercial use. These values are quite competitive with existing engines and mechanical coolers, and are therefore good marks to shoot for in terms of research and engineering effort versus return on investment.

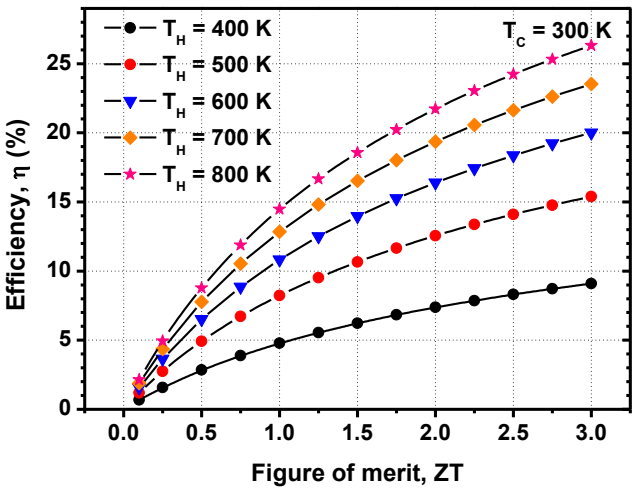

Figure 1.3 Thermoelectric energy conversion as a function of *ZT* at the setting of T_c=300 K.

The best TE materials currently used in devices are Bi_2Te_3-based alloys having a maximum *ZT* of about 0.8. A *ZT* of 0.8, which translates to an energy conversion efficiency of several percent calculated by using equation (1. 19), was a practical upper limit for bulk materials established in the 1960s. However, the conversion efficiency needs to be improved for the practical use of TE materials. As shown in Figure 1.4, the aim in internal combustion engine is to convert about 10 % of the waste heat to usable energy in the present.

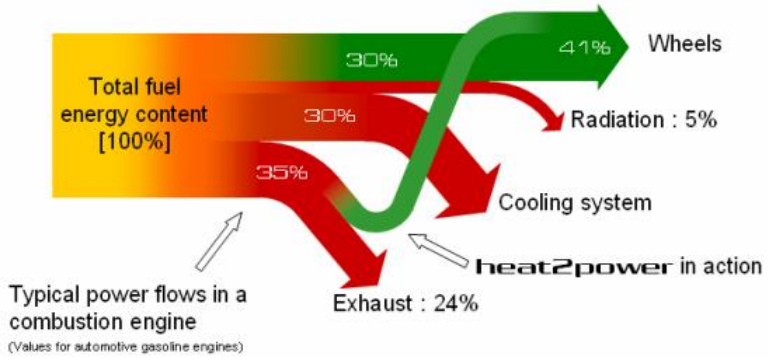

Figure 1.4 Energy flow path in internal combustion engine.[34)]

1.2.3 Optimization of Thermoelectric Figure of Merit

In a semiconductor the values of the Seebeck coefficient, the electrical conductivity, and the thermal conductivity are related to one another since they are functions of the free charge carrier concentration. As shown in Figure 1.5, the Seebeck coefficient decreases while the

electrical conductivity increases with increasing concentration of charge carriers. This accounts for the maximum in $S^2\sigma$, which is called the power factor and the numerator of *ZT*, when plotted as a function of *n*. From the slops, developing a high TE power factor and therefore *ZT*, needs to have a large Seebeck coefficient (found in low carrier concentration semiconductors or insulators) and a large electrical conductivity (found in high carrier concentration metals).

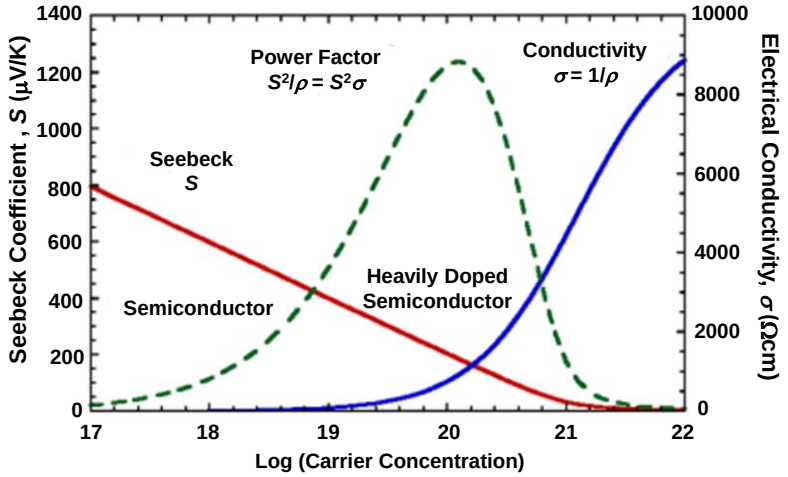

Figure 1.5 Power factor as a function of carrier concentration.

The thermoelectric power factor maximizes somewhere between a metal and semiconductors. Good thermoelectric materials are typically heavily doped semiconductors with carrier concentration of 10^{19} to 10^{21} carriers/cm^3. To ensure that the net Seebeck effect is large, there should only be a single type of carrier. Mixed *n*-type and *p*-type conduction will lead to opposing Seebeck effect and low thermopower.[26)]

1.3 Current Research in Thermoelectrics

1.3.1 Low Dimensional Effects

For the development of TE materials with enhanced performance, it is important to control the interconnected physical parameters Seebeck coefficient, electrical resistivity and thermal conductivity in a crystalline system. Nanostructures provide a chance to disconnect the linkage between thermal and electrical transport by introducing some new scattering mechanisms for *ZT* enhancement. There are some reviews focusing on nanocrystalline[35)] and nanostructured

thermoelectric materials[36] and interfaces in bulk thermoelectric materials[37]. Reducing the dimensions offers a new possibility to individually tune the TE parameters. When the system size decreases and approaches a scale comparable to the feature length of electron behavior (*e.g.* mean free path, wavelength) in any direction, the DOS is increased significantly due to quantum confinement, resulting in the enhancement of the Seebeck coefficient. The quantum confinement approach is trying to increase the thermoelectric power factor through an increase of the electronic DOS near the Fermi level. This is accomplished by making the size scale of the material comparable to the spatial extent of the electronic wave function confining the electrons in one or more dimension. If electron scattering is assumed to be energy independent (*i.e.* $\mu(E) = \mu$), then the electrical conductivity is directly proportional to the DOS.[38] According to the Mott–Jones relation, which is only strictly valid in the case of metals and highly degenerate semiconductors, this would result in enhancement of the thermopower by increasing the slope of the DOS at the Fermi level: [39]

$$S = \frac{\pi^2}{3}\frac{k^2 T}{e}\left(\frac{\partial \log\sigma(E)}{\partial E}\right)_{E=E_F} \tag{1.20}$$

$$S = \frac{8\pi^2 k_B^2}{3eh^2} m^* T\left(\frac{\pi}{3n}\right)^{\frac{2}{3}} \tag{1.21}$$

A sharply changing DOS implies the increased influence of carriers having relatively flat dispersion behavior, thus the origin of the increase in thermopower could alternatively be thought of as increase in the carrier effective mass. It is well known that low-dimensional, quantum-confined systems exhibit sharp, nearly dispersionless bands as shown in Figure 1.6, and appropriate size tuning to place these bands near the Fermi level could enable a marked increase in thermopower. Although this approach appears promising for enhancing *ZT*, quantum confinement can be difficult to achieve due to the small confinement length requirements in many materials, potentially limiting the ability of this route to enhance *ZT*. However, similar approaches in bulk materials involving the introduction of dopants having appropriate resonant levels appear to have been more successful.

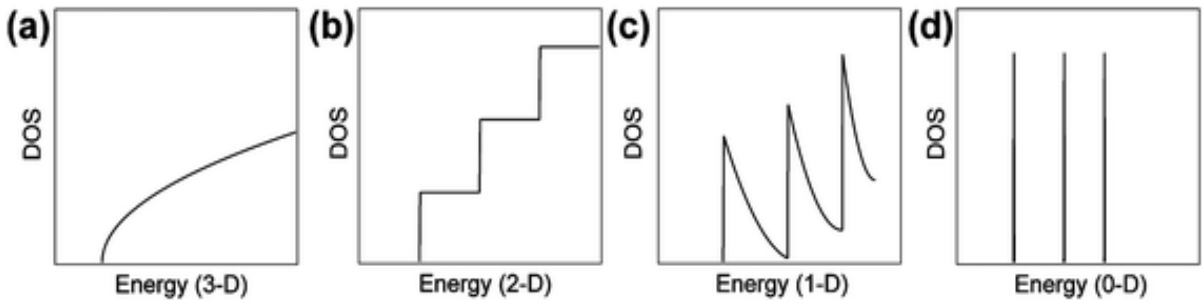

Figure 1.6 Schematic illustration of the density of states (DOS) as a function of energy for: (a) a bulk material (3-D), (b) a quantum well (2-D), (c) a nanowire (1-D), and (d) a quantum dot (0-D). The DOS at the band edge increases with decreasing dimension.

Meanwhile, the thermal conductivity is also reduced because the surface strongly scatters the propagation of phonons, as any dimension is less than the average free path of phonons. For example, Bi_2Te_3-based films prepared by pulsed laser deposition show κ values of 0.3–0.4 W m^{-1} K^{-1}, which are 25% lower than in the bulk.[40] It has also been reported that a silicon nanowire with a diameter of 10–20 nm presents amazingly low thermal conductivity with a $\kappa_{bulk}/\kappa_{nanowire}$ ratio of as high as 25–150 near room temperature.[41,42]

1.3.2 Nanocomposites

As I already mentioned in previous chapter, nanostructured TE materials have a great advantages for increasing the power factor and reducing the lattice thermal conductivity, simultaneously. However, the increased grain boundaries often have a minor effect on the carrier mobility. Considering this balance between the phonon scattering and carrier mobility caused by the grain boundaries, a nanocomposite TE material which is a composite constructed by incorporating some form of nanostructure into a bulk material might provide better TE performance compared with monolithic coarse- or fine-grained samples.[43,44] In this nanocomposite, the dispersed nanoparticles play a role in scattering the phonon, while the charge carriers have a less influence on the nanoparticles than the phonon.

Obvious *ZT* improvement have been obtained in (Zr,Hf)NiSn half-Heusler alloys with nano-ZrO_2 due to the significant reduction of lattice thermal conductivity as shown in Figures 1.7(a) and (b).[45] It is also reported that more significant enhancements can be achieved by embedding metal or conductive nanoparticles into a TE material matrix: examples include Pb and Sb in PbTe[46], Sb in $Yb_yCo_4Sb_{12}$[48] and ErAs in $In_{0.53}Ga_{0.47}As$.[49] This kind of nanoscale dispersed

phase can be located at the grain boundary or within the grains.

A current challenge in the development of nanocomposite TE materials is how to preserve the nanostructures within the bulk composite and prevent aggregation and interparticle growth. The solution to these issues significantly depends on the interfaces. A suitable interface could prohibit undesired grain boundary growth and interdiffusion, as well as selectively scattering phonons and charge carriers, potentially resulting in a considerably enhancement of *ZT* values.

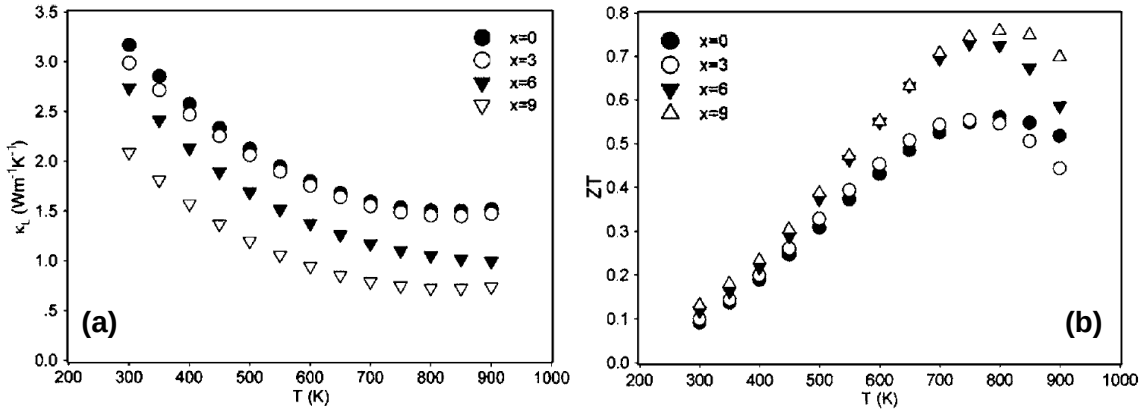

Figure 1.7 Temperature dependence of (a) κ_{lat} and (b) *ZT* for (Zr,Hf)NiSn containing x vol % ZrO_2 nanoinclusions.[45)]

1.3.3 Reducing the Bipolar Effect

The major purpose of nanocomposites has been a reduction of lattice thermal conductivity. However, the lattice thermal conductivity of nanocomposites now is very low level. Thus, the other contributions to the thermal conductivity such as the electrical thermal conductivity and the bipolar thermal conductivity need to be reduced. Figure 1.8 shows the calculated temperature dependence of the total, lattice, electronic, and bipolar thermal conductivities for heavily doped bulk *n*-type $Si_{80}Ge_{20}$.[52)] According to increase temperature, the contributions of electrical and the bipolar thermal conductivity account for about 50 % of total thermal conductivity.

The bipolar effect is due to the fact that there are two types of carriers, electrons and holes. At high temperature many electrons are thermally excited from the valence band to the conduction band, leaving behind an equal number of holes. The presence of these two types of

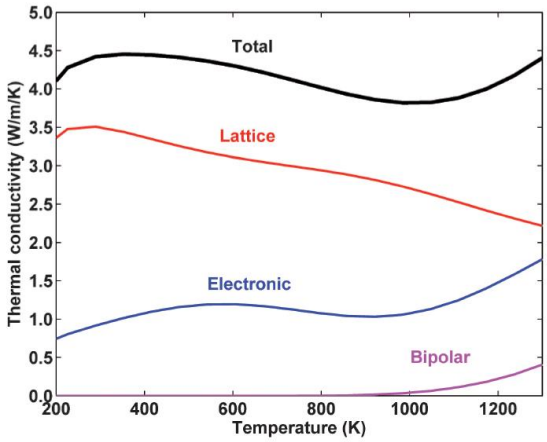

Figure 1.8 The calculated temperature dependence of the total, lattice, electronic, and bipolar thermal conductivities for heavily doped bulk *n*-type $Si_{80}Ge_{20}$.[52)]

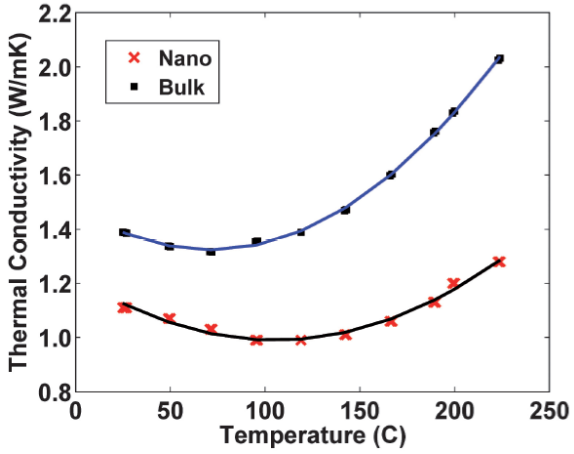

Figure 1.9 Total thermal conductivity of a $Bi_xSb_{2-x}Te_3$ nanocomposite.[22,52)] A nanocomposite sample shows relatively low thermal conductivity at high temperature compared to bulk sample.

carriers allows heat conduction to take place even if the net electrical current is zero.[6)] While many TE materials are usually so highly doped that this effect is not strong, for some materials at elevated temperature the bipolar thermal conductivity can be a significant component of the total thermal conductivity. The way to reduce the bipolar effect is to somehow affect only the minority carrier. One possible way is to create a nanostructured TE material. The reduced bipolar effect was observed in a $Bi_xSb_{2-x}Te_3$ nanocomposite alloy,[22)] and modeling indicates that the electrons in *p*-type $Bi_xSb_{2-x}Te_3$ are more strongly scattered by the grain boundaries than the holes, resulting in a decreased electron contribution to the transport properties. Figure 1.9 shows the thermal conductivity of $Bi_xSb_{2-x}Te_3$ nanocomposite in which the total thermal conductivity maintains low

value at high temperature. As a result, the $Bi_xSb_{2-x}Te_3$ nanocomposite can sustain high *ZT* values over the whole temperature range.

However, unfortunately, the reason why electrons are preferentially scattered is currently being under study. Further enhancing this preferential scattering requires detailed knowledge of the electron and hole scattering processes at grain boundaries in TE materials. If this technique can be better understood and improved, it will be a powerful way to maintain a high *ZT* at elevated temperatures.[52)]

1.3.4 Increasing the Carrier Mobility

The electrical properties could be enhanced by reducing the impact of grain boundaries or interfaces on electron transport. The theoretical prediction for the grain boundary region showed that grain boundaries have a minor effect on the mobility at high doping levels,[49–51)] however in practical the mobility showed often substantially reducing. Figure 1.10 represents the

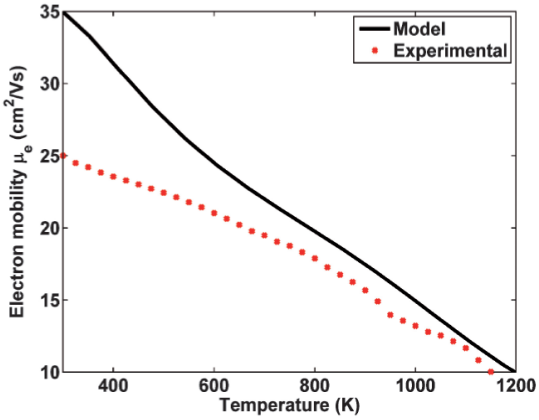

Figure 1.10 Theoretical prediction and experimental results for the mobility of *n*-type nano-$Si_{80}Ge_{20}$.[48)]

electron mobility of heavily doped nanostructured *n*-type $Si_{80}Ge_{20}$ obtained from theoretical prediction and experimental results.[52)] As seen in Figure 1.10, the experimental mobility is about 40 % lower than that of theoretical expectation at room temperature. If it is possible for the mobility to be restored to near the theoretical value, *ZT* could be increased by up to 40 %. The Kanatzidis group recently made progress towards this goal with the introduction of synergistic nanostructuring.[46)] They found that nanostructured PbTe with encapsulated nanodots made of both Pb and Sb has an increased mobility over that of the bulk PbTe, resulting in a *ZT* a factor of

two larger than that of bulk PbTe. This increase in mobility only occurs when both Pb and Sb are present together in the nanoparticle. So far there has been no explanation for this effect, but their result gives hope that a similar effect is possible in other material systems.

1.4 Purpose of Present Study

Since the concept of low dimensional nanostructured TE materials was introduced in the 1990s, many different material systems have broken the $ZT = 1$ barrier which was the maximum ZT of any materials for over 50 years. The main reason for the remarkable achievement in ZT is due to the fact that both an improvement in the Seebeck coefficient and a reduction in lattice thermal conductivity are possible in nanostructure. Nanostructuring of TE materials played an important role in taking a new leap forward from the stagnant TE technology for last 50 years and there is no doubt that the nanostructuring has enormous potential for development continuously.

However ironically, since most research is focused on the nanostructuring, a new concept of research for improving TE performance is relatively insufficient. In addition, as I already mentioned in chapter 1.3.1 and 2, quantum confinement can be difficult to achieve due to the small confinement length requirements in many materials and as for nanocomposite, nanoparticle tend to be aggregated during the synthesis process, leading to degradation of carrier mobility.

The major purpose of present thesis can be broadly classified into three categories. First, I challenged on a concept of the wall of ion conduction to reduce lattice thermal conductivity selectively as an alternative to nanostructuring though Ag_2Te which is well-known for a good performance of TE material as well as an ion conductor. I investigated the effect of moving Ag ions on the phonon transport behavior in Ag_2Te. Second, I focused on a nanocomposite composed of Au nanoparticles and BiSbTe which is one of the best TE materials known for application around room temperature. I attempted a new method to synthesize a complete nanocomposite using γ-ray irradiation, in which Au nanoparticles are dispersed uniformly without aggregation in the BiSbTe matrix phase and investigate the effect of the Au nanoparticles dispersed uniformly in BiSbTe matrix on the lattice thermal conductivity and Seebeck coefficient. Lastly, compatibility of these materials was investigated by measuring mechanical properties such as thermal expansion and hardness. Although the mechanical properties of TE materials are important as much as TE properties in terms of stability in TE device, there is lack of research.

The experimental results and discussion are explained in the following each chapter.

1.5 References

1) U. S. Energy Information Administration (2010).
2) W. H. J. Graus, M. Voogt, and E. Worrell, Energy Policy **35,** 3936 (2007).
3) H. Fischer, M. Behrens, M. Bock, U. Richter, J. Schmitt, L. Loulergue, J. Chappellaz, R. Spahni, T. Blunier, M. Leuenberger and T. F. Stocker, Nature **452,** 864 (2008).
4) J. Lelieveld, S. Lechtenböhmer, S. S. Assonov, C. A. M. Brenninkmeijer, C. Dienst, M. Fischedick and T. Hanke, Nature **443,** 405 (2006).
5) All fossil fuel reserve and consumption data from CIA World Facebook.
6) G. S. Nolas, J. Sharp, and H. Goldsmid, Thermoelectrics: Basic Principles and New Materials Developments, Springer, New York, (2001).
7) D. Rowe, ed., Thermoelectrics Handbook: Macro to Nano, CRC Press Boca Raton, (2006).
8) T. M. Tritt and M. A. Subramanian, MRS Bull. **31**, 188 (2006).
9) T. M. Tritt, ed., Recent Trends in Thermoelectric Materials Research, in Semiconductors and Semimetals, Academic Press, San Diego, (2001).
10) G. Chen, M. S. Dresselhaus, G. Dresselhaus, J. P. Fleurial and T. Caillat, Int. Mater. Rev. **48**, 45 (2003).
11) M. Dresselhaus, G. Chen, M. Y. Tang, R. G. Yang, H. Lee, D. Z. Wang, Z. F. Ren, J. P. Fleurial and P. Gogna, Adv. Mater. **19**, 1043 (2007).
12) J. Yang, in 24th International Conference on Thermoelectrics, (2005).
13) http:///www.research.philips.com/newscenter/archive/2006/060227-woodstove.html. (2008).
14) H. Scherrer, L. Vikhor, B. Lenoir, A. Dauscher and P. Poinas, J. Power Sources **115**, 141 (2003).
15) H. Xi, L. Luo and G. Fraisse, Renewable Sustainable Energy Rev. **11**, 923 (2007).
16) S. Maneewan, J. Hirunlabh, J. Khedari, B. Zeghmati and S. Teekasap, Sol. Energy **78**, 495 (2005).
17) S. Maneewan, J. Khedari, B. Zeghmati, J. Hirunlabh and J. Eakburanawat, Renewable Energy **29**, 743 (2004).
18) R. Venkatasubramanian, E. Siivola, T. Colpitts and B. O'Quinn, Nature **413**, 597 (2001).
19) T. C. Harman, P. J. Taylor, M. P. Walsh and B. E. LaForge, Science **297**, 2229 (2002).
20) A. I. Hochbaum, R. Chen, R. D. Delgado, W. Liang, E. C. Garnett, M. Najarian, A. Majumdar and P. Yang, Nature **451**, 163 (2008).
21) A. I. Boukai, Y. Bunimovich, J. Tahir-Kheli, J.-K. Yu, W. A. Goddard Iii and J. R. Heath,

Nature **451**, 168 (2008).

22) B. Poudel, Q. Hao, Y. Ma, Y. Lan, A. Minnich, B. Yu, X. Yan, D. Wang, A. Muto, D. ashaee, X. Chen, J. Liu, M. S. Dresselhaus, G. Chen and Z. Ren, Science **320**, 634 (2008).
23) Y. Ma, Q. Hao, B. Poudel, Y. Lan, B. Yu, D. Wang, G. Chen and Z. Ren, Nano Lett. **8**, 2580 (2008).
24) X. W. Wang, H. Lee, Y. C. Lan, G. H. Zhu, G. Joshi, D. Z. Wang, J. Yang, A. J. Muto, M. Y. Tang, J. Klatsky, S. Song, M. S. Dresselhaus, G. Chen and Z. Ren, Nano Lett. **93**, 193121 (2008).
25) G. Joshi, H. Lee, Y. Lan, X. Wang, G. Zhu, D. Wang, R. W. Gould, D. C. Cuff, M. Y. Tang, M. S. Dresselhaus, G. Chen and Z. Ren, Nano Lett. **8**, 4670 (2008).
26) C. Uher, in Thermoelectric Materials Research I (ed. T. Tritt)139-253 (Semiconductors and Semimetals Series 69, Elsevier, 2011).
27) G. S. Nolas, J. Poon and M. Kauzlarich, Mater. Res. Soc. Bull. **31**, 199 (2006).
28) S. M. Kauzlarich, S. R. Brown and G. J. Snyder, Dalton trans. 2099 (2007).
29) G. J. Snyder and E. S. Toberer: Nat. Mater. **7**, 105 (2008).
30) T. J. Seebeck: Magnetische Polarisation der Metalle und Erze durch Temperatur - Differenz (Wilhelm Engelmann, Leipzig, 1895)
31) J. Li, W. Liu, L. Zho and M. Zhou, NPG Asia Mater. **2**, 152 (2010).
32) L.M. Goncalves and J.G. Rocha: Solid State Circuits Technologies (Intech, Rijeka, 2010).
33) G. S. Nolas, J. Sharp, and H. J. Goldsmid. Thermoelectrics: Basic Principles and New Materials Developments (Springer, Berlin, 2001).
34) http://www.heat2power.net/en__scope.php
35) P. Pichanusakorn, and P. Bandaru, Mater. Sci. Eng. R **67**, 19 (2010).
36) D. L. Medlin, G. J. Snyder, Curr. Opin. Colloid & In. **14**, 226 (2009).
37) J. R. Sootsman, D. Y. Chung and M. G. Kanatzidis, Angew. Chem., Int. Ed. **48**, 8616 (2009).
38) N. F. Mott and H. Jones, The Theory of the Properties of Metals and Alloys (Dover Publications, New York, 1958).
39) R. S. Makala, K. Jagannadham and B. C. Sales, J. Appl. Phys **94**, 3907 (2003).
40) A. I. Hochbaum, et al., Nature **451**, 163 (2008).
41) A. I. Boukai et al., Nature **451**, 168 (2008).
42) J. L. Mi, X. B. Zhao, T. J. Zhu and J. P. Tu, Appl. Phys. Lett. **91**, 172116 (2007).
43) L. D. Zhao, B.-P. Zhang, W.-S. Liu and J.-F. Li, J. Appl. Phys. **105**, 023704 (2009).

44) L. D. Chen, X. Y. Huang, M. Zhou, X. Shi and W. B. Zhang, J. Appl. Phys. **99**, 064305 (2006).
45) J. Sootsman, H. Kong, C. Uher, J. D'Angelo, C. I. Wu, T. Hogan, T. Caillat and M. Kanatzidis, Angew. Chem., Int. Ed. **47**, 8618 (2008).
46) H. Li, X. Tang, X. Su and Q. Zhang, Appl. Phys. Lett. **92**, 202114 (2008).
47) W. Kim et al., Phys. Rev. Lett. **96**, 045901 (2006).
48) C. R. M. Grovenor, J. Phys. C: Solid State Phys. **18**, 4079 (1985).
49) J. Y. W. Seto, J. Appl. Phys. **46**, 5247 (1975).
50) T. I. Kamins, J. Appl. Phys. **42**, 4357 (1971).
51) A. J. Minnich, M. S. Dresselhaus, Z. F. Ren and G. Chen, Energy Environ. Sci. **2**, 466 (2009).
52) J. Capps, F. Drymiotis, S. Lindsey and T. M. Tritt: Philos. Mag. Lett. **90**, 677681 (2010).

CHAPTER II

Experimental Methods

2.1 Synthesis and Characterization Methods

All experiments in this chapter were carried out in our Yamanaka lab at Osaka University. In the present study, the polycrystalline bulk samples were prepared by a traditional solid-state reaction or mechanical alloying, followed by hot-pressing. And their crystal structures, microstructures, thermoelectric and mechanical properties were examined by the X-ray powder diffraction (XRD), field emission scanning electron microscopy (FE-SEM), energy dispersive X-ray spectrometry (EDX), ZEM-1, Laser flash method, Hall effect and dilatometer. The basic principle of such synthesis and characterization methods will be covered in this chapter.

2.1.1 Mechanical Alloying

Mechanical alloying (MA) is a powder processing technique that allows production of homogeneous materials starting from blended elemental powder mixtures. MA process can be used to produce nanomaterial by ball-milling which repeats bonding, fracturing and rebonding of elemental. Once trapped between the balls, solid material is subjected to an external pressure causing a sequence of deformations which starts with reversible elastic deformations followed by irreversible plastic deformations, such as shear and twist deformations[1)] as shown in Figure 2.1. Microstructurally, the MA process can be divided into four stages: (i) initial stage, (ii) intermediate stage, (iii) final stage, and (iv) completion stage.

(i) At the initial stage of ball milling, the powder particles are flattened by the compressive forces due to the collision of the balls. Micro-forging leads to changes in the shapes of individual particles, or cluster of particles being impacted repeatedly by the milling balls with high kinetic energy. However, such deformation of the powders shows no net change in mass.

(ii) At the intermediate stage of the mechanical alloying process, significant changes occur in comparison with those in the initial stage. Cold welding is now significant. The intimate mixture of the powder constituents decreases the diffusion distance to the micrometer range. Fracturing and cold welding are the dominant milling processes at this stage. Although some dissolution may take place, the chemical composition of the alloyed powder is still not homogeneous.

(iii) At the final stage of the mechanical alloying process, considerable refinement and reduction in particle size is evident. The microstructure of the particle also appears to be more homogenous in microscopic scale than those at the initial and intermediate stages. True alloys may have already been formed.

(iv) At the completion stage of the mechanical alloying process, the powder particles possess an extremely deformed metastable structure. At this stage, the lamellae are no longer resolvable by optical microscopy. Further mechanical alloying beyond this stage cannot physically improve the dispersoid distribution. Real alloy with composition similar to the starting constituents is thus formed.

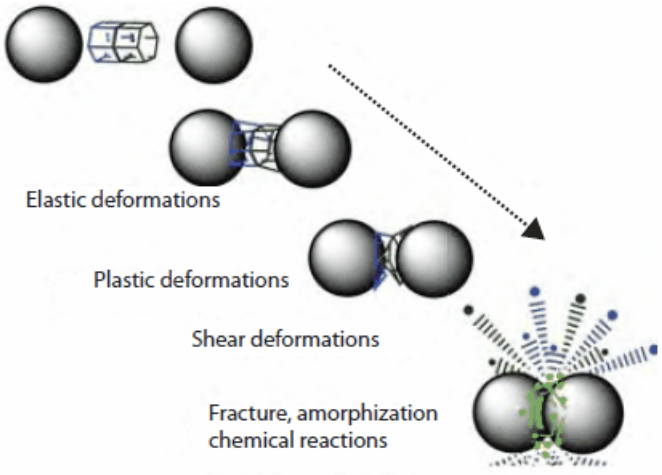

Figure 2.1 Schematic illustration of the deformation process in the material trapped between two colliding balls during milling.[2)]

2.1.2 Hot Pressing

The powder samples were hot-pressed and densified using a hot-pressing procedure. The sample powder is first cold-pressed into a pellet, which is then put into the graphite die to be heated by a furnace and pressed by upper punch as shown in Figure 2.2. The sintering

temperature, pressure, duration and relative density of the hot-pressed bulk samples are listed in each chapter.

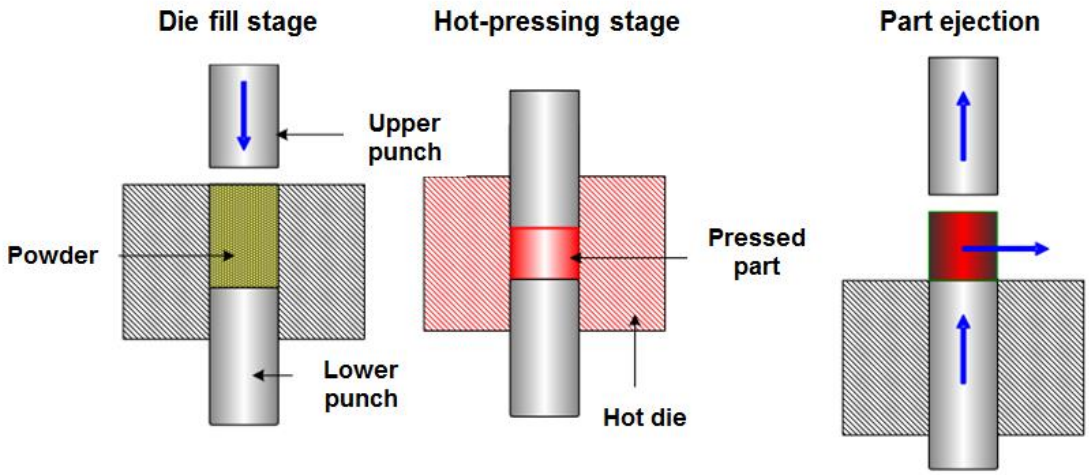

Figure 2.2 Schematic illustration of hot-pressing method.

2.1.3 X-ray Powder Diffraction

The samples were characterized using powder X-ray diffraction (XRD, Rigaku RINT2000) using Cu $K\alpha$ radiation at room temperature (λ= 1.5406 Å). The lattice parameter, unit cell volume and theoretical density were basically estimated from the XRD results. Since most materials have unique diffraction patterns, compounds can be identified by using a database of diffraction patterns. The purity of a sample can also be determined from its diffraction pattern, as well as the composition of any impurities present. X-rays are partially scattered by atoms when they strike the surface of a crystal. The part of the X-ray that is not scattered passes through to the

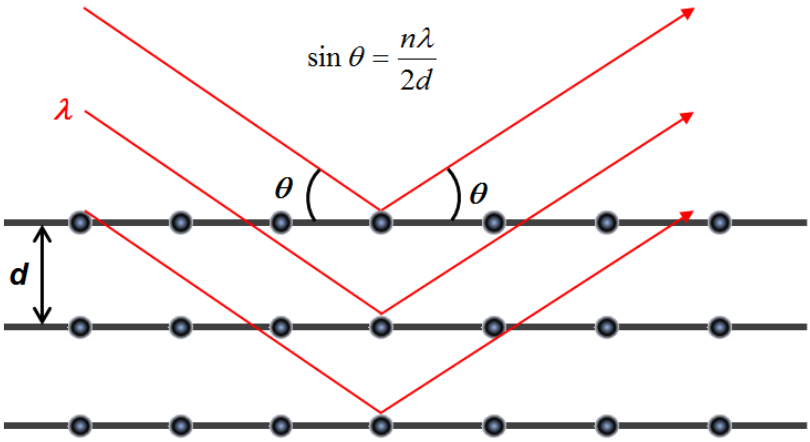

Figure 2.3 Schematic illustration of X-ray diffraction by atoms. The θ, n, λ, and d are the angle of incidence of the X-ray, integer, wavelength, and spacing between atom layers, respectively.

next layer of atoms, where again part of the X-ray is scattered and part passes through to the next layer as described in Figure 2.3. This causes an overall diffraction pattern, similar to how a grating diffracts a beam of light. In order for an X-ray to diffract the sample must be crystalline and the spacing between atom layers must be close to the radiation wavelength. If beams diffracted by two different layers are in phase, constructive interference occurs and the diffraction pattern shows a peak, however if they are out of phase, destructive interference occurs appear and there is no peak. Since a highly regular structure is needed for diffraction to occur, only crystalline solids will diffract; amorphous materials will not show up in a diffraction pattern.

A powder X-ray diffractometer consists of an X-ray source, a sample stage, a detector and a way to vary angle θ. The X-ray is focused on the sample at some angle θ, while the detector opposite the source reads the intensity of the X-ray it receives at 2θ away from the source path. The incident angle is than increased over time while the detector angle always remains 2θ above the source path.

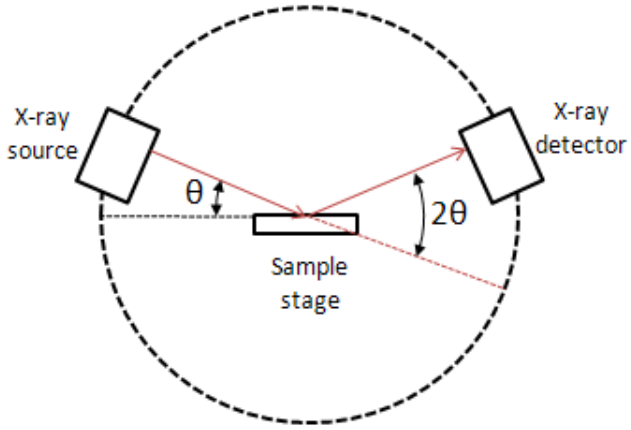

Figure 2.4 Schematic illustration of X-ray diffracting apparatus.

2.1.4 Morphology of Surface Microstructure

The microstructures of the samples were investigated by field emission scanning electron microscopy (FE-SEM) and energy dispersive X-ray spectrometry (EDX) analysis using a commercially available apparatus (JEOL, JSM-6500 F) in vacuum at room temperature.

In a typical SEM an electron gun and multiple condenser lenses produce an electron beam whose rays at various angles are deflected by the first set of electromagnetic scan coils. The second set of scan coils deflects the beam back across the optic axis. All the rays pass through the final aperture of the final lens and strike the specimen at various points at a time. The resultant

signals contain high energy back scattered electrons, low energy secondary and backscattered electrons, X-rays, and luminescent radiation in the UV, visible, and infrared. Scanning electron micrographs and energy dispersive X-ray spectra are obtained by a scanning electron image (SEI) detector, and an EDS detector, respectively. Figure 2.5 shows the schematic illustration of SEM.[4)]

In the case of FE-SEM, a field emission cathode is used in the electron gun as a substitute for a filament. The field emission cathode provides narrower probing beams as well as high electron energy resulting in improved spatial resolution.

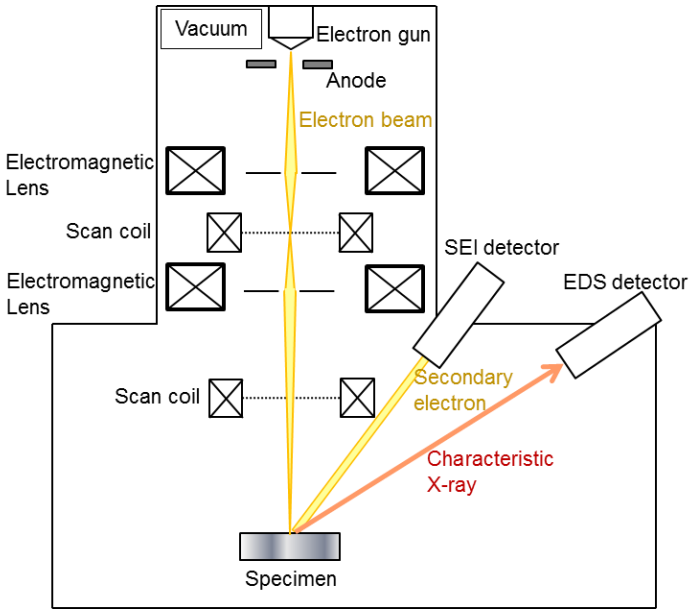

Figure 2.5 Schematic illustration of SEM.[4)]

2.1.5 Electrical Resistivity and Seebeck Coefficient

The high temperature resistivity and thermopower of the samples were measured simultaneously on a Model ZEM-1 electrical resistivity and Seebeck coefficient measuring system (ULVAC-RIKO) under helium atmosphere as shown in Figure 2.6. The electrical resistivity was measured by the standard four probe method. Two thermocouples are attached to the sample to measure the voltage across A and B as ΔV. At the meantime, the temperature is measured between two thermocouples as T_H and T_L. In this way, the measuring temperature T would be

$$T = \frac{(T_H + T_L)}{2} \tag{2.1}$$

The voltage across a reference resistance R_0, which is connected in parallel with the

sample, is measured as V_0. The ΔV is the measured voltage between two thermocouples placed on the sample. The sample resistance (R_{sample}) would be

$$R_{sample} = \frac{\Delta V}{V_0} \times R_0 \tag{2.2}$$

During the measurement, the current applied to the sample is reversed in order to eliminate the influence of the thermopower at the contact point between the probe and the sample. The resistivity can be derived by measuring the resistance value of the sample and taking the dimensions into account as following:

$$\rho = R_{sample} \frac{A}{L} \tag{2.3}$$

where, R_{sample}, A and L are is the sample resistance, cross-sectional area of the sample and L is the distance between the two thermocouples.

The Seebeck coefficients (S) is obtained by the following equation as described in chapter 1.2.1:

$$S = \frac{\Delta V}{\Delta T} \tag{2.4}$$

ΔV is the Seebeck voltage developed between two thermocouples on the sample, across the direction of the temperature gradient. T_H and T_L are the measured absolute temperatures at the two points. The measurement was carried out by applying three temperature gradients of ΔT = 20, 30, and 40 K between two blocks at each temperature T, the average value of three data is used as the experimental value.

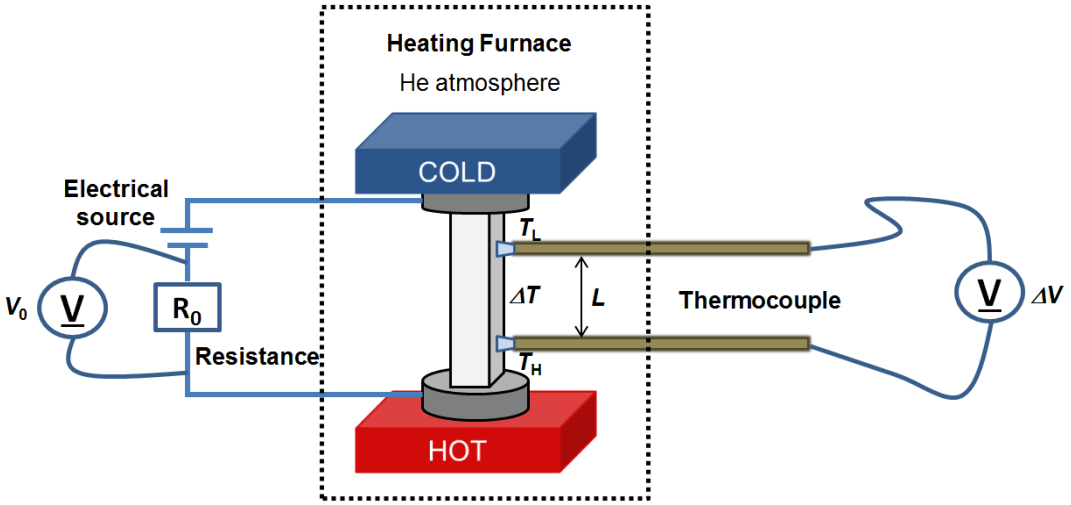

Figure 2.6 Schematic illustrating of the electrical resistivity and the Seebeck coefficient measurement.

2.1.6 Thermal Conductivity

The thermal conductivity of the bulk samples was measured by the laser flash thermal diffusivity (LFTD) method using TC-7000 (ULVAC-RIKO) in vacuum. The LFTD method measures the thermal diffusivity (α) of the sample. The thermal conductivity is determined by

$$\kappa = \alpha D C_P \tag{2.5}$$

where D and C_P are the density of the bulk sample and the heat capacity of the sample, respectively. The heat capacity (C_P) of the sample approaches the classical value $3nR$ at high temperature, i.e. above the Debye temperature, while at low temperature C_P varies according to the T3 law of Debye.[6] In the research, $C_P = 3nR$ is used for estimated the heat capacity of the samples, where n is the number of atoms per formula unit and R is the gas constant.

The thermal diffusivity was measured three times at each temperature and the average value was used as the measurement value. The sketch of the laser flash method is shown in Figure 2.7. Pulse laser causes the temperature change at the back surface of the sample and the temperature change is detected by the infrared sensor. The sample surface was covered with carbon black to prevent the reflection of the pulse laser from the surface. The thermal diffusivity is calculated in the following way.[5]

If the initial temperature distribution within a thermally insulated solid of uniform thickness L is $T(x, 0)$, the temperature distribution at any later time t is given as following, where α is the thermal diffusivity.

$$T(x,t) = \frac{1}{L}\int_0^L T(x,0)dx + \frac{2}{L}\sum_{n=1}^{\infty}\exp\left(\frac{-n^2\pi^2\alpha l}{L^2}\right)\cos\frac{n\pi x}{L}\int_0^L T(x,0)\cos\frac{n\pi x}{L}dx \tag{2.6}$$

If a pulse of radiant energy Q is instantaneously and uniformly absorbed in the small depth g at the front surface $x = 0$ of a thermally insulated solid of uniform thickness L, the

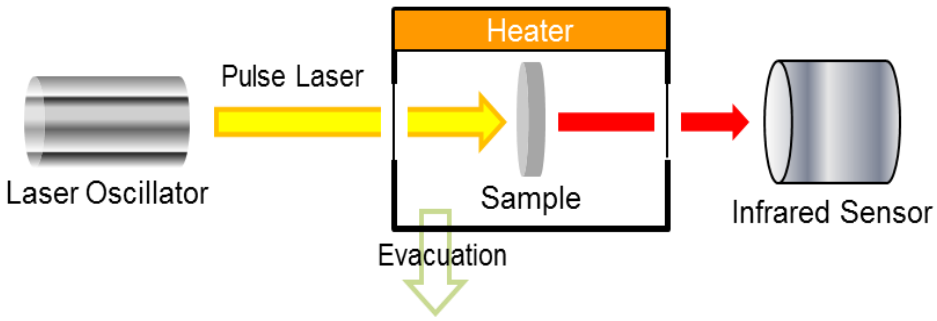

Figure. 2.7 Schematic illustration for the laser flash measurement.

temperature distribution at that instant is given by $T(x, 0) = Q/DC_g$ for $0 < x < g$ and $T(x, 0) = 0$ for $g < x < L$. With this initial condition, equation (2.6) can be written as following.

$$T(x,t) = \frac{Q}{DC_p L}\left[1 + 2\sum_{n=1}^{\infty} \cos\frac{n\pi x}{L} \frac{\sin(n\pi g / L)}{n\pi g / L} \exp\left(\frac{-n^2\pi^2\alpha l}{L^2}\right)\right] \tag{2.7}$$

Since g is a very small number for opaque materials, it follows that $\sin(n\pi g / L) \approx n\pi g / L$. At the rear surface where $x = L$, the temperature history can be expressed by equation (2.8).

$$T(L,t) = \frac{Q}{DC_p L}\left[1 + 2\sum_{n=1}^{\infty} (-1)^n \exp\left(\frac{-n^2\pi^2\alpha l}{L^2}\right)\right] \tag{2.8}$$

Two dimensionless parameters, V and ω can be defined as following relationships, where T_M represents the maximum temperature at the rear surface.

$$V(L,t) = T(L,t) / T_M \tag{2.9}$$

$$\omega = \pi^2 \alpha l / L^2 \tag{2.10}$$

The combination of equations (2.8), (2.9) and (2.10) yields the equation (2.11).

$$V = 1 + 2\sum_{n=1}^{\infty} (-1)^n \exp(-n^2\omega) \tag{2.11}$$

Equation (2.11) is plotted in Figure 2.8. From equation (2.11) and Figure 2.8, thermal diffusivity α is deduced: when V is equal to 0.5, ω is equal to 1.38 and the following relationship is obtained.

$$\alpha = (1.38L^2 / \pi^2 t_{1/2}) \tag{2.12}$$

The parameter $t_{1/2}$ is the time required for the back surface to reach half of the maximum temperature rise.

Without attempting a rigorous analysis, an effective temperature T_e is picked as the time average of the mean of the front and back surface reaches one-half of its maximum value. The dimensionless parameter $V(L,t)$ at the rear surface was given by equation (2.13). The dimensionless parameter $V(0,t)$ at the front surface obtained in a similar manner is given by the following.

$$V(0,t) = 1 + 2\sum_{n=1}^{\infty} \exp(-n^2\omega) \tag{2.13}$$

The mean value of $V(L,t)$ and $V(0,t)$ is

$$\frac{V(0,t)+V(L,t)}{2} = 1 + 2\sum_{n=1}^{\infty} \exp(-4n^2\omega) \tag{2.14}$$

and the effective value of V is expressed as equation (2.15).

$$\begin{aligned} V_{\mathrm{e}} &= 1 + \frac{2}{\omega_{1/2}} \int_0^{\omega_{1/2}} \sum_{n=1}^{\infty} \exp(-4n^2\omega) d\omega \\ &= 1 + \frac{2}{4(1.38)} \left[\sum_{n=1}^{\infty} \frac{1}{n^2} \left(1 - \exp(-4n^2 \times 1.38)\right) \right] \\ &= 1.6 \end{aligned} \tag{2.15}$$

Finally, the effective temperature is given by

$$T_{\mathrm{e}} = V_{\mathrm{e}} T_{\mathrm{M}} = 1.6 T_{\mathrm{M}} \tag{2.16}$$

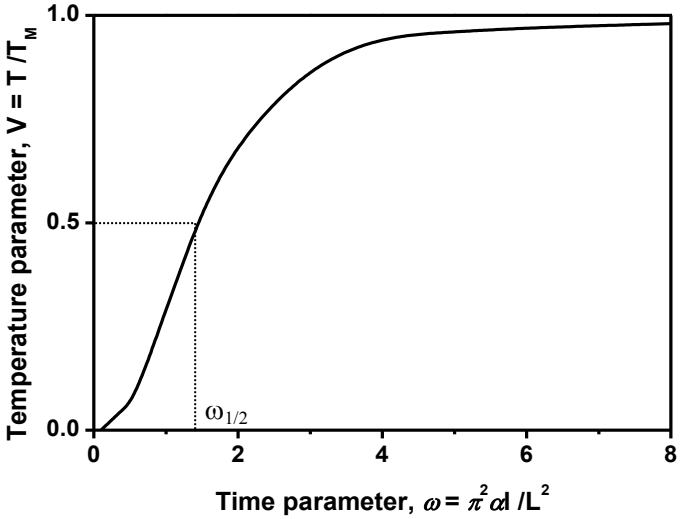

Figure. 2.8 Dimensionless plot of rear surface temperature history

2.1.7 Carrier Concentration and Mobility

The Hall coefficient (R_H) was measured by the Van der Pauw method using Resitest 8300 (Toyo Co. Ltd.) apparatus at room temperature under an applied magnetic field of 0.5 T. The Hall carrier concentration (n_H) and Hall mobility (μ_H) were calculated from the measured R_H assuming a single band model and Hall factor of 1 with following equations;

$$n_{\mathrm{H}} = \frac{\gamma_{\mathrm{H}}}{eR_{\mathrm{H}}} \quad \text{and} \quad \mu_{\mathrm{H}} = \frac{R_{\mathrm{H}}}{\rho} \tag{2.17}$$

where R_H and ρ is the Hall coefficient and the resistivity, respectively, and γ_H is the Hall factor which is given by

$$\gamma_{\mathrm{H}} = \frac{3\sqrt{\pi}}{4} \frac{(2s+3/2)\ !}{[(s+3/2)\ !]^2} \tag{2.18}$$

For acoustic deformation potential scattering where $s = -1/2$, the hall factor becomes γ_H = 1.18, while for ionized impurity scattering where s = 3/2, we find γ_{H} = 1.93. Obviously the order of magnitude of γ_{H} is 1.

The Hall coefficient is given by the following equation using the magnetic field B, Hall voltage V, the current I, and the sample's thickness δ.

$$R_{\mathrm{H}} = \frac{|V_{23}|\delta}{I_{14}B} = \frac{\delta}{B} R_{12,34} \tag{2.19}$$

Here, twice measurements give two resistances:

$$R_{12,34} = \frac{|V_{23}|}{I_{14}} \quad \text{and} \quad R_{23,41} = \frac{|V_{41}|}{I_{23}} \tag{2.20}$$

The numbers indicate proves shown in Figure 2.7. Then, the resistivity is calculated from

$$\rho = \frac{\pi}{\ln 2} \delta \frac{R_{12,34} + R_{23,41}}{2} f \tag{2.21}$$

The factor f depends on the ratio $R_{12,34}/R_{23,41}$ as shown in Figure. 2.9.

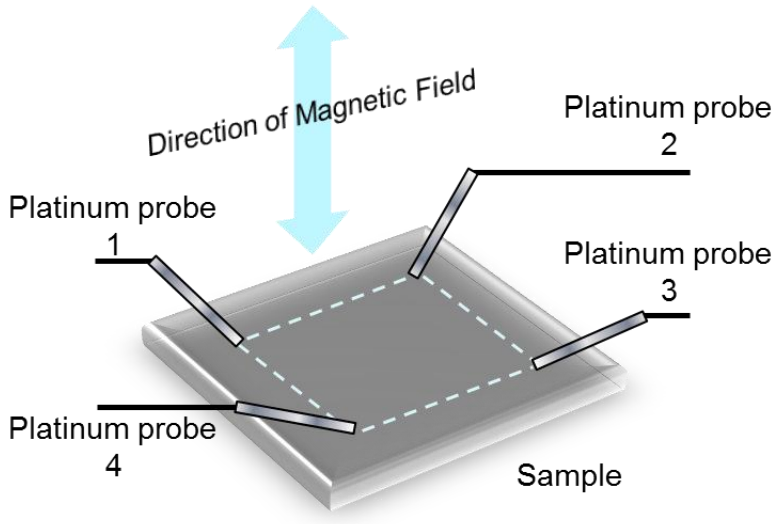

Figure 2.9 Schematic illustration of van der Pauw's method.[7)]

2.1.8 Elastic Moduli and Debye Temperature

The elastic moduli are consisting of the shear modulus (G), Young's modulus (E), Bulk modulus (K), Bulk compressibility (β), and Debye temperature (θ_D). These parameters are evaluated from sound velocities of the samples. The sound velocities, i.e. longitudinal velocity (V_L) and shear velocity (V_S), of the sample were measured by an Ultrasonic pulse echo method (Nihon Matech, Echometer 1062) at room temperature. The schematic view of the apparatus is shown in Figure 2.10.

The sound velocities in the sample can be calculated from the sample length and the time separation between the ultrasonic echoes.[8)] The longitudinal sound velocity and shear sound velocity are described by the following equation:

$$v_L = \frac{2L}{t_2 - t_1} \quad \text{for the longitudinal sound velocity}$$

$$v_S = \left[\left(\frac{t_3 - t_2}{D} \right)^{\frac{1}{2}} + \left(\frac{t_2 - t_1}{2L} \right)^{\frac{1}{2}} \right]^{-\frac{1}{2}} \quad \text{for the shear sound velocity} \tag{2.22}$$

In equation (2.22) t_1 is the reflection time of the longitudinal sound velocity from the bottom face of the sample, t_2 is the reflection time of the longitudinal sound velocity from the top face of the sample, t_3 is the reflection time of the shear sound velocity from the top face of the sample, D is the diameter of the sample and L is the length of the sample. A 5.0 MHz longitudinal wave pulse and shear wave pulse were used for measuring the longitudinal sound velocity and the shear sound velocity, respectively.

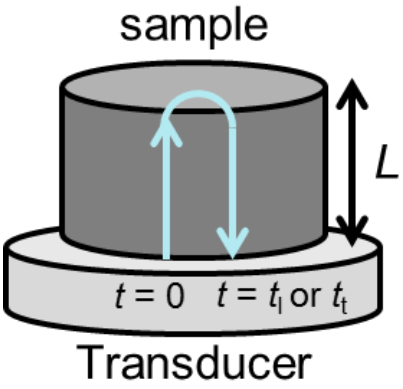

Figure 2.10 Schematic illustration of the sound velocity measurement.

In case of isotropic materials, the Debye temperature (θ_D), Shear modulus (G), Young's modulus (E), and Bulk compressibility (β) can be written in terms of the longitudinal sound velocity (V_L) and the shear sound velocity (V_S) as following equasions:[9, 10,11)]

$$\theta_D = \left(\frac{h}{k_B}\right)\left[\frac{9N}{4\pi V(V_L^{-3} + 2V_S^{-3})}\right]^{\frac{1}{3}} \tag{2.23}$$

$$G = dV_S^2 \tag{2.24}$$

$$E = G\left(\frac{3V_L^2 - 4V_S^2}{V_L^2 - V_S^2}\right) \tag{2.25}$$

$$\beta = \frac{1}{d\left(V_L^2 - \frac{3}{4}V_S^2\right)} \tag{2.26}$$

where h, k_B, N, V and d are the Plank's constant, Boltzmann constant, number of atoms in a unit cell, unit cell volume and total density, respectively.

2.1.9 Thermal Expansion Coefficient

The thermal expansion was measured by a dilatometer method on. The dilatometer is comprised of a cantilevered horizontal tube protruding into a horizontal furnace cavity as described in Figure 2.11. A pushrod is positioned at the center of and parallel to the long axis of the tube. The pushrod is affixed to a high-sensitivity linear displacement transducer. The sample rests on a cradle or holder, which then rests on the bottom inside face of the furnace tube. The sample is positioned against the sealed end of the tube and is held in place by a force maintained on the pushrod from the opposite end. The force applied through the pushrod must be sufficient to maintain complete contact between the stationary tube face, the sample and the pushrod. The temperature rises and expanding sample pushes the pushrod away to the opposite end. Then the displacement sensor perceives a thermal expansion ($\Delta L/L$) as increasing temperature. The average linear thermal expansion coefficient (α_{ave}) is calculated from the obtained $\Delta L/L$ with following equation;

$$\alpha_{ave} = \frac{1}{L_{RT}}\frac{L(T) - L_{RT}}{T - T_{RT}} \tag{2.27}$$

where L_{RT} is the sample length at room temperature.

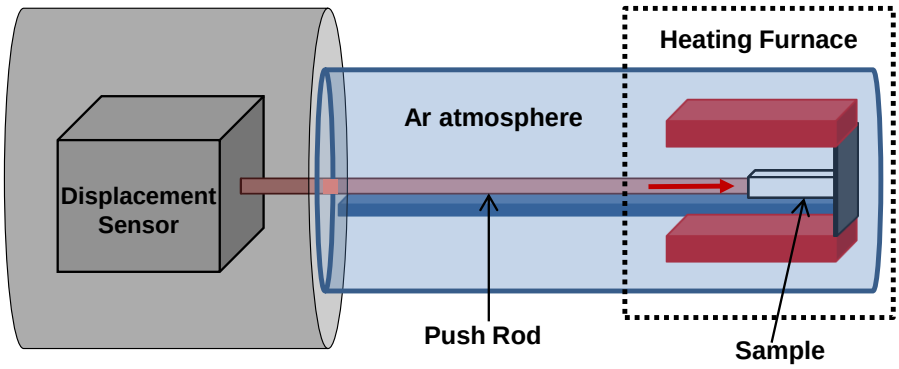

Figure 2.11 Schematic illustration of dilatometer method.

2.2 References

1) V. P. Balema, J. W. Wiench, K. W. Dennis, M. Pruski and V. K. J. Pecharsky, Am. Chem. Soc. **124**, 6244 (2002).

2) V. P. Balem, Material Matters 2, article 2 (2009).

3) D. Kopeliovich, Solid state fabrication of metal matrix composites, www.substech.com.

4) T. G. Rochow and P. A. Tucker: Introduction to Microscopy by Means of Light, Electrons, X Rays, or Acoustics Second Edition (Plenum Press, New York, 1994)

5) W. J. Parker, R. J. Jenkins, C. P. Butler, and G. L. Abbott: J. Appl. Phys. **32**, 1679 (1961).

6) L. J. Pauw, Philips Tech. Rev. **20**, 220 (1958).

7) K. Seeger: Semiconductor Physics - An Introduction, 2nd Corrected and Updated Edition (Springer-Verlag, New York, 1982).

8) S. Yamanaka, A. Kosuga, and K. Kurosaki, J. Alloys Comp. **350**, 288 (2003).

9) H. Inaba and T. Yamamoto, Netsu Sokutei. **10**, 132 (1983).

10) K. Yamada, S. Yamanaka and M. Katsura, Technol. Rep. Osaka Univ. **47**, 181 (1997).

11) M. Fukuhara and I. Yamauchi, J. Mater. Sci. **28**, 4681 (1993).

CHAPTER III

Thermoelectric and Mechanical Properties of Ag_2Te

3.1 Effect of Silver Ion Conduction on Thermoelectric Properties of Ag_2Te

This chapter covers an effect of ion conduction on the phonon transport behavior of TE material. Ag_2Te is well-known as a silver ion conductor. In this compound, a phase transition occurs at around 420 K and silver ions jump to interstitial sites repeatedly at the point of starting the phase transition. I consider that the active movement of silver ions would have influence on the scatterings of both charge carriers and heat carrying phonons in Ag_2Te. In order to evaluate the effect of the silver ion conduction on the thermoelectric properties of Ag_2Te, the Seebeck coefficient, electrical resistivity, thermal conductivity and Hall coefficient of polycrystalline bulk samples of Ag_2Te were examined in the temperature range from room temperature to 650 K.

3.1.1 Introduction

Ag_2Te, AgI and Ag_2Se are well-known as Ag ion conductors. In these compounds, a phase transition occurs at a specific temperature and Ag ions jump to interstitial sites repeatedly at the point of starting the phase transition. I anticipate that the moving Ag ions would influence on the heat carrying phonons transport behavior as described in Figure 3.1. For instance, Ag ions in AgI start to move at around 420 K, resulting that the ionic conductivity increases about 10^4 times.[1] As the result, the κ of AgI shows a rapid decrease at around the phase transition temperature.[2] And in the Ag_8GeTe_6 system, the value of κ_{min} at room temperature showed almost the limited value[3]. T. J Zhu explained that the moving Au atoms in the Ag_8GeTe_6 crystal cell may contribute to the extremly low κ in the Ag_8GeTe_6 system.

Ag_2Te is well-known for not only a high performance of TE material but also an ionic conductor.[4] Ag_2Te exhibits a structural phase transition from a low- to a high-temperature phase

at around 420 K[5] as described in Figure 3.2, which accompanies a dramatic increase in the Ag ionic conductivity from 10^{-3} S/cm to a superionic level of 1 S/cm.[6] The crystalline structure is monoclinic in the low-temperature phase.[7] In the high-temperature phase, it is cubic, and Te anions form a face centered cubic (fcc) sublattice through which Ag cations can move easily, thus giving rise to the superionic conductivity.[6,8] In contrast, the electronic conductivity remains mostly constant at a relatively high value, 10^{2}–10^{3} S/cm, which can be ascribed to a degenerate *n*-type conduction.[9] Accordingly, Ag_2Te could be regarded as a mixed ionic-electronic conductor for the whole temperature range.[10,11] In this chapter, I investigate the effect of silver ion conduction on the phonon transport behavior in Ag_2Te.

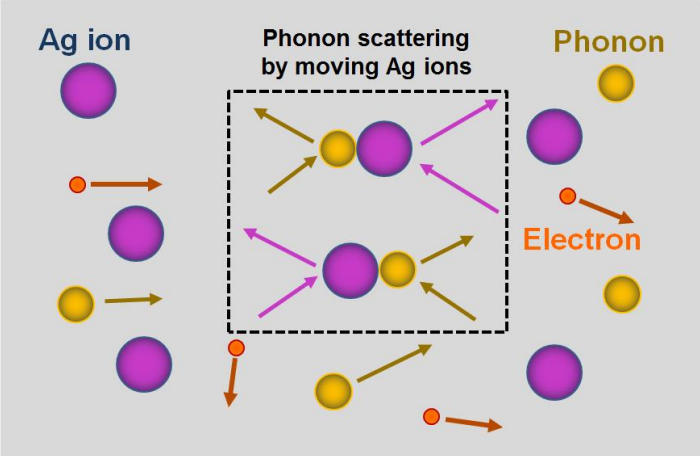

Figure 3.1 Schematic diagram illustrating the phonon scattering by moving Ag ions. The active movement of Ag ions would have an effect on the phonons transport.

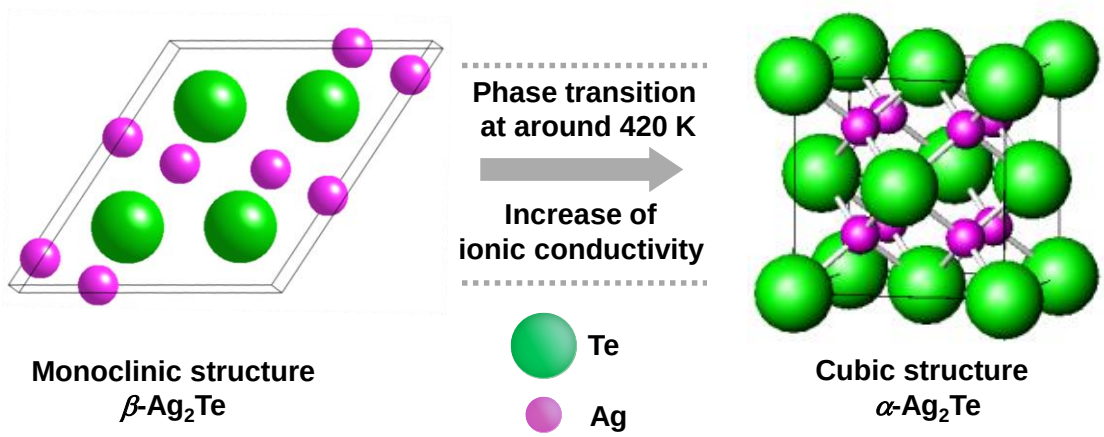

Figure 3.2 Crystal structures of Ag_2Te before and after the phase transition. The α- ↔ β-Ag_2Te phase transition, corresponding to monoclinic to cubic (fcc) transformation, take place at around 420 K.

3.1.2 Experimental Procedures

Ag_2Te and Ag (purity 99.999%) were weighted and put in a silica tube in the ratio of 1:0.25 to produce *n*-type Ag_2Te. The silica tube was sealed in a vacuum and gradually heated up to 1233 K. After keeping the temperature for 24 h, the tube was cooled down slowly to room temperature. The obtained ingots were crushed into fine powders then ball milling for 2 h using a WC pot and balls. The obtained powders were packed into a graphite die and pelletized by hot pressing at a sintering temperature of 923 K under a pressure of 38 MPa in an Ar-flow atmosphere. The density of the polycrystalline samples was calculated from the measured weight and dimensions. The sample was characterized with a powder X-ray diffraction (XRD) method using Cu $K\alpha$ radiation at room temperature. The polished surface of the sample was observed by scanning electron microscope (SEM) and energy dispersive X-ray (EDX) analysis. Differential thermal analysis (DTA) was performed to evaluate the phase transition temperature. The ρ and the S were measured in the temperature range from 323 K to 673 K in a He atmosphere using the commercially available apparatus (ULVAC, ZEM-1). The κ was calculated from the thermal diffusivity (α), heat capacity (C_P), and density (d) based on the relationship of $\kappa = aC_Pd$. The α was measured by the laser flash method using the commercially available apparatus (ULVAC, TC-7000). C_p was estimated from the Dulong-Petit model, that is, $C_p = 3nR$, where n is the number of atoms per formula unit and R is the gas constant. The Hall coefficient (R_H) was measured by the van der Pauw method using the commercially available apparatus (TOYO, Resitest 8300) in a vacuum from 323 K to 523 K under an applied magnetic field of 0.5 T. The Hall carrier concentration (n_H) and Hall mobility (μ_H) were calculated from R_H assuming a single band model and a Hall factor of 1; i.e., $n_H = 1/(eR_H)$ and $\mu_H = R_H/\rho$, where e is the elementary electric charge.

3.1.3 Results and Discussion

The XRD patterns of the sample before and after hot-pressing are shown in Figure 3.3, together with the literature data. It was confirmed that the sample prepared in the present study was a single phase of β-Ag_2Te with the monoclinic *mP12* structure at room temperature[12-14]. There was no change of the phase before and after hot-pressing. The lattice parameters calculated from the XRD patterns are summarized in Table 3.1. The density of the sample was 8.32 g/cm^3, corresponding to 92% of the theoretical density. The SEM and EDX mapping images of the hot-pressed sample are shown in Figure 3.4. The SEM image confirmed that the sample was homogeneous with no remarkable cracks. The EDX analysis revealed that Ag and Te were uniformly distributed on the sample surface. Figure 3.5 shows the DTA curves of the Ag_2Te and AgI samples. It was observed that there existed large endothermic peaks in both the DTA curves. These peaks correspond to the phase transitions with starting Ag ion conduction. From the beginning point of the endothermic peaks, the phase transition temperatures for Ag_2Te and AgI were determined to be 421.3 K and 421.8 K, respectively. These values were in good agreement with the literature data[1,15].

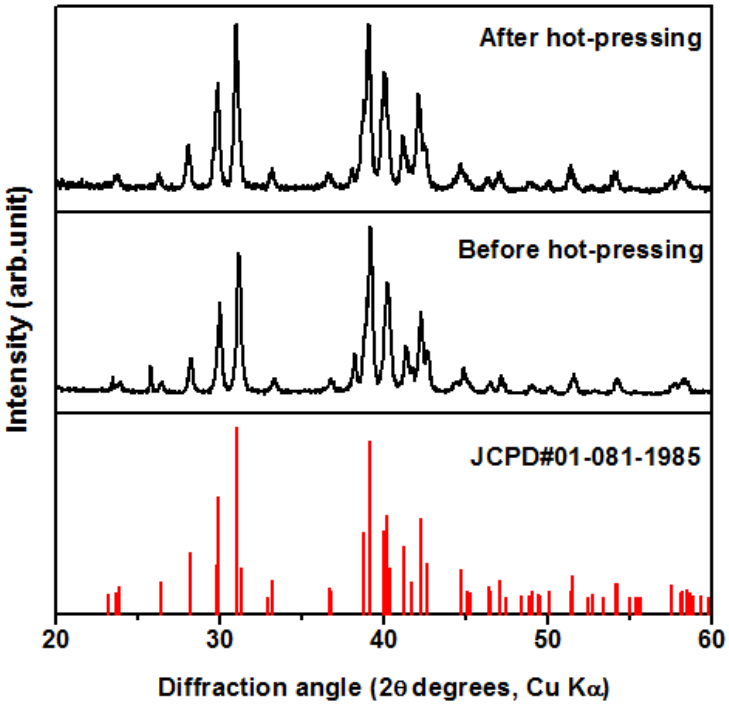

Figure 3.3 Powder XRD patterns of the Ag_2Te sample before and after hot-pressing, together with literature data.

Table 3.1 Lattice parameters and density of the Ag_2Te sample.

Crystal system		Monoclinic (space group *mpl*2)
Lattice parameter	a (nm)	0.817
	b (nm)	0.449
	c (nm)	0.901
	β (degree)	123.9
Theoretical density	d_{th} (gcm^{-3})	9.06
Sample density	d_{exp} (gcm^{-3})	8.32
Relative density	d_{exp}/ d_{th} (%)	92

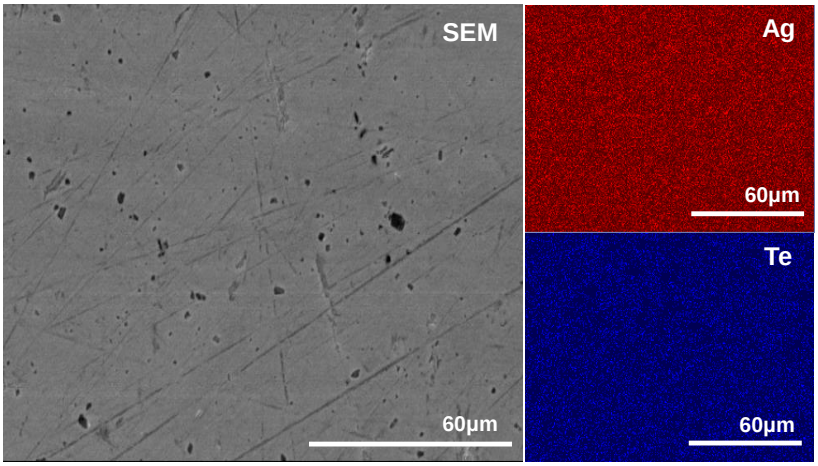

Figure 3.4 SEM and EDX mapping images of the hot-pressed sample of Ag_2Te.

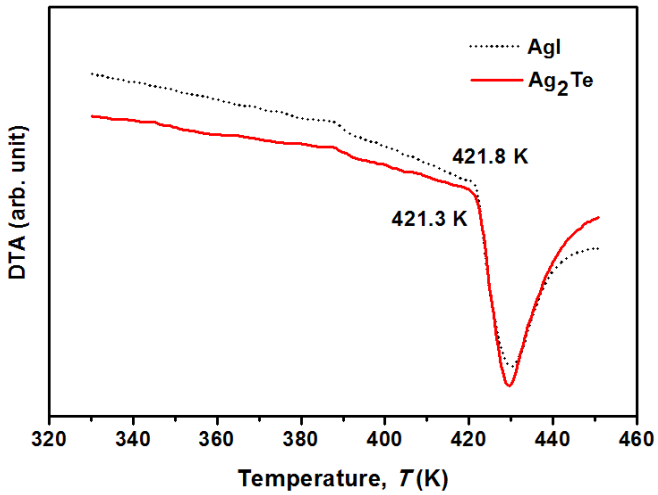

Figure 3.5 DTA curves of Ag_2Te and AgI. The values are corresponding to the phase transition temperature.

The temperature dependences of the ρ of the Ag_2Te sample are shown in Figures 3.6. The ρ of Ag_2Te samples at 335 K is 0.54 mΩcm, whereas the previously reported ρ by Fujikane was 2.75 mΩcm at room temperature. This reduced ρ in our samples might be due to the difference in sample density when compared to the sample in the previous work.[16,17)]

It was confirmed that the ρ of Ag_2Te jumped up at around the phase transition temperature. The ρ value denoted nearly tripling just after the phase transition. The ρ increased with increasing temperature in the whole temperature range. The rate of increase after the phase

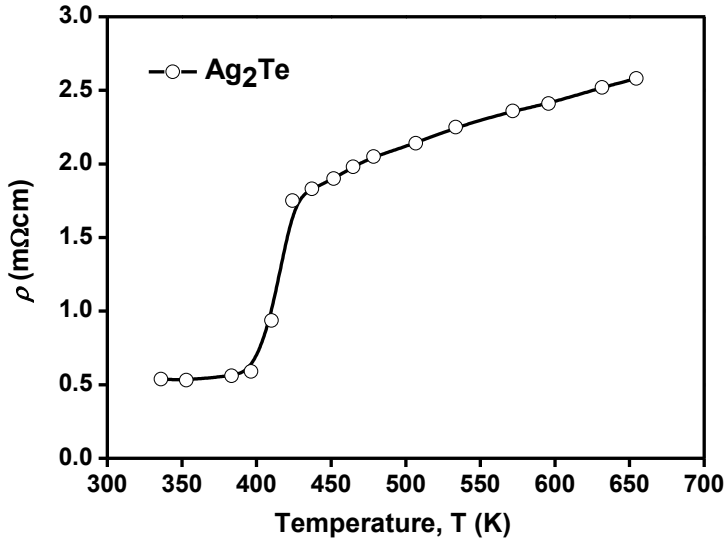

Figure 3.6 Electrical resistivity of Ag_2Te as a function of temperature.

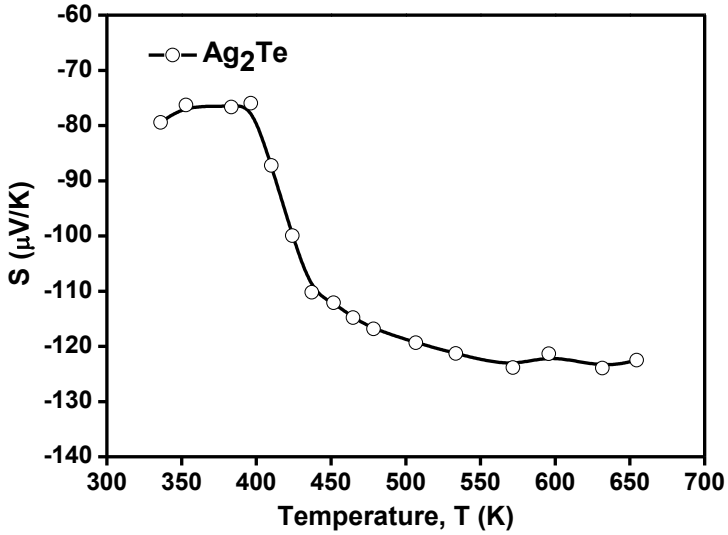

Figure 3.7 Seebeck coefficient of Ag_2Te as a function of temperature.

transition exhibited approximately 4 times larger than that before the phase transition and continues to increase.

The *S* values were negative in the whole temperature range, indicating that the majority of charge carriers were electrons as shown in Figure 3.7. The absolute *S* showed nearly temperature-independent behavior before the phase transition. However, it increased rapidly at around the phase transition temperature, likely due to the decrease of carriers by the phase transition.

To verify the effect of the silver ion conduction on the electrical properties of Ag_2Te, the n_H and the μ_H data were collected in the temperature range from 323 K to 523 K. The results are shown in Figure 3.8. With increasing temperature, the n_H increased until around 420 K, then rapidly decreased followed by slightly increased again. The rapid decrease of the n_H at around the

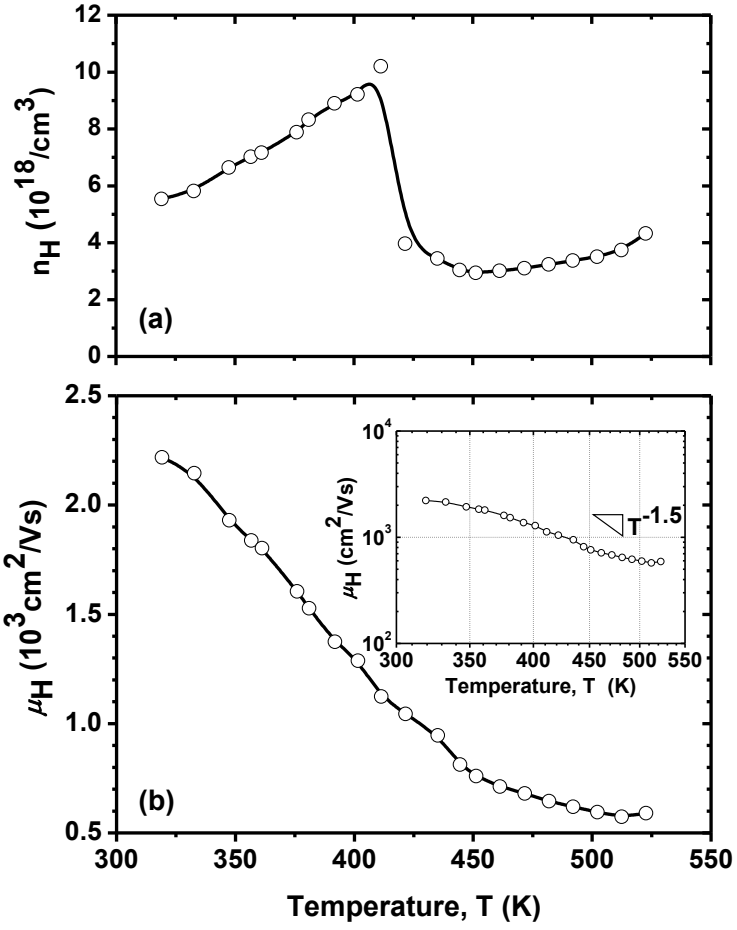

Figure 3.8 Temperature dependence of (a) the Hall carrier concentration n_H, and (b) carrier mobility μ_H. The inset illustrates the μ_H vs. *T* double logarithmic plot.

phase transition temperature corresponded to the increase of both the ρ and the absolute S as shown in Figures 3.8(a) and (b), respectively. While the n_H rapidly decreased after the phase transition, no such drastic changing occurred in the μ_H. The μ_H gradually decreased with increasing temperature roughly according to a $T^{-1.5}$ relation especially at high-temperatures, meaning that the charge carriers were scattered by acoustic phonons predominantly. This result indicates that the silver ion conduction has little influence on the scattering of charge carriers in the case of Ag_2Te.

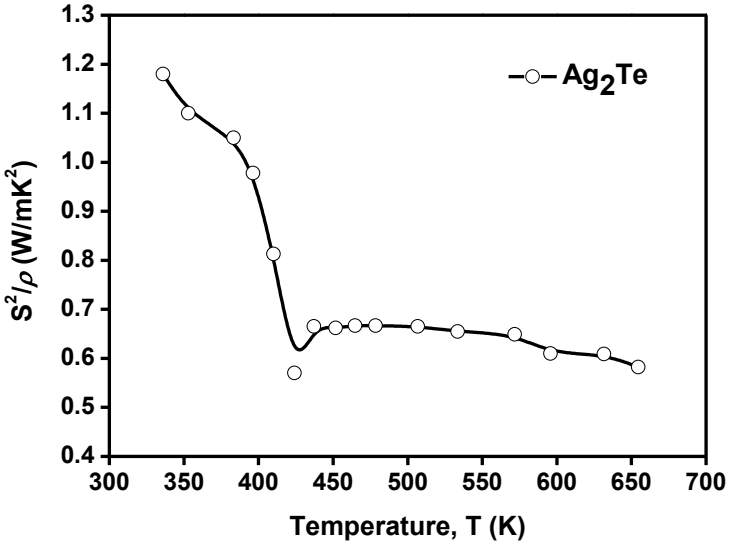

Figure 3.9 Power factor of Ag_2Te as a function of temperature.

The temperature dependence of the S^2/ρ of the Ag_2Te sample is shown in Figure 3.9. As seen in Figure, the S^2/ρ was significantly decreased after the phase transition mostly due to the change of carrier concentration.

The temperature dependence of the κ of the Ag_2Te sample is shown in Figure 3.10. The κ was very sensitive to the phase transition like the ρ and the S. The κ exhibited a maximum to be 1.8 $Wm^{-1}K^{-1}$ before the phase transition and rapidly decreased to 0.9 $Wm^{-1}K^{-1}$ after the phase transition. These values obtained in the present study were slightly higher than the previously reported values,[4,16)] which would be caused by the differences of the sample density and the Ag-doping content between the present and the previous samples. It has been expected that the Ag ion conduction will scatter heat carrying phonons leading to the reduction of the κ_{lat}. Thus, the κ_{lat} was roughly evaluated by subtracting the electronic contribution ($\kappa_{el} = LT\rho^{-1}$, where L is the Lorentz number = 2.45×10^{-8} $W\Omega K^{-2}$) from the measured κ, i.e. $\kappa_{lat} = \kappa - LT\rho^{-1}$. The temperature

dependences of the κ_{ele} and the κ_{lat} are shown in Figure 3.10. I expected that the κ_{lat} might show rapid decrease at around the phase transition temperature due to the phonon scattering by the silver ion conduction. However, the κ_{lat} indicated rather flat temperature dependence. The contributions of electronic conductivity and ionic conductivity to the measured electrical conductivity of Ag_2Te are shown in Table3.2. The electronic contribution is significantly large compared to the ionic contribution. Even though when the ionic conductivity is increased after the phase transition, the contribution occupies only 0.2 % of electrical conductivity. It is known that in the case of AgI in which most electrical conductivity is contributed by ionic conductivity, Ag ion disorder results in the Frenkel defects: the movement of Ag ions into normally vacant interstitial site or increasing anharmonicity of lattice vibration.[1,18] However, in the case of Ag_2Te, the contribution of ionic conductivity is relative low that the Ag ion conduction would have not influenced on the scattering of heat carrying phonons in the case of Ag_2Te.

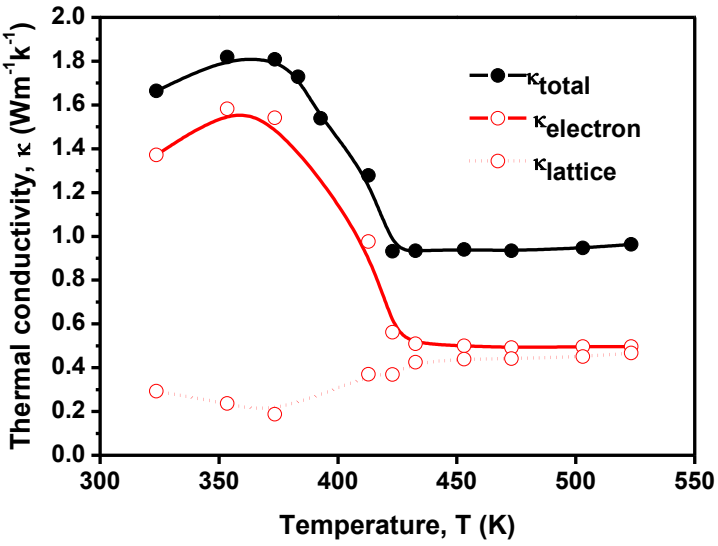

Figure 3.10 Thermal conductivity κ_{total}, electron thermal conductivity $\kappa_{electron}$ and lattice thermal conductivity $\kappa_{lattice}$ of Ag_2Te as a function of Temperature.

Table 3.2 Electronic and ionic conductivity to the overall electrical conductivity of Ag_2Te.

	σ_e [19] (S/cm)	σ_i [6,19] (S/cm)	σ_{exp} (S/cm)	σ_e / σ_{exp} (%)	σ_i / σ_{exp} (%)
Before phase transition	10^3	10^{-2}	1.7×10^3	59	0.58×10^{-3}
After phase transition	2×10^2	1	0.5×10^3	40	0.2

The dimensionless figure of merit of Ag_2Te was calculated from the measured TE properties as shown in Figure 3.11. Although there are low power factor in the α-Ag_2Te range, higher *ZT* value was obtained than those of β-Ag_2Te range due to the low κ after the phase transition. The maximum *ZT* value is 0.36 at 530 K in this study.

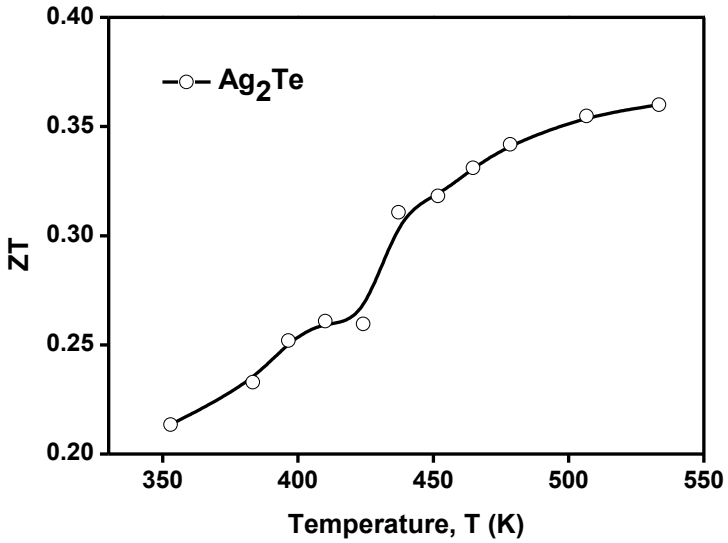

Figure 3.11 Dimensionless of merit of Ag_2Te as a function of temperature.

3.1.4 Conclusion

Dense polycrystalline samples of *n*-type Ag_2Te were synthesized and their TE transport properties were examined. In the DTA curve of the Ag_2Te sample, an endothermic peak was observed at around 420 K, which was due to the phase transition where silver ions moved to start. The ρ and the *S* of the Ag_2Te sample drastically changed at around the phase transition temperature, mainly due to the change of the carrier concentration before and after the phase transition. Both the carrier mobility and the κ_{lat} did not show remarkable changes at around the phase transition temperature; the carrier mobility decreased monotonically with increasing temperature roughly according to a $T^{-1.5}$ relation, and the κ_{lat} showed rather flat temperature dependence. Although we expected that the silver ion conduction should have an impact on the TE transport properties, it has little influences on the scatterings of both charge carriers and heat carrying phonons. In the case of Ag_2Te, the change of the crystal structure, i.e. from monoclinic (β-phase) to cubic (α-phase), led to the change of the carrier concentration, leading to changing the ρ, *S*, and κ_{el}. Consequently, the maximum *ZT* value obtained is 0.36 at 530 K in the α-Ag_2Te.

3.1.5 References

1) P. A. Madden, K. F. O'sullivan and G. Chiarotti: Phys. Rev. B **45**, 10206 (1992).
2) M. C. Goetz and J. A. Cowen: Solid State Communications **41**, 293 (1982).
3) T. J. Zhu, S. N. Zhang, S. H. Yang, and X. B. Zhao, Phys. Status Solidi RRL **4**, 317 (2010).
4) J. Capps, F. Drymiotis, S. Lindsey and T. M. Tritt: Philosophical Magazine Letters **90**, 677 (2010).
5) M. Hansen, Constitution of Binary Alloys ~McGraw-Hill, (New York, 1958).
6) S. Miyatani, J. Phys. Soc. Jpn. **14**, 996 (1959).
7) J. Schneider and H. Schulz, Z. Kristallogr. **203**, 1 (1993).
8) M. Kobayashi, K. Ishikawa, F. Tachibana, and H. Okazaki, Phys. Rev. B **38**, 3050 (1988).
9) S. Miyatani, J. Phys. Soc. Jpn. **13**, 341 (1958).
10) Yu. Ya. Gurevich and A. K. Ivanov-Shits, in Semiconductors and Semimetals, edited by R. K. Willards and A. C. Beer ~Academic, Boston **26**, 338 (1988),
11) S. Miyatani, J. Phys. Soc. Jpn. **14**, 996 (1959).
12) A. V. D. Lee and J. L. D. Boer: Acta Cryst. C **49**, 1444 (1993).
13) T. Sakuma and S. Saitoh, J. Phys. Soc. Jpn. **54**, 3647 (1985).
14) I. Karakaya and W. T. Thompson: Binary Alloy Phase Diagrams, 2nd ed. T. B. Massalski, H. Okamoto, P. R. Subramanian and L. Kacprzak, (ASM International, Materials Park, Ohio, 1990).
15) M. Ohto and K. Tanaka: J. Vac. Sci. Technol. B **14** (1996) 3452-3454
16) M. Fujikane, K. Kurosaki, H. Muta and S. Yamanaka, J. Alloys Compd. **393**, 299 (2005).
17) M. Fujikane, K. Kurosaki, H. Muta and S. Yamanaka, J. Alloys Compd. **387**, 297 (2005).
18) W. Buhrer, R. M. Nicklow and P. Bruesch, Phys. Rev. B **17**, 3362 (1978).
19) IIT JEE Study Material - Solid State; Structure of Ionic compounds

3.2 Thermomechanical Properties of Ag_2Te

When utilizing the TE materials in TE devices, the TE properties as well as thermomechanical properties are quite important at the point of machining reliability. However, since most of researches are focused on an enhancement of TE performance, the thermomechanical properties such as the thermal expansion, melting temperature, hardness and Young's modulus of TE materials have not been researched actively. In this chapter, thermal expansion, indentation hardness of Ag_2Te and AgI were examined. Especially, the dilatometric measurements on solid solution in the Ag_2Te-AgI system were focused in order to look for a zero thermal expansion conditions.

3.2.1 Introduction

Since the enhancement of TE performance by nanostructuring, the interest on the application of TE materials significantly increased. For the application, TE figure of merit (*ZT*) is assuredly the most important characteristic of TE materials. However mechanical properties and thermal expansion are equally important parameters affecting the applicability in TE devices. To warrant a reliability of TE device in the application, the thermal expansion of *n*- and *p*-legs should be considered, otherwise the *n*- and *p*-legs would undergo a mismatch of thermal expansion within the TE device that could cause a crack and consequently degradation of TE performance as shown in Figure 3.12.

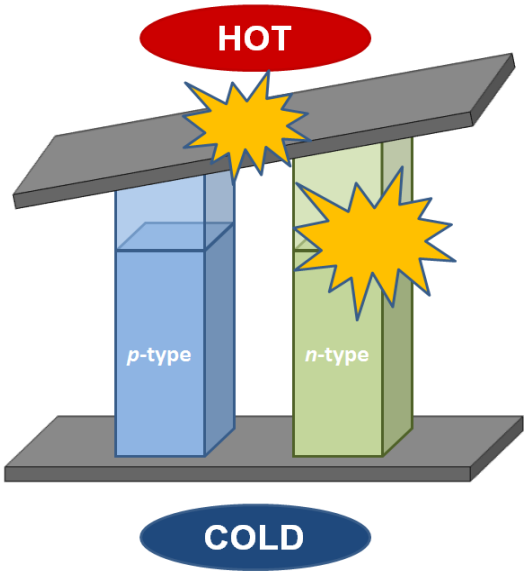

Figure 3.12 Schematic diagram of TE device. TE devices is composed of *n*- and *p*- type TE materials and usually operated under temperature gradation.

For the prevention of this problem, firstly, similar values of the thermal expansion coefficient are required for *n*- and *p*-type TE materials in fabricating a TE generator in order to reduce the mismatch between two materials arising across the temperature gradient. For example, *M*NiSn and *M*CoSb type half-Heusler compounds (*M* = Ti, Zr, Hf) are one of the candidates for non-toxic and high performance of TE materials.[1–7] The *ZT* values and thermal expansion coefficients of representative *n*- and *p*-type half-Heusler compounds are summarized in Table 3.3. As seen in Table 3.3, when utilizing such half-Heusler compounds in the TE generator devices, *n*-type *M*NiSn are suitable for *p*-type ZrCoSb in terms of their *ZT* values. However, the thermal expansion coefficients of *n*-type *M*NiSn are similar to those of ErPbSb and ErPdBi. Therefore, it can be said that from the viewpoint of the stability of TE device, *n*-type *M*NiSn have better compatibility with ErPdSb and ErPdBi than ZrCoSb.

Secondly, thermal expansion of TE material needs to be reduced. The thermal expansion of materials, which is the change of volume with the temperature fluctuation, is a pronounced disadvantage for applications. A large number of piezoelectric ceramics are nowadays present in industrial applications such as sensors, actuators, transducers and some other devices, but many of them might lead to mechanical degradation and structural instability because of the fragility of ceramics towards large volumetric changes with increasing temperature.[18–12] In generally, most natural materials expand with increasing temperature, and this positive correlation between the materials' volume and the temperature is defined as positive thermal expansion (PTE). In contrast, some instances of negative thermal expansion (NTE), in which materials contract with increasing temperature, have been discovered in the last decade.[13–22] Here, I introduce zero thermal expansion (ZTE) materials which neither expand nor contract as the temperature changes. These materials are highly desirable, because they are free from thermal shock on rapid heating or cooling, and can prevent the structural instability and mechanical degradation of materials resulting from sizeable volumetric changes on variation of the temperature.[27,28] As I have already

Table 3.3 *ZT* and thermal expansion coefficients of half - Heusler compounds

	n - type			*p* - type		
	ZrNiSn[23,26]	HfNiSn[26]	TiNiSn[23,26]	ZrCoSb[24]	ErPdSb[25]	ErPdBi[25]
ZT	0.72	-	0.6	0.45	0.16	0.075
α_{ave}($\times 10^{-6}$ K^{-1})	12.1	10.2	11.3	8.9	10.4	10.6

mentioned above, since the TE materials are usually operated under temperature change, a high thermal expansion occur at high temperature and adversely effect on TE device due to their large deformation. Therefore, the TE materials are also desired to have a low thermal conductivity. Nevertheless, the effort to find the conditions for near ZTE coefficients of TE materials has not been actively studied in TE field.

With this background, I focused on the investigation of finding ZTE conditions of Ag_2Te by alloying with AgI which is a negative thermal expansion material as well as an ionic conductor. I will mainly discuss the results about the change of thermal expansion of Ag_2Te-AgI compound and also evaluate the micro indentation hardness.

3.2.2 Experimental Procedures

Polycrystalline samples of $Ag_2Te_{1-x}I_x$ (x = 0, 0.1, 0.2) were prepared from stoichiometric ratios of Ag and Te chunks and AgI powder by direct reaction in a sealed silica tube. All samples were crushed to powders by ball-milling, followed hot-pressing with same condition as described in chapter 3.1.2. All the samples were characterized with a powder X-ray diffraction (XRD) method using Cu $K\alpha$ radiation at room temperature.

The thermal expansion was measured by a dilatometer for rectangular-shaped samples cut from the sintered pellets in the temperature range between room temperature and 573K in an argon atmosphere, with the heating rate 5 K/min. From the obtained thermal expansion curves, the average linear thermal expansion coefficient, α_{ave}, between room temperature T_{RT} and temperature T, was calculated from the equation 2.27.

Hardness (H) were determined by indentation tests using a dynamic ultra - micro tester (DUH-211S, Shimadzu) at room temperature. The maximum load was chosen to be 10, 30, 50, 100, 200, 500, 1000 mN under a loading and unloading times of 15 s.

3.2.3 Results and Discussion

Figure 3.13 shows the thermal expansion of Ag_2Te and AgI obtained by dilatometer measurements in the temperature range from room temperature to 573 K. As shown in Figure 3.13(a), the thermal expansion of Ag_2Te increases linearly in the β–phase range (~420 K), corresponding to expansion of monoclinic phase. And then, the thermal expansion shows rapid increases in the β– and α–phase transition. After the phase transition, the region over 450 K corresponds to the linear expansion of the α–phase (fcc).

The thermal expansion of AgI shows in Figure 3.13(b). Apparently unusual and primarily negative thermal expansion in the measured temperature range is represented for AgI. The thermal expansion is fairly constant or slightly below zero in the β– and α–phase range. However, the thermal expansion shows a sharp negative anomaly at the phase transition temperature. The linear thermal expansion coefficients of Ag_2Te and AgI calculated from the equation 2.27 are listed in Table 3.4.

As temperature is increased, some increase in bond lengths is generally normal behavior. The actual amount of expansion has relevance to the strength of the bond.[29,30] Thus, very strong bonds, such as those between oxygen and high - valent cations, typically show no detectable change in bond length over a temperature range as large as 1237 K.[31] On the basis of these considerations, very low thermal expansion might be expected for some materials, but negative thermal expansion cannot be anticipated based on the thermal expansion behavior of bonds.[32]

A negative thermal expansion coefficient in AgI is thermodynamically in keeping with its other uniquely anomalous properties. This is considered to be caused by uniquely anomalous properties of AgI which has a large number of defects such as Frenkel defects (vacancies and interstitials) and low activation energy for silver ion jump. Lawn explained this phenomenon that the radius of the interstitial void which may snugly accommodate is larger than that of Ag ion. The displacement of nearest neighbours toward the oppositely charged interstitial may prove sufficient to outweight the outward relaxation about the vacated lattice site, thereby producing an overall contraction in one unit cell volume.[33] However, the exact origin of this phenomenon is still an open question.[34]

From this characteristic of Ag_2Te and AgI, the thermal expansion of a solid solution of Ag_2Te with AgI is expected to be weak compared to Ag_2Te especially in the range of the phase transition temperature through a cancellation effect by different thermal expansion between Ag_2Te and AgI.

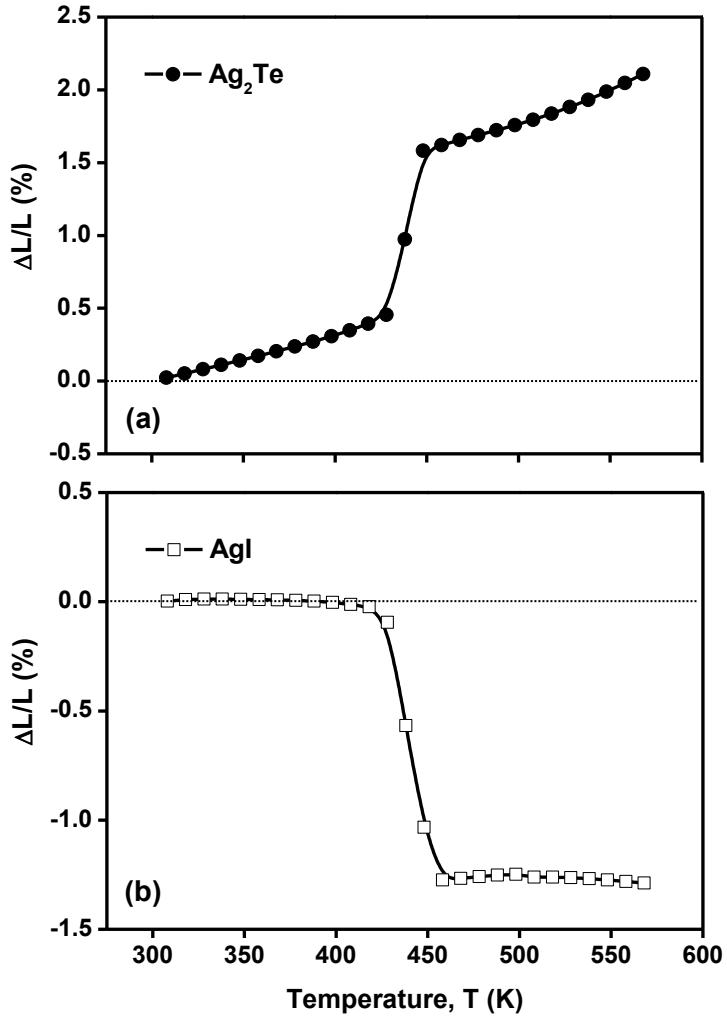

Figure 3.13 Thermal expansion of polycrystalline samples of (a) Ag_2Te and (b) AgI obtained from dilatometer measurements.

Table 3.4 Average linear thermal expansion of Ag_2Te and AgI

	Linear thermal expansion coefficient, α_{ave} ($\times 10^{-5} K^{-1}$)	
Temperature range	Ag_2Te	AgI
308 ~ 428 K	3.36	-2.37
448 ~ 568 K	4.31	-1.34
308 ~ 568 K	8.01	-4.96

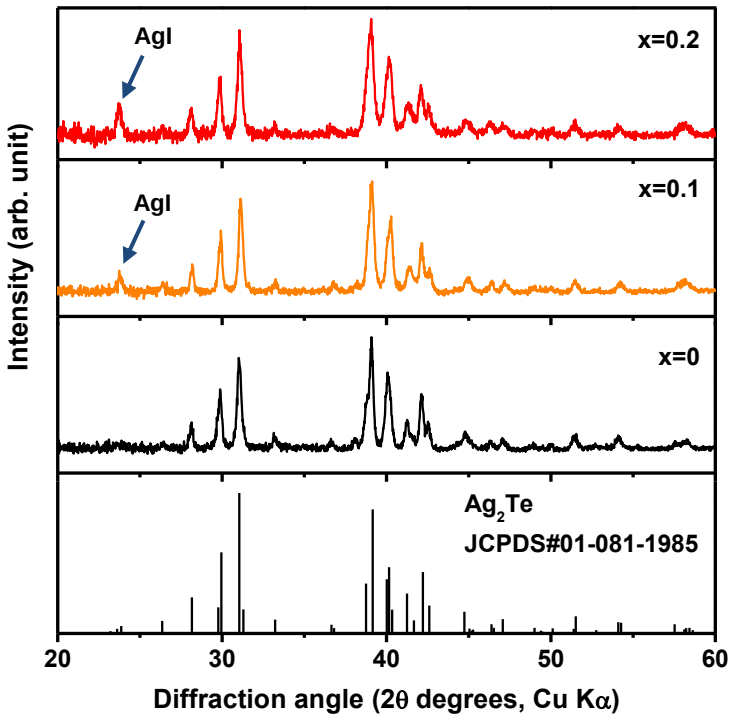

Figure 3.14 Power XRD patterns of polycrystalline samples of *n*-type $Ag_2Te_{1-x}I_x$ (x = 0, 0.1, 0.2), after hot-pressing together with the peak position of Ag_2Te.

Table 3.5 Lattice parameter and sample bulk density of *n*-type $Ag_2Te_{1-x}I_x$

		$Ag_2Te_{1-x}I_x$		
		x = 0	x = 0.1	x = 0.2
Lattice parameter	a (nm)	0.8178	0.8158	0.8171
	b (nm)	0.4476	0.4465	0.4472
	c (nm)	0.8993	0.8971	0.8985
Theoretical density	d_{th} (gcm^{-3})	9.03	9.09	9.05
Measured density	d_{exp} (gcm^{-3})	8.01	7.81	7.77
Relative density	$d_{exp}/ d_{th} \times 100$ (%)	88.6	86.3	85.9

Figure 3.14 shows powder XRD patterns of polycrystalline samples of *n*-type $Ag_2Te_{1-x}I_x$ (x = 0, 0.1, 0.2), together with the peak position of Ag_2Te. Small impurity peaks of AgI were detected in the x = 0.1, 0.2 samples as indicated arrows. The lattice parameters of $Ag_2Te_{1-x}I_x$ (x = 0, 0.1, 0.2) samples were calculated from the XRD patterns, and the results are summarized in Table 3.5. It was confirmed that the lattice parameters of x = 0.1 sample decreased and then for the x = 0.2 sample, lattice parameter slightly increased. Therefore, the solubility limit of I in

Ag_2Te could be concluded to under 10 at % from the results of the formation of second phase (AgI) and the non-linear change of lattice parameters for the x = 0.1, 0.2 samples.

Figure 3.15 represents the results of dilatometer measurement of polycrystalline samples of *n*-type $Ag_2Te_{1-x}I_x$ (x = 0.1, 0.2), together with Ag_2Te. As shown in Figure 3.15, the trend of dilatometric curves of both $Ag_2Te_{0.9}I_{0.1}$ and $Ag_2Te_{0.8}I_{0.2}$ agreed well with the result of Ag_2Te which is lineally increased from room temperature to 413 K and after the phase transition, lineally increased to 573 K. Above all things, it is important to note that the thermal expansion is increased slowly in the temperature range of phase transition. This might be due to the shrinkage of Ag-I bonding in the $Ag_2Te_{1-x}I_x$ structure, especially during the occurrence of phase transition as shown in Figure 3.13(b). The linear average thermal expansion coefficient of the samples was calculated from the equation 2.27 and the average volume thermal expansion coefficient also was

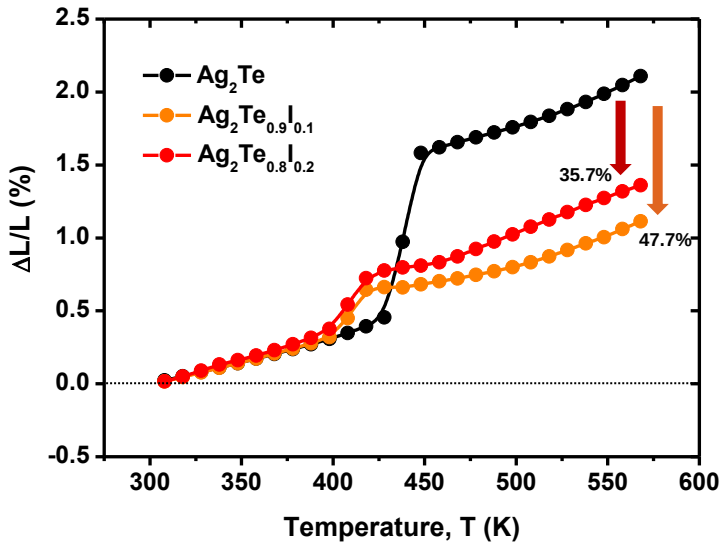

Figure 3.15 Thermal expansion of polycrystalline samples of *n*-type $Ag_2Te_{1-x}I_x$ (x = 0, 0.1, 0.2) obtained from dilatometer measurements.

Table 3.6 Average linear thermal expansion coefficient of $Ag_2Te_{1-x}I_x$

		$Ag_2Te_{1-x}I_x$		
	temperature range	x = 0	x = 0.1	x = 0.2
α_{lave} ($\times 10^{-5}$ K^{-1})	308 ~ 398 K	3.15	3.39	3.99
	448 ~ 568 K	4.31	3.58	4.55
	308 ~ 568 K	8.02	4.22	5.16
α_{Vave}($\times 10^{-5}$ K^{-1})	308 ~ 568 K	24.06	12.66	15.48

α_{lave}, average linear thermal expansion coefficient; α_{Vave}, average volume thermal expansion coefficient.

roughly calculated with the relationship; $\alpha_V \approx 3\alpha_l$.[35] The results are listed in Table 3.6. No remarkable change showed in the linear α_{lave} of x = 0.1 and 0.2 samples before and after the phase transition. However, the linear α_{lave} of x = 0.1 and 0.2 samples represent 4.22×10^{-5} K^{-1} and 5.16×10^{-5} K^{-1} in the whole measured temperature range which are about 47.7 % and 35.7 % increased values, respectively, compared to Ag_2Te. Furthermore, the α_{Vave} also significantly decreased, meaning that when utilizing Ag_2Te in the TE generator device, the $Ag_2Te_{1-x}I_x$ (x = 0.1, 0.2) are more suitable than the Ag_2Te in the terms of stability.

Figure 3.16 shows the indentation hardness of $Ag_2Te_{1-x}I_x$ (x = 0, 0.1, 0.2) together with AgI. As seen in Figure 3.16, the hardness slightly decreases with increasing I content because AgI shown relatively weak hardness have a minor effect on the hardness of $Ag_2Te_{0.9}I_{0.1}$ and $Ag_2Te_{0.8}I_{0.2}$. Above 200 mN of load, both $Ag_2Te_{0.9}I_{0.1}$ and $Ag_2Te_{0.8}I_{0.2}$ shows almost same values of hardness, corresponding ~19 % lower than that of Ag_2Te.

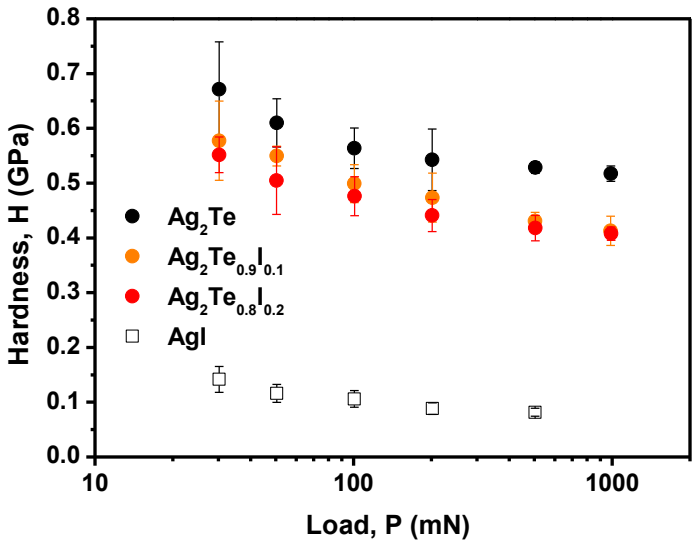

Figure 3.16 Hardness of polycrystalline samples of *n*-type $Ag_2Te_{1-x}I_x$ (x = 0, 0.1, 0.2) together with AgI obtained from dilatometer measurements.

3.2.4 Conclusion

ZTE would be an important requirement in TE devices which operate at higher than ambient temperature. An attempt to look for near ZTE of Ag_2Te was carried out mainly with AgI in this chapter. Consequently, while the hardness of Ag_2Te decreased about 19 % by alloying with AgI which have anomaly a negative thermal expansion, the linear thermal expansion coefficient of Ag_2Te significantly is reduced. Average linear thermal expansion coefficients of $Ag_2Te_{0.9}I_{0.1}$ and $Ag_2Te_{0.8}I_{0.2}$ were reduced about 47.7 % and 35.7 %, respectively. This achievement is expected to play an important role in practical use of Ag_2Te in TE device in terms of stability and open a new possibility that the thermal expansion of TE materials can control.

3.2.5 References

1) C. Uher, J. Yang, S. Hu, D.T. Morelli, G.P. Meisner, Phys. Rev. B **59**, 8615 (1999).
2) Q. Shen, L. Chen, T. Goto, T. Hirai, J. Yang, G.P. Meisner, C. Uher, Appl. Phys. Lett. **79**, 4165 (2001).
3) S. Bhattacharya, A. L. Pope, R.T. Littleton, T. M. Tritt, V. Ponnambalam, Y. Xia, and S. J. Poon, Appl. Phys. Lett. **77**, 2476 (2000).
4) Y. Xia, S. Bhattacharya, V. Ponnambalam, A. L. Pope, S. J. Poon and T. M. Tritt, J. Appl. Phys. **88**, 1952 (2000).
5) Y. Xia, V. Ponnambalam, S. Bhattacharya, A. L. Pope, S. J. Poon and T. M. Tritt, J. Phys.: Condens. Matter **13**, 77 (2001).
6) T. Wu,W. Jiang, X. Li, Y. Zhou and L. Chen, J. Appl. Phys. **102**, 103705 (2007).
7) H. Muta, T. Kanemitsu, K. Kurosaki, S. Yamanaka, J. Alloys Compd. **469**, 50 (2009).
8) G. H. Haertling, J. Am. Ceram. Soc. **82**, 797 (1999).
9) P. Janker, M. Christmann, F. Hermle, T. Lorkowski and S. Storm, J. Eur. Ceram. Soc. **19**, 1127 (1999).
10) B. W. Chua, L. Lu, M. O. Lai and G. H. L. Wong, J. Alloys Com. **381**, 272 (2004).
11) S. Jiansirisomboon, K. Songsiri, A. Watcharapasorn and T. Tunkasiri, Cur. Appl. Phys. **6**, 299 (2006).
12) 14 R. Tickoo, R. P. Tandon, K. K. Bamzai and P. N. Kotru, Mater. Sci. Eng. B **110**, 177 (2004).
13) C. N. Chu, N. Saka and N. P. Suh, Mater. Sci. Eng. **95**, 303 (1987).
14) J. S. O. Evans, T. A. Mary, T. Vogt and A. W. Sleight, Science **272**, 90 (1996).
15) J. S. O. Evans, T. A. Mary and A. W. Sleight, Physica. B **241**, 311 (1998).
16) A. W. Sleight, Nature **425**, 674 (2003).
17) G. Shirane, S. Hoshino and K. Suzuki, Phys. Rev. B **80**, 1105 (1950).
18) G. A. Rossetti, J. P. Cline and A. Navrotsky, J. Mater. Res. **13**, 3197 (1998).
19) X. R. Xing, J. X. Deng, J. Chen and G. R. Liu, Rare Metals. **22**, 294 (2003).
20) A. K. Tyagi, S. N. Achary and M. D. Mathews, J. Alloy Com. **339**, 207 (2002).
21) J. Chen, X. R. Xing, R. B. Yu and G. R. Liu, Appl. Phys. Lett. **87**, 231915 (2005).
22) P. Lommens, C. D. Meyer, E. Bruneel, K. D. Buysser, I. V. Dridssche and S. Hoste, J. Eur. Ceram. Soc. **25**, 3605 (2005).
23) H. Muta, T. Kanemitsu, K. Kurosaki and S. Yamanaka, J. Alloys Compd. **469**, 50 (2009).

24) T. Sekimoto, K. Kurosaki, H. Muta and S. Yamanaka, J. J. Appl. Phys. **46**, L673 (2007)..

25) T. Sekimoto et. al, J. Appl. Phys. **99**, 103701 (2006).

26) D. Jung, K. Kurosaki, C. Kim, H. Muta, and S Yamanaka, J. Alloy and comp. **489**, 328 (2010).

27) A. Jayaraman, E. Bucher, P. D. Dernier and L. D. Longinotti, Phys. Rev. Lett. **31**, 700 (1973).

28) J. Arvanitidis, K. Papagelis, S. Margadonna, K. Prassides, and A. N. Fitch, Nature **599**, 425 (2003)

29) H. D. Z. Megaw, Kristallogr. A **100**, 58 (1938).

30) R. M. Hazen, C. T. Prewitt, Am. Miner. **62**, 309 (1977).

31) I. D Brown and R. D. Shannon, Acta Cryst. **29**, 266 (1973).

32) J. S. O. Evans, T. A. Mary, T. Vogt, M. A. Subramanian, and A. W. Sleight, Chem. Mater. **8**, 2809 (1996).

33) B. R. Lawn, Acta Cryst. **17**, 1341 (1963).

34) D. B. Mohan and C. S. Sunandana, J. Phys. Chem. B **100**, 4569 (2006).

35) Y. S. Touloukian, R. K. Kirby, R. E. Taylor and P. D. Desai, Thermophysical Properties of Matter, Volume **12**, Thermal Expansion, Metallic Elements and Alloys (New York: IFI–Plenum, 1975).

CHAPTER IV

Thermoelectric and Mechanical Properties of Au nanoparticles-supported $Sb_{1.6}Bi_{0.4}Te_3$ Synthesized by a γ-ray irradiation Method

4.1 Thermoelectric Properties of Au nanoparticle-supported $Sb_{1.6}Bi_{0.4}Te_3$ Nanocomposite

In this chapter, a γ-ray irradiation method is introduced as a new method to synthesize a complete nanocomposite composed of Au nanoparticles and TE material $Sb_{1.6}Bi_{0.4}Te_3$. The γ-ray irradiation method has been previously applied in a biomedical field to support Au nanoparticles on iron oxide particles, in where the Au nanoparticles need to become smaller and increase the number on the iron oxide particles. I extended this approach to TE material $Sb_{1.6}Bi_{0.4}Te_3$ and this is the first experimental attempt in the TEs field. The results of γ-ray irradiation on TE material and the effect of Au nanoparticles on TE properties of polycrystalline bulk $Sb_{1.6}Bi_{0.4}Te_3$ will be discussed.

4.1.1 Introduction

Bi_2Te_3–based compounds, for many years, have been some of the most efficient commercial TE materials near room temperature. Commercial alloys of this material which are fabricated by a traditional solid-state reaction method, have been obtained with maximum *ZT* close to 0.8 at around 330 K, corresponding to several % efficiency of heat to energy conversion. However, this efficiency is still relatively low for practical use for widespread commercial applications. A *ZT* of 1 or more, corresponding to a device efficiency of above 10%, needs to be achieved. To achieve high *ZT*, a material with a high power factor and a very low thermal

conductivity is required. The problem is that the transport parameters are interdependent and, often, attempts to maximize one parameter have deleterious effect on the other parameters. There are continuous effort to control each parameters that many studies have shown that it is possible to enhance the thermoelectric performance of materials beyond what is possible in bulk materials by the use of nanostructures, either through the quantum low-dimensional effects on the change of electronic energy states, the selective filtering of low energy electrons across a barrier, or by interfacial scattering of phonons to reduce the thermal conductivity. And several groups have reported enhanced *ZT* by nanostructuring,[1)] such as the development of nanostructured PbTe-based alloys,[2)] nanostructured BiSbTe,[3)] and Bi_2Te_3-based nanocomposites.[4)] These studies achieved to control only κ_{lat} without decreasing of electrical properties mainly due to increased phonon scattering at grain boundaries and interfaces. At the present time a number of research groups are developing nanocomposite materials with a potential for scale-up and practical applications. The overarching goals for designing these nanocomposites materials are to introduce many interfaces that are specially chosen to: 1) reduce the thermal conductivity more than the electrical conductivity conduction by interface scattering,[5-13)] and 2) to increase Seebeck coefficient[14-17)] (for example, by carrier-energy filtering or by quantum confinement) more than decreasing the electrical conductivity, thereby yielding an increase in power factor, with both goals helping to increase *ZT*.

With this background, I focused on nanocomposite TE materials in which nanoparticles are uniformly incorporated into a matrix of bulk TE material. As I already mentioned above, it is considered that such a nanocomposite structure has the potential to scatter phonons effectively at the interfaces between nanoparticles and the matrix phase as described in Figure 4.1, resulting in reduction of κ_{lat} and consequent enhancement of *ZT*.[18)] The TE properties of various nanocomposites, such as Bi_2Te_3/SiC,[19)] $La_{0.9}CoFe_3Sb_{12}/CoSb_3$,[20)] and $Ba_{0.3}Co_4Sb_{12}$/Ag[21)] have been previously reported, wherein enhanced *ZT* was achieved mainly due to significant reduction of κ_{lat}. Furthermore, although rarely observed, the presence of nanoparticles might in principle also lead to an enhancement in the Seebeck coefficient via processes such as carrier energy filtering in a TE nanocomposite structure. The interfaces between nanoparticles and the matrix phase produce potential energy barriers which would scatter low energy electrons less than barrier height, while transmitting high energy electrons. This concept is well-known as energy filtering effects, resulting in enhanced *S* coefficient since the charge is carried by high energy electrons as shown in Figure 4.2.[14,22-24)] These results suggest that nanocomposite TE materials

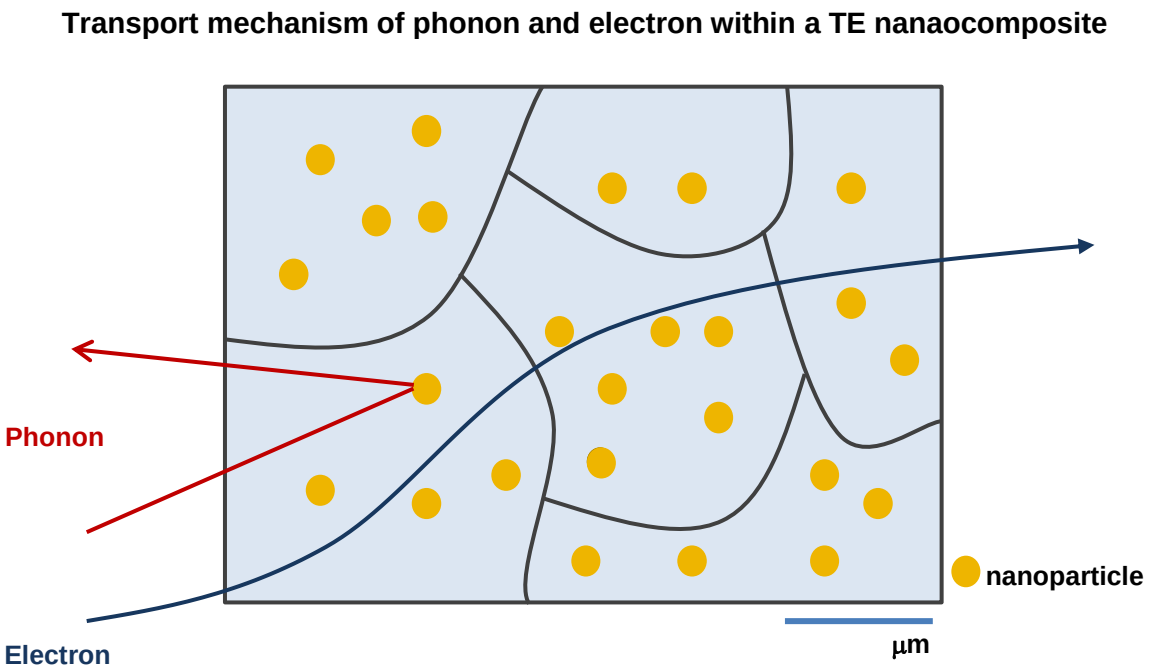

Figure 4.1 Schematic diagram illustrating phonon scattering mechanism within a TE nanocomposite, along with electronic transport of electron. Phonons are scatted by the nanoparticles, whereas electrons are less influenced by the nanoparticles than phonons.

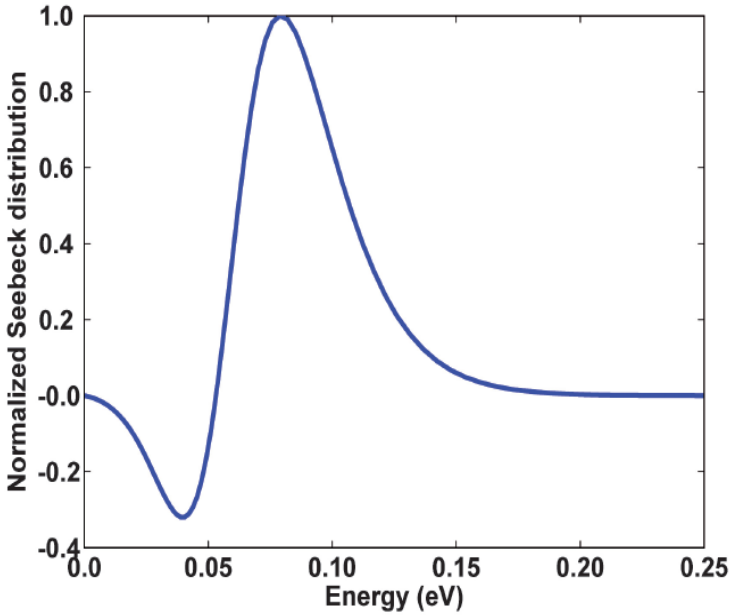

Figure 4.2 Calculated normalized Seebeck distribution versus energy for heavily doped bulk *n*-type $Si_{80}Ge_{20}$. Low energy electrons reduce the total Seebeck coefficient.[24)]

can be effective in enhancement of *ZT*. And the synthesis method of nanocomposite in the present study is the first attempt to embed metallic nanoparticles in the BiSbTe matrix.

Generally, nanocomposite structures have been prepared by ball-milling of nanoparticles as precipitates and microparticles of TE materials as the matrix phase, followed by hot-pressing[3,25,26] or spark plasma sintering.[27,28] However, it is difficult to disperse nanoparticles uniformly into the matrix phase, i.e., the nanoparticles typically tend to clump during ball-milling. Figure 4.3 shows one example of (Zr,Hf)NiSn half-Heusler alloys with nano-ZrO_2.[28,30] As seen in the picture, There are many ZrO_2 nanoinclusions aggregations situated on the grain boundaries, which exerted an important influence on not only the phonon transport but also the electron transport resulted in an increase in electrical resistivity.

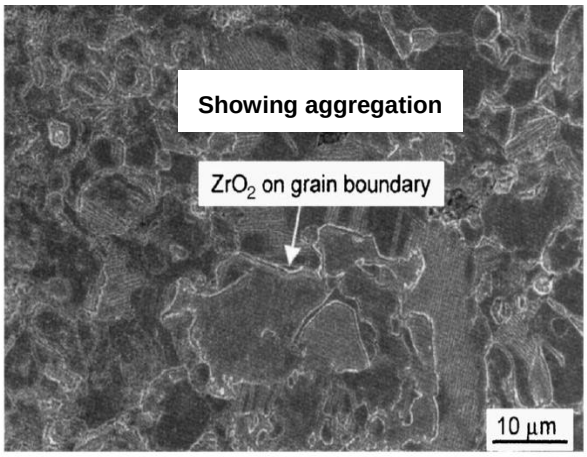

Figure 4.3 SEM micrograph of the(Zr,Hf)NiSn half-Heusler alloys containing 3 vol% ZrO_2 nanoinclusions.[30]

Here, I propose a new method to synthesize a complete nanocomposite using γ-ray irradiation, in which Au nanoparticles are dispersed uniformly without aggregation in the BiSbTe matrix phase. This method has been previously applied in a biomedical field, where Au nanoparticles were supported on iron oxide particles. The iron oxide particles need appropriate surface coating to make them to combine with specific biomolecules and to avoid nonspecific absorption of unwanted species. To enhance the specific adsorption and suppress the nonspecific adsorption, it is necessary to reduce the size and increase the number of Au particle on the iron oxide nanoparticle.[31,32] Figure 4.4 represents TEM images of composite nanoparticles of (a) Au/γ-Fe_2O_3, (b) Au/Fe_3O_4, (c) Pt/γ-Fe_2O_3, and (d) Pd/γ-Fe_2O_3, respectively synthesized by γ-ray

irradiation. Smaller particles with a size of ~10 nm and stronger contrast show noble metal, indicating uniform dispersion on the surface of larger magnetic nanoparticles. I expected that in a nanocomposite composed of nano-sized noble metal and BiSbTe, κ_{lat} could be decreased by phonon scattering at the interfaces between nano-sized Au and BiSbTe, and the *ZT* could be enhanced.

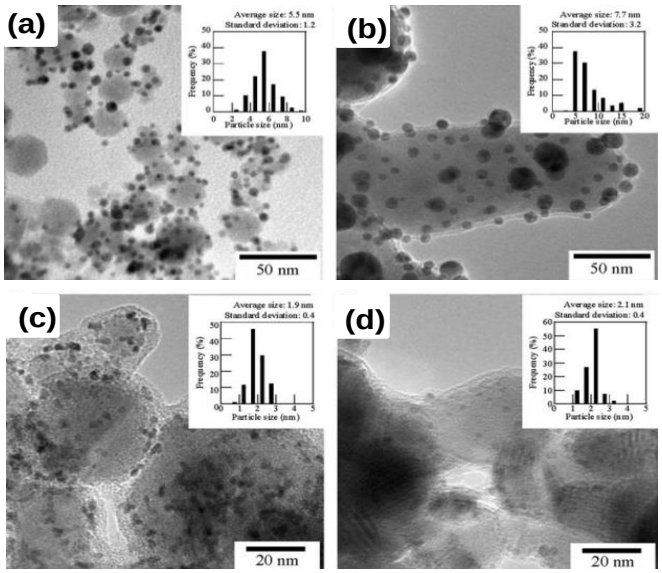

Figure 4.4 TEM micrographs of the composite nanoparticles[31]; (a) Au/γ-Fe_2O_3, (b) Au/Fe_3O_4, (c) Pt/γ-Fe_2O_3, and (d) Pd/γ-Fe_2O_3. The insets indicate the particle size distributions of noble metal nanoparticles immobilized on magnetic iron oxide particles

4.1.2 Experimental Procedures

In the γ-ray irradiation method, microparticles are dispersed in an aqueous solution containing Au ions. γ-ray irradiation into the aqueous solution induces a radiation-chemical reaction, forming metallic Au nanoparticles on the surface of the microparticles. Since this process is carried out in an aqueous solution, the microparticles should be stable in water. Therefore, I estimated a stability of Te, Bi and Sb microparticles in water. Figure 4.5 shows XRD patterns of (a) Te microparticles, (b) Bi microparticles, and (c) Sb microparticles as time passed in water. Te and Bi microparticle are easily oxidized in water in several hours as shown in Figure 4.5(a) and (b), in which TeO_2 and Bi_2O_3 peaks were detected in 1 and 3 hours, respectively, whereas Sb microparticles did not oxidize for over 10 days in water. Thus, Au nanoparticles are first supported on the surface of Sb microparticles by the γ-ray irradiation method, and then they are ball milled together with microparticles of Bi and Te to form BiSbTe alloy containing uniformly dispersed Au nanoparticles.

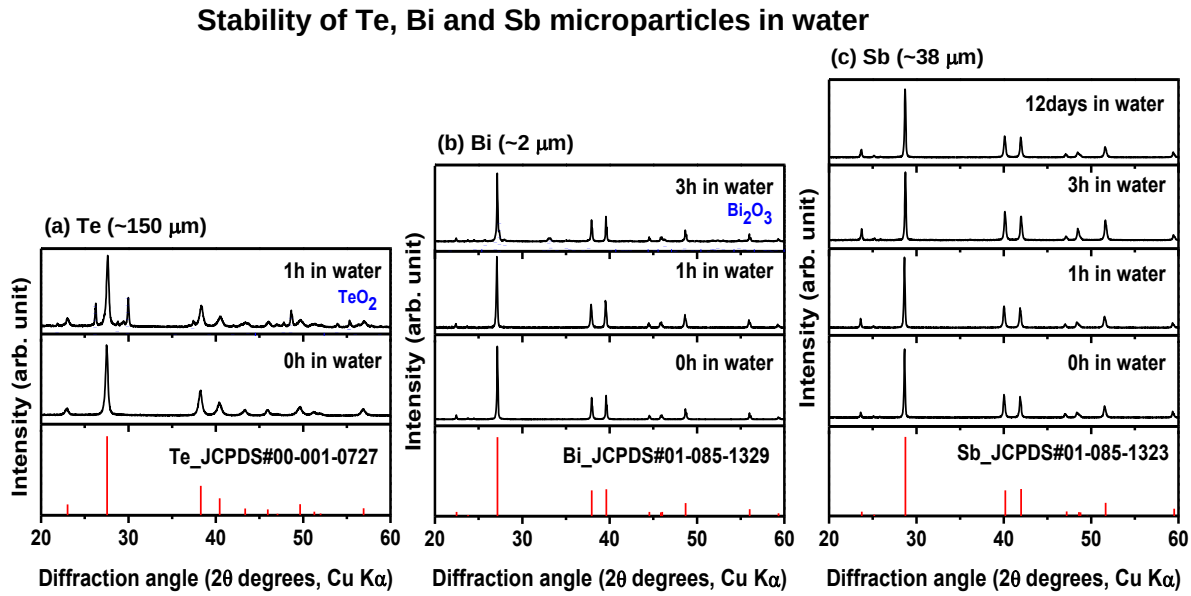

Figure 4.5 Stability of (a) Te microparticles, (b) Bi microparticles, and (c) Sb microparticles in the water as time passed. Te and Bi microparticles were easily oxidized in water in several hours, whereas Sb microparticles did not oxidize for over 10 days in water.

Sb microparticles with particle size of ~38 μm (1 g) were dispersed in an aqueous solution containing water (750 mL), polyvinyl alcohol aqueous solution (5wt%, 200 mL), 2-propanol (10 mL), and $HAuCl_4$ (0.5 m mol). The aqueous solution containing the Sb microparticles was irradiated at room temperature with a ^{60}Co γ-ray source at a dose rate of 0.5 kGy/h for 6 h as described in Figure 4.6. The process for the formation of metallic Au nanoparticles is expressed by the following equations:[33,34)]

$$H_2O \xrightarrow{\gamma\text{-ray}} e^-_{aq.}, H\bullet, OH\bullet \quad (4.1)$$

$$(CH_3)_2CHOH + OH\bullet \rightarrow (CH_3)_2\bullet COH + H_2O \quad (4.2)$$

$$(CH_3)_2CHOH + H\bullet \rightarrow (CH_3)_2\bullet COH + H_2 \quad (4.3)$$

$$Au^{n+} + ne^-_{aq.} \rightarrow Au \quad (4.4)$$

$$Au^{n+} + nH\bullet \rightarrow Au + nH^+ \quad (4.5)$$

$$Au^{n+} + n(CH_3)_2\bullet COH \rightarrow Au + n(CH_3)_2CO + nH^+ \quad (4.6)$$

where, equation (4.1) represents radiolysis of water, and equations (4.2) and (4.3) represent radiolysis of 2-propenol. Since the hydrated electron (e^-_{aq}) and H radicals (H•) generated by the

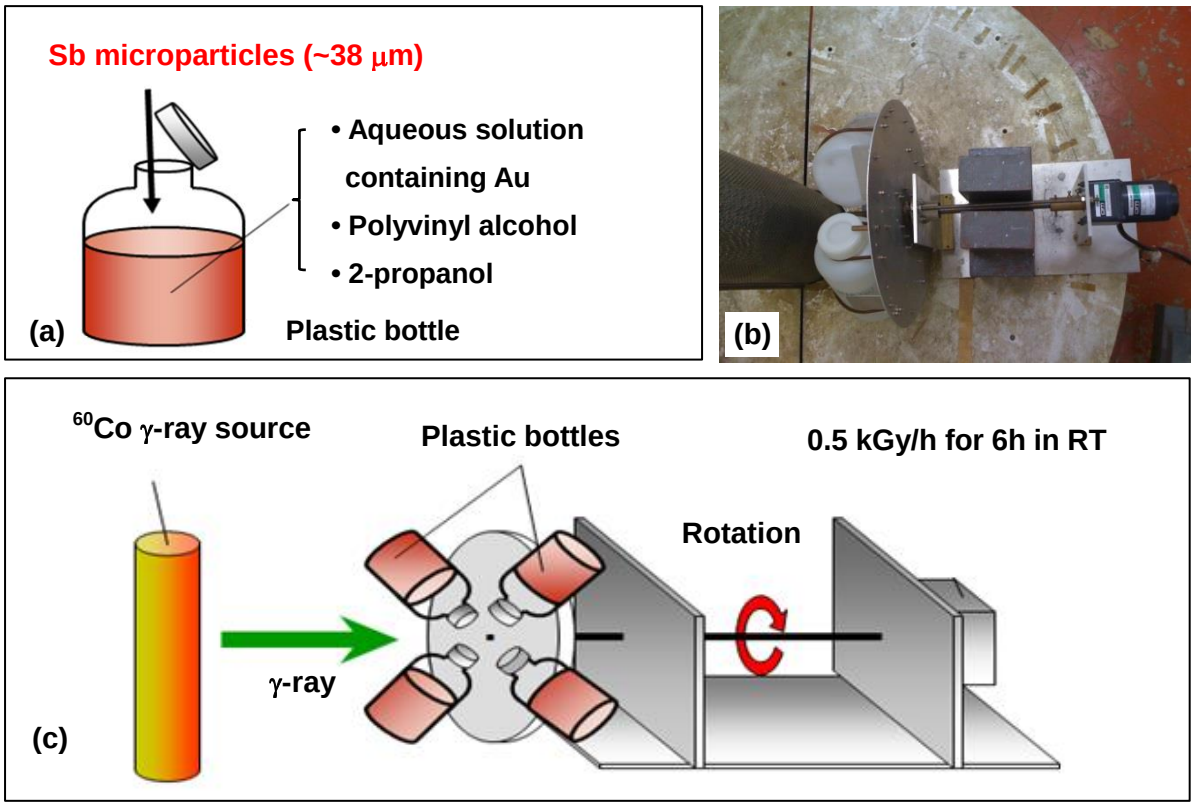

Figure 4.6 Preparation of the γ-ray irradiation; (a) aqueous solution containing the Sb microparticles, (b) apparatus of the γ-ray irradiation, and (c) schematic view of the γ-ray irradiation method.

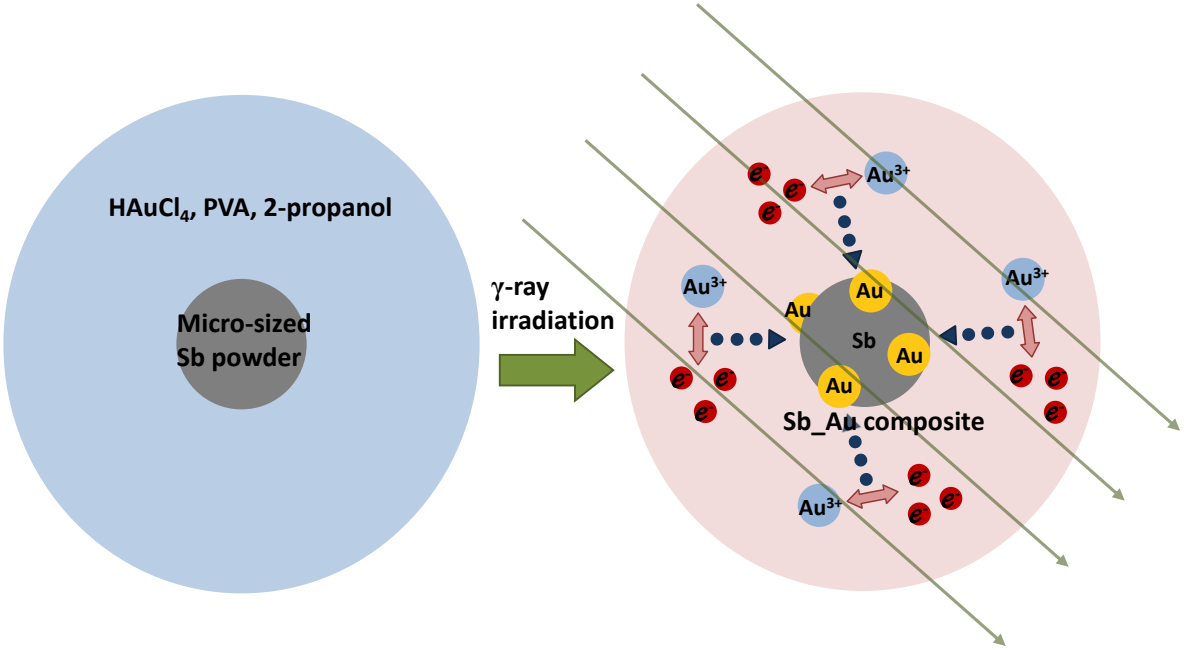

Figure 4.7 Process of the creation of Au nanoparticles on the surface of Sb particles during γ-ray irradiation. Hydrated electron (e^-_{aq}) and H radicals (H•) generated by the γ-ray irradiation act as strong reducing agents, and they reduce Au ions down to the metallic state.

γ-ray irradiation act as strong reducing agents, they reduce Au ions down to lower valences and finally the metallic state. In addition, secondary generated $(CH_3)_2$•COH radicals also efficiently reduce Au ions.[35] These *in situ* generated reducing agents transform the Au^{n+} to Au according to equations (4.4), (4.5), and (4.6), leading to the formation of Au nanoparticles as described in Figure 4.7. The reason for the Au nanoparticles being supported on the surface of the microparticles currently remains unclear. After γ-irradiation, the aqueous solution was filtered and dried to obtain the Au nanoparticle-supported Sb microparticles, indicated as Sb_Au hereafter.

Microparticles of Bi (~2 μm), Te (~150 μm), and Sb or Sb_Au were used as starting materials for the ball-milling. Mixtures of these microparticles with chemical composition of Sb : Bi : Te = 1.6 : 0.4 : 3 were mechanically alloyed (MA) by planetary ball-milling using a WC pot and balls to prepare the $Sb_{1.6}Bi_{0.4}Te_3$ alloy or a nanocomposite composed of Au nanoparticles and $Sb_{1.6}Bi_{0.4}Te_3$, designated as $Sb_{1.6}Bi_{0.4}Te_3$_Au hereafter. The rotating speed of the ball milling was maintained at 450 rpm and the weight ratio of the balls to powders was set at 10 : 1. The microparticles obtained after MA were hot-pressed in a graphite die at 693 K for 1.5 hours in an Ar flow to obtain bulk samples. The samples were characterized using powder X-ray diffraction (XRD, Rigaku RINT2000) using Cu $K\alpha$ radiation. The nanostructure of the samples was examined using field emission scanning electron microscopy (FE-SEM) and high angle annular dark-field (HAADF) scanning transmission electron microscopy (STEM). ρ and S were measured using a ZEM-1 (ULVAC) apparatus in a He atmosphere from room temperature to 523 K. κ was calculated using the equation $\kappa = \alpha C_p d$, where α, C_p and d are the thermal diffusivity, heat capacity, and density, respectively. α was measured by a laser flash method using a TC-7000 (ULVAC) apparatus in the temperature range from 323 K to 523 K. C_p was estimated using the Dulong–Petit law, that is, $C_p = 3nR$, where n is the number of atoms per formula unit and R is the gas constant. The bulk density of the samples was calculated based on the measured mass and dimension. High-density samples (over 99% of the theoretical density) were obtained in the present study. The Hall coefficient (R_H) was measured by the Van der Pauw method using Resitest 8300 (Toyo Co. Ltd.) apparatus at room temperature under an applied magnetic field of 0.5 T. The Hall carrier concentration (n_H) and Hall mobility (μ_H) were calculated from R_H, assuming a single band model and a Hall factor of 1; i.e., $n_H = 1/eR_H$ and $\mu_H = R_H/\rho$, where e is the elementary electric charge.

4.1.3 Results and Discussion

Figures 4.8(a) and (b) shows the FE-SEM and TEM images of a Sb_Au particle, respectively. The images clearly reveal that Au nanoparticles are dispersed and immobilized on the surface of the Sb microparticle. Figures 4.8(c) shows the TEM image of the $Sb_{1.6}Bi_{0.4}Te_3$_Au powders after MA. As seen in the picture, the Au particles retain their nanosize and are dispersed in the $Sb_{1.6}Bi_{0.4}Te_3$ phase during ball-milling. An FE-SEM image of the fracture surface of a hot-pressed bulk sample of $Sb_{1.6}Bi_{0.4}Te_3$_Au is shown in Figures 4.8(d). It can be seen that Au nanoparticles with a size of 10~100 nm (one nanoparticle is indicated by an arrow) were embedded into the $Sb_{1.6}Bi_{0.4}Te_3$ matrix phase without aggregation.

The SEM image and elemental maps obtained by EDX are shown in Figure 4.9. These images indicate that the hot-pressed sample is homogeneous and Bi, Sb, Te, and Au are uniformly distributed. In addition, nanoparticles in the matrix phase were confirmed through FE-SEM observation. The quantitative EDX analysis confirmed that the chemical composition of the hot-pressed sample was consistent with the stoichiometric composition.

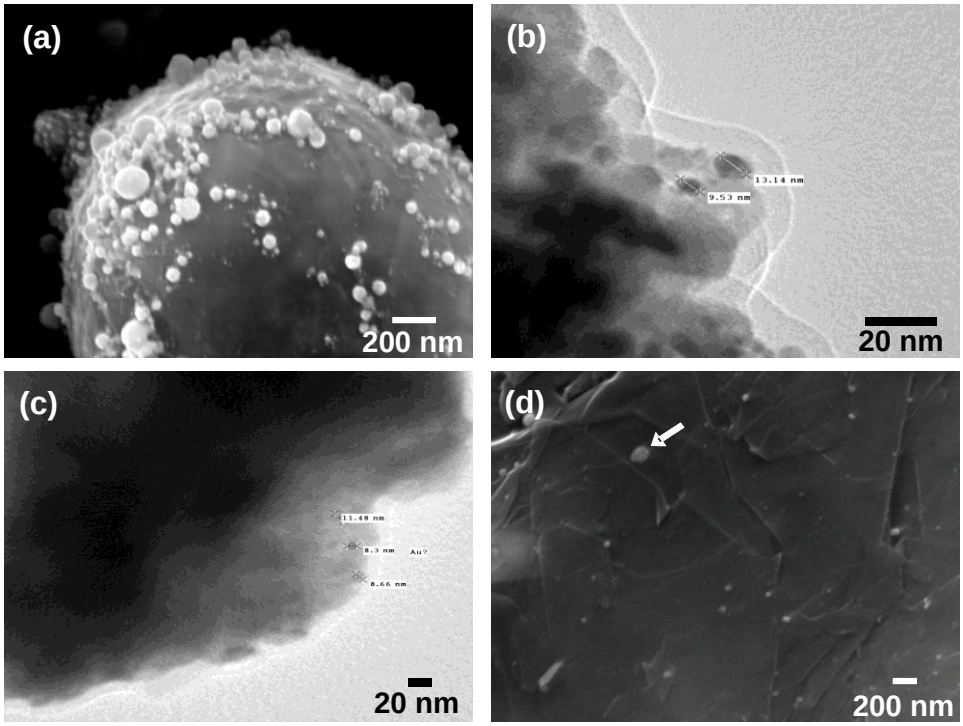

Figure 4.8 (a) SEM and (b) TEM images of Sb_Au composite after γ-ray irradiation. Nano-sized Au nanoparticles are supported on the surface of Sb particle. (c) TEM image of a $Sb_{1.6}Bi_{0.4}Te_3$_Au after ball-milling. (d) SEM image of $Sb_{1.6}Bi_{0.4}Te_3$_Au bulk sample. Au particles retain their nanosize during ball-milling and hot-pressing. One of the nanoparticles is indicated by an arrow.

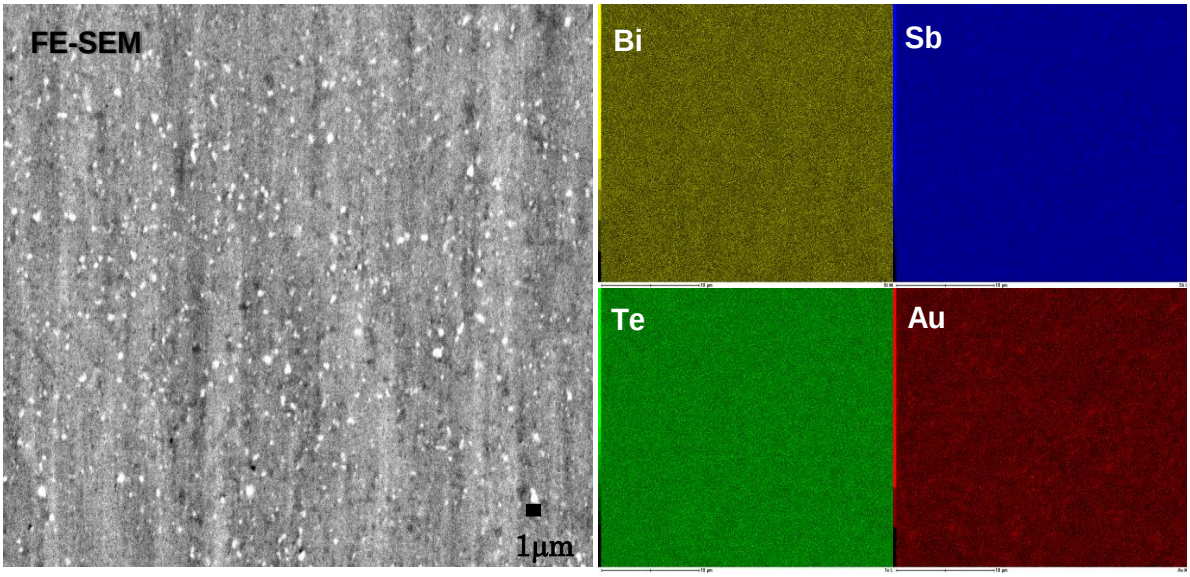

Figure 4.9 FE-SEM and EDX mapping images of the hot-pressed sample of $Sb_{1.6}Bi_{0.4}Te_3$_Au. The nanoparticles were dispersed in the matrix phase.

Table 4.1 Atomic percentage of Au concentration in each process.

	Initial concentration of each content in the aqueous solution (%)	**Concentration of each content after irradiation (%)**	**Concentration of each content after hot-pressing (%)**
Au	5.81	4.73	1.28
Sb	94.19	95.27	29.41
Bi			8.56
Te			60.75
Sb/Au	**6.17**	**4.96**	**4.35**

The atomic percentage of Au nanoparticles to Sb particles after the ball-milling and hot-pressing were calculated by EDX analysis. The results are summarized in Table 4.1. Initial atomic ratio of Sb/Au was set 6.17 %. However, the Au concentration of Sb_Au composites reduced to 4.96 % during the irradiation, meaning that about 81.4% of the initial concentration of Au was supported on the surface of Sb particles. Finally, the atomic ratio of Sb/Au in the hot-pressed bulk sample was 4.35 %. This loss of Au content is considered to be occurred during ball-milling process.

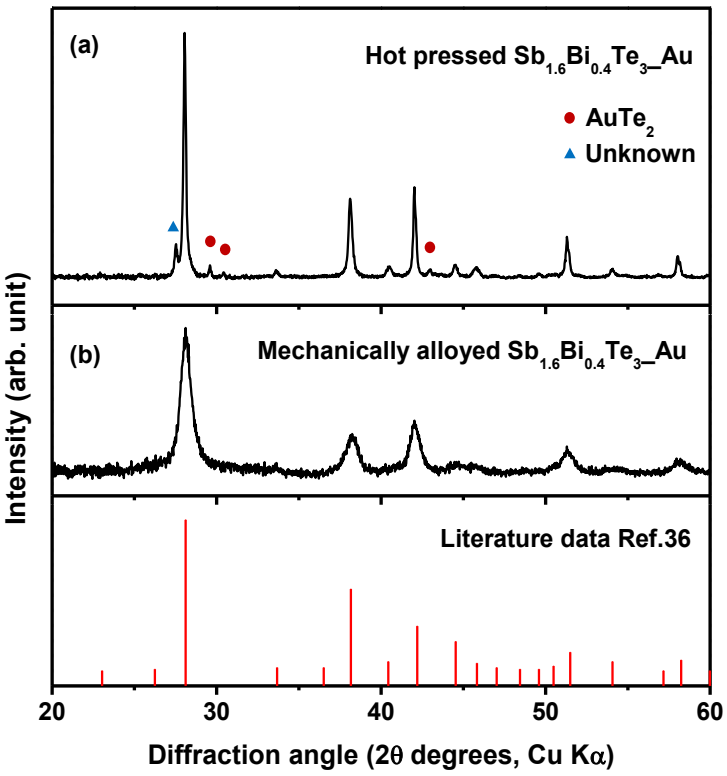

Figure 4.10 Powder XRD patterns of (a) hot-pressed and (b) mechanically alloyed $Sb_{1.6}Bi_{0.4}Te_3$_Au, together with the peak positions of $Sb_{1.5}Bi_{0.5}Te_3$ reported in Ref. 36.

XRD patterns of the $Sb_{1.6}Bi_{0.4}Te_3$_Au samples before and after hot-pressing are shown in Figures 4.10(a) and (b), respectively. As shown in Figure 4.10(b), the MAed powders before hot-pressing had a single phase, consistent with the reference data for the BiSbTe alloy.[36] However, as shown in Figure 4.10(a), some $AuTe_2$ peaks as well as an unknown peak were detected in the XRD pattern of the hot-pressed sample. Although, from the FE-SEM image shown in Figure 4.8(d), Au nanoparticles were clearly detected in the hot-pressed sample, peaks of elemental Au were not confirmed in the XRD pattern.

To confirm Au, $AuTe_2$ and unknown particles into the $Sb_{1.6}Bi_{0.4}Te_3$ matrix phase, high angle annular dark-field (HAADF) scanning transmission electron microscopy (STEM) was carried out. HAADF-STEM images and energy dispersive x-ray (EDX) spectroscopy line scanprofiles of nanoparticles present on the surface of the $Sb_{1.6}Bi_{0.4}Te_3$_Au bulk sample are shown in Figure 4.11. As seen in the HAADF-STEM images, two types of nanoparticles with size of 100~300 nm were confirmed. As shown in the EDX spectroscopy line scan profiles, the first

nanoparticle(indicated by the red line 1) is mainly composed of Au, while the second nanoparticle (indicated by the red line 2) is mainly composed of Au and Te. From the XRD results, HAADF-STEM observations, and EDX spectroscopy line scan analysis, it can be concluded that two kinds of nanoparticles, i.e., nanoparticles of elemental Au and $AuTe_2$, were present in the $Sb_{1.6}Bi_{0.4}Te_3$ For the unknown particles, although the unknown peak position in the XRD pattern is most close to Te peak and Poudel reported for nanostructured BiSbTe alloy that the Te phase could be formed during the hot-press heating and cooling process,[3)] I could not observe the Te phase from the microstructure in the present study.

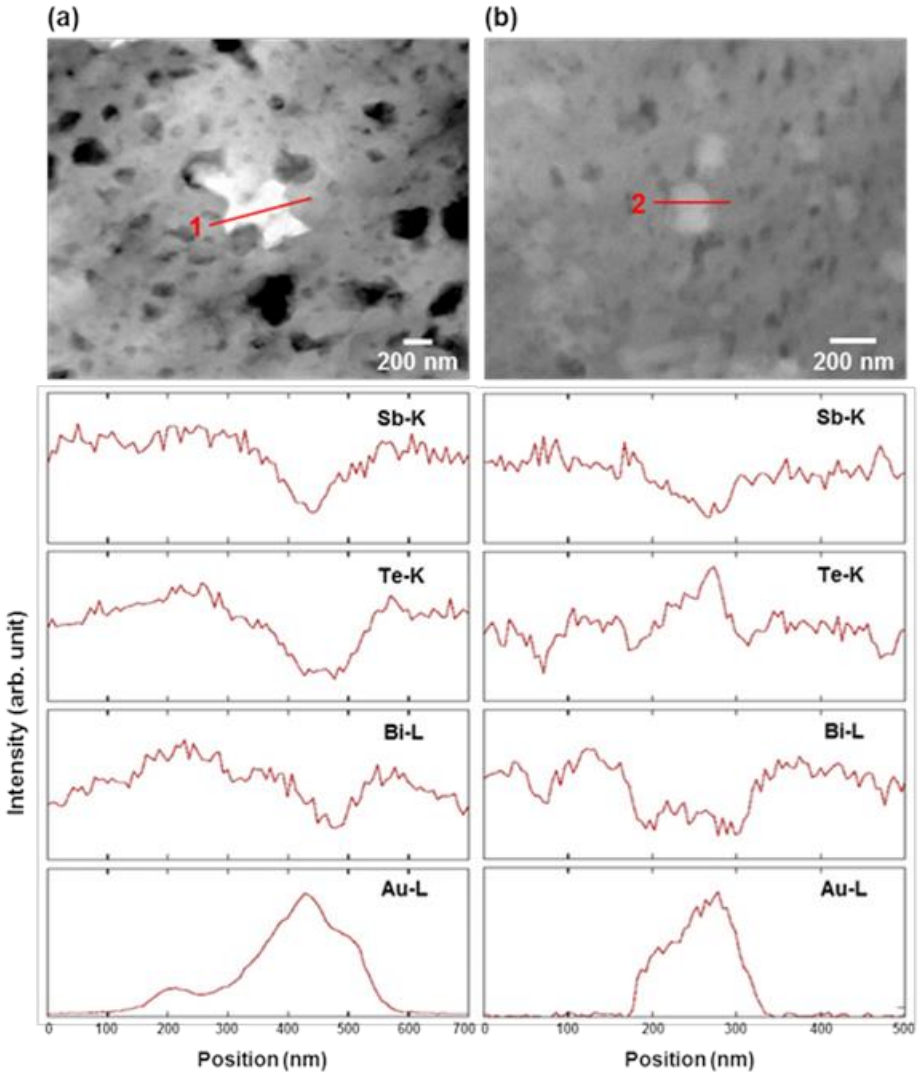

Figure 4.11 HAADF-STEM images and EDX spectroscopy line scan profiles of (a) an Au nanoparticles and (b) nanoparticles of an Au-Te binary compound present on the surface of the $Sb_{1.6}Bi_{0.4}Te_3$_Au bulk sample

The temperature dependence of ρ of the hot-pressed bulk samples of $Sb_{1.6}Bi_{0.4}Te_3$_Au and $Sb_{1.6}Bi_{0.4}Te_3$ are shown in Figure 4.12. As shown in Figure 4.12, ρ for both samples increased with increasing temperature, indicating degenerate semiconducting behavior. The ρ of $Sb_{1.6}Bi_{0.4}Te_3$_Au is slightly lower than that of $Sb_{1.6}Bi_{0.4}Te_3$ in the whole temperature range. According to the results of Hall effect measurements at room temperature as summarized in Table 4.2, this decrease in ρ is mainly caused by the increase in n_H. It is considered that this increase in n_H of $Sb_{1.6}Bi_{0.4}Te_3$_Au is due to the formation of $AuTe_2$ during hot-pressing. When Au nanoparticles react with Te forming $AuTe_2$, the Te concentration of the BiSbTe matrix phase decreases and thereby, the hole concentration increases.[37] As for μ_H, the value for $Sb_{1.6}Bi_{0.4}Te_3$_Au is slightly lower than the value for $Sb_{1.6}Bi_{0.4}Te_3$. This is due to an increase in carrier scattering at the interfaces between Au/$AuTe_2$ nanoparticles and the BiSbTe matrix phase.

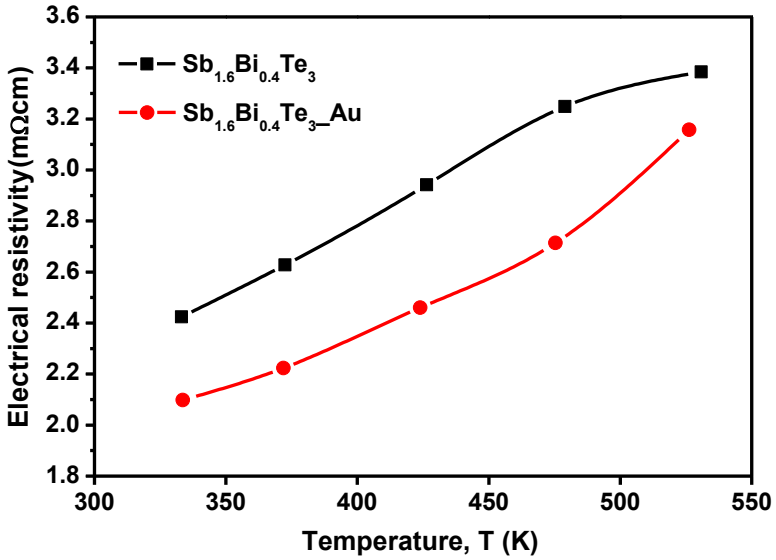

Figure 4.12 Temperature dependence of the electrical resistivity of the $Sb_{1.6}Bi_{0.4}Te_3$_Au bulk sample as compared to those of $Sb_{1.6}Bi_{0.4}Te_3$.

Table 4.2 Carrier concentration and mobility at room temperature of bulk samples

Sample	Carrier concentration, n_H (cm^{-3})	Carrier mobility, μ_H ($cm^2V^{-1}s^{-1}$)
$Sb_{1.6}Bi_{0.4}Te_3$_Au	5.10×10^{19}	69.8
$Sb_{1.6}Bi_{0.4}Te_3$	3.85×10^{19}	82.1

The *S* value for both samples is positive, as shown in Figure 4.13, indicating that the majority charge carriers are holes. The *S* of $Sb_{1.6}Bi_{0.4}Te_3$_Au is smaller than that of $Sb_{1.6}Bi_{0.4}Te_3$ at room temperature due to the larger n_H of $Sb_{1.6}Bi_{0.4}Te_3$_Au compared to that of $Sb_{1.6}Bi_{0.4}Te_3$. *S* for both samples showed a similar temperature dependence, where *S* reached maximum values at ~420 K and then decreased. The decreasing *S* above ~420 K would be caused by a bipolar contribution arising from the diffusion of electron-hole pairs. Since the intrinsic excitation of minority carriers (in the present case, electrons) would become strong with increasing temperature, the impact of the bipolar diffusion on *S* would become strong, leading to a decrease in *S* at high temperatures.[38] Since the number of majority carriers (in the present case, holes) in $Sb_{1.6}Bi_{0.4}Te_3$_Au is larger than that in $Sb_{1.6}Bi_{0.4}Te_3$, the bipolar effect caused by the excitation of minority carriers in $Sb_{1.6}Bi_{0.4}Te_3$_Au would be smaller than that in $Sb_{1.6}Bi_{0.4}Te_3$. As a result, the *S* of $Sb_{1.6}Bi_{0.4}Te_3$_Au showed a relatively slow decrease over ~420 K compared to $Sb_{1.6}Bi_{0.4}Te_3$.

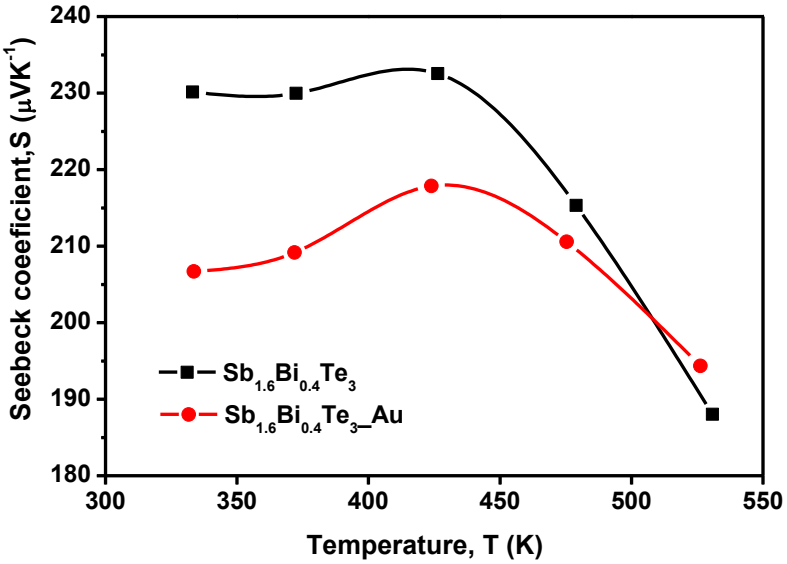

Figure 4. 13 Temperature dependences of the Seebeck coefficient *S*, of the $Sb_{1.6}Bi_{0.4}Te_3$_Au bulk sample as compared with those of $Sb_{1.6}Bi_{0.4}Te_3$.

The *S* as a function of carrier concentration is potted to confirm the low energy carrier filtering effect in Figure 4.14. The dashed lines in Figure 4.14 were calculated for m* = 1.3 and 1.4 m_e, respectively, assuming a single parabolic band and approximates energy-independent carrier scattering in degenerate semiconductors[39] with following equation:

$$S = \frac{8\pi^2 k_B^2}{3eh^2} m^* T \left(\frac{\pi}{3n}\right)^{\frac{2}{3}} \tag{4.7}$$

where k_B, h, m^*, and T are the Boltzmann constant, Planck constant, effect electron mass and absolute temperature, respectively. The $Sb_{1.6}Bi_{0.4}Te_3$_Au have higher effective mass than the $Sb_{1.6}Bi_{0.4}Te_3$ with a comparable carrier concentration. This slight increase in the effective mass of the carrier is considered to be the evidence of energy-dependent electronic scattering of the carrier by the formation of a potential barrier between at the nanoparticles and $Sb_{1.6}Bi_{0.4}Te_3$ interfaces. As a result, the enhancement in the S of $Sb_{1.6}Bi_{0.4}Te_3$_Au for a given carrier concentration could be demonstrated.

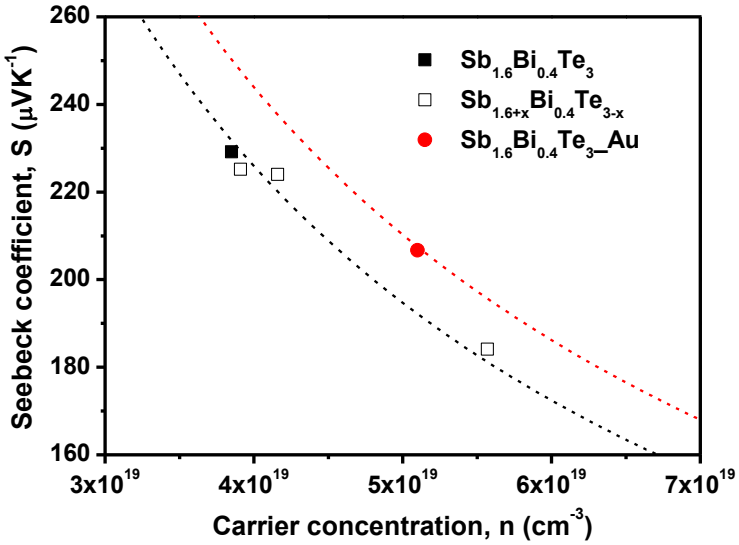

Figure 4. 14 Seebeck coefficient as a function of carrier concentration for $Sb_{1.6+x}Bi_{0.4}Te_{3-x}$ and $Sb_{1.6}Bi_{0.4}Te_3$_Au. The dashed lines correspond to the calculation S according to equation m^* being 1.3 m_e and 1.4 m_e for black dash line and red dash line, respectively.

Figure 4.15 shows the S^2/ρ for both samples. The S^2/ρ values of $Sb_{1.6}Bi_{0.4}Te_3$_Au are similar to those of $Sb_{1.6}Bi_{0.4}Te_3$ over the whole temperature range. Although the formation of $AuTe_2$ increased n_H of $Sb_{1.6}Bi_{0.4}Te_3$_Au and led to a change in ρ and S as compared to $Sb_{1.6}Bi_{0.4}Te_3$, it did not have a negative effect on the S^2/ρ of $Sb_{1.6}Bi_{0.4}Te_3$_Au.

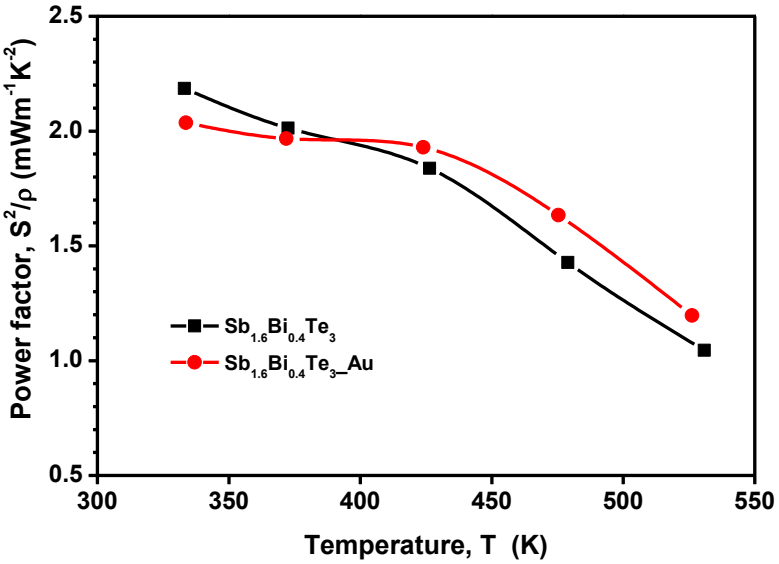

Figure 4. 15 Temperature dependences of the power factor S^2/ρ, of the $Sb_{1.6}Bi_{0.4}Te_3$_Au bulk sample as compared with those of $Sb_{1.6}Bi_{0.4}Te_3$.

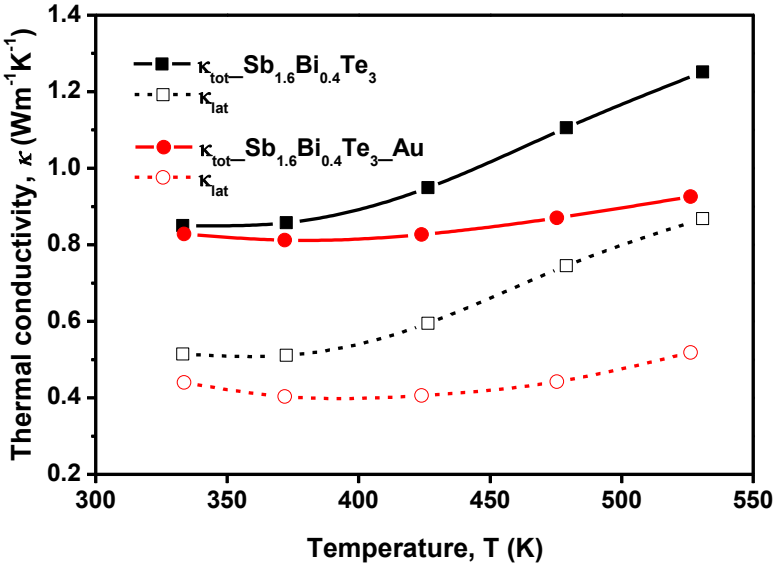

Figure 4. 16 Temperature dependences of the thermal conductivity κ, of the $Sb_{1.6}Bi_{0.4}Te_3$_Au bulk sample as compared with those of $Sb_{1.6}Bi_{0.4}Te_3$.

The temperature dependence of κ_{total} and κ_{lat} of the hot-pressed bulk samples of $Sb_{1.6}Bi_{0.4}Te_3$_Au and $Sb_{1.6}Bi_{0.4}Te_3$ are shown in Figure 4.16. κ_{lat} was roughly calculated by subtracting the electronic contribution ($\kappa_{el} = LT/\rho$, where L is the Lorentz number = 2.45×10^{-8} $W\Omega K^{-2}$) from the measured κ, i.e, $\kappa_{lat} = \kappa - LT/\rho$. Note that here, κ_{lat} contains both lattice and

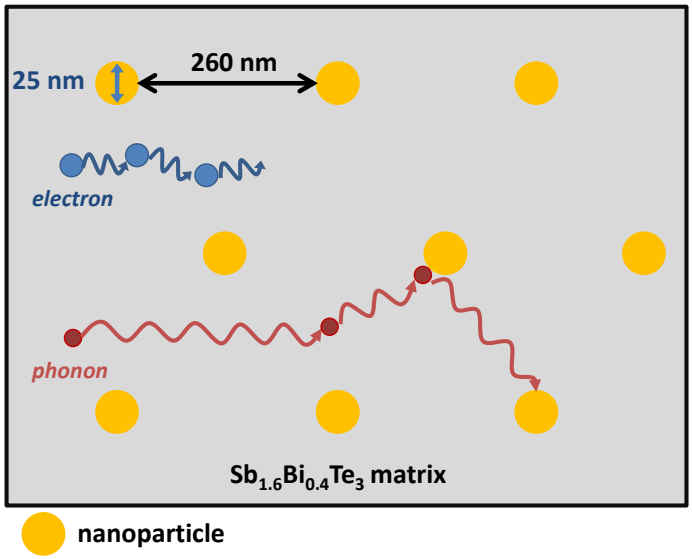

Figure 4.17 Schematic diagram illustrating phonon scattering mechanism within $Sb_{1.6}Bi_{0.4}Te_3$_Au.

Table 4.3. Electron and phonon MFPs of Bi_2Te_3 and Si nanowire

	Electron MFP	Phonon MFP
Bi_2Te_3[40-42)]	60 nm	~ 1000 nm
Si nanowire[43)]	110 nm	~ 300 nm

bipolar contribution. As shown in Figure. 4.16, κ of $Sb_{1.6}Bi_{0.4}Te_3$_Au is significantly lower than the κ of $Sb_{1.6}Bi_{0.4}Te_3$ over the entire temperature range, as expected due to the increased interfaces which induce phonon scattering. Nanoparticles of both $AuTe_2$ and Au dispersed in the $Sb_{1.6}Bi_{0.4}Te_3$ matrix phase would scatter mid- and long-wavelength phonons effectively. As a result, the effective phonon mean free path (MFP) in $Sb_{1.6}Bi_{0.4}Te_3$_Au would be decreased as seen in Figure 4.17. Generally, it is known that the inter-dot distance or the size of nanograin should be larger than the electron MFP and smaller than that of phonon to affect the phonon transport behavior, selectively.[44)] The electron and phonon MFPs of Bi_2Te_3 are listed in Table 4.3, together with Si nanowire. According to reference, phonon MFP of Bi_2Te_3 is larger than that of electron at room temperature, and the distance between nanoparticles in the present study is about 260 nm. Therefore, it can be concluded that the phonon MFP is influenced by the present of Au and $AuTe_2$ nanoparticles, leading to a reduction in κ_{lat}. Additionally, it should be noted that κ for $Sb_{1.6}Bi_{0.4}Te_3$_Au showed a slow increase at high temperature, in contrast to $Sb_{1.6}Bi_{0.4}Te_3$. This phenomenon also could be explained the reduced bipolar effect. While the bipolar diffusion contribution in κ would be dominant for the $Sb_{1.6}Bi_{0.4}Te_3$ at high temperature, as for

$Sb_{1.6}Bi_{0.4}Te_3$_Au, the majority carriers (in this case, holes) contribution in κ would be dominant due to the increased n_H which suppress the bipolar diffusion contribution. In addition, the existence of interfacial potentials between Au/$AuTe_2$ nanoparticles and the $Sb_{1.6}Bi_{0.4}Te_3$ matrix might have helped to reduce the bipolar effect. Previously, the nanostructured *p*-type $Bi_xSb_{2-x}Te_3$ alloy reported by Poudel showed a similar slow increase in κ at high temperature.[3)] They explained this phenomenon as being due to a reduced bipolar effect assuming that minority carriers (in this case, electrons) are more strongly scattered by the grain boundaries than the majority carriers (in this case, holes), resulting in a decreased minority carrier contribution to the transport properties especially at high temperatures.[7,45,46)] I believe that in the present case, the interfacial potentials between nanoparticles and the matrix would scatter more electrons than holes. As a result, $Sb_{1.6}Bi_{0.4}Te_3$_Au maintains a relatively low κ compared to $Sb_{1.6}Bi_{0.4}Te_3$ at high temperature, and this low κ would lead to further enhancement in *ZT* of $Sb_{1.6}Bi_{0.4}Te_3$_Au.

The figure of merit *ZT* was calculated based on the measured TE properties, and the results are shown in Figure. 4.18 as a function of temperature. As shown in Figure. 4.18, the error bars on the *ZT* data for the $Sb_{1.6}Bi_{0.4}Te_3$_Au sample are larger than the error bars on the *ZT* data for the $Sb_{1.6}Bi_{0.4}Te_3$. The $Sb_{1.6}Bi_{0.4}Te_3$ sample showed no hysteresis in the TE properties during measurements. On the other hand, the $Sb_{1.6}Bi_{0.4}Te_3$_Au sample showed slightly different TE data

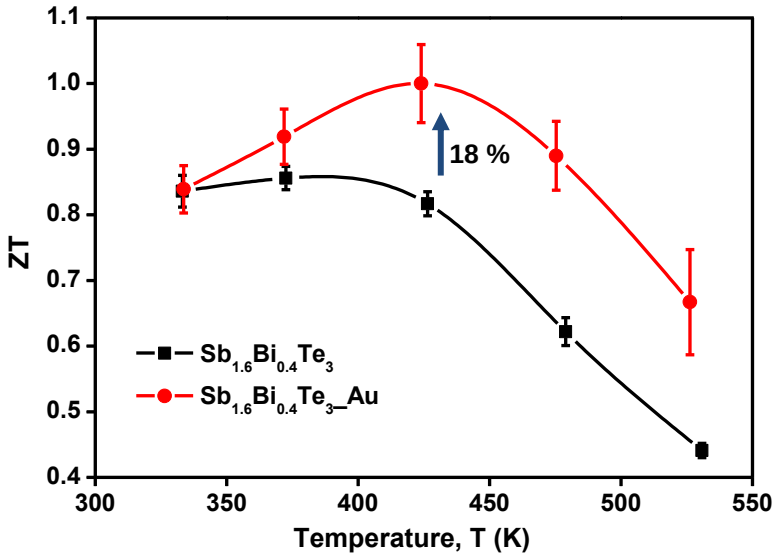

Figure 4. 18 Temperature dependences of the dimensionless figure of merit *ZT*, of the $Sb_{1.6}Bi_{0.4}Te_3$_Au bulk sample as compared with those of $Sb_{1.6}Bi_{0.4}Te_3$. Considering the uncertainty in the measurement of electrical resistivity, Seebeck coefficient, and thermal diffusivity, the error bars are a maximum of 5.8 % for *ZT*.

in heating and cooling cycles during measurements in the temperature range from room temperature to 523 K. This would be due to Au diffusing into the SbBiTe alloy at high temperatures. This is the reason why the error bars on the *ZT* data for the $Sb_{1.6}Bi_{0.4}Te_3$_Au sample are larger than the error bars on the other *ZT* data. In order to determine the thermal stability of the $Sb_{1.6}Bi_{0.4}Te_3$_Au sample, I measured the TE properties in various temperature range. From the experimental results, it was confirmed that the $Sb_{1.6}Bi_{0.4}Te_3$_Au sample is stable and the TE data are reproducible below 473 K.

The *ZT* values of $Sb_{1.6}Bi_{0.4}Te_3$_Au were clearly higher than those of $Sb_{1.6}Bi_{0.4}Te_3$ over the whole temperature range considered. This is mainly due to a significant reduction in κ_{lat}. In addition, the peak of *ZT* of $Sb_{1.6}Bi_{0.4}Te_3$_Au shifted slightly to a higher temperature compared to $Sb_{1.6}Bi_{0.4}Te_3$. Such *ZT* characteristics are suitable for more widespread TE applications. The maximum *ZT* value obtained in the present study was 1.01 at 423 K, for the polycrystalline hot-pressed $Sb_{1.6}Bi_{0.4}Te_3$_Au sample.

4.1.4 Conclusion

I have proposed a combined method of γ-ray irradiation, ball-milling, and hot-pressing to prepare a nanocomposite of Au/$AuTe_2$ nanoparticles and $Sb_{1.6}Bi_{0.4}Te_3$. I confirmed, by means of FE-SEM and HAADF-STEM observations, that nano-sized Au and $AuTe_2$ particles were uniformly dispersed in the $Sb_{1.6}Bi_{0.4}Te_3$ matrix. The formation of $AuTe_2$ increased n_H of $Sb_{1.6}Bi_{0.4}Te_3$_Au and caused a change in ρ and S as compared to $Sb_{1.6}Bi_{0.4}Te_3$. However, the electrical properties (S^2/ρ) maintained similar values with $Sb_{1.6}Bi_{0.4}Te_3$. The Au and $AuTe_2$ nanoparticles present in the $Sb_{1.6}Bi_{0.4}Te_3$ matrix scattered phonons effectively, resulting in significant reduction in κ_{lat}. Consequently, a peak *ZT* value of about 1.01 at 423 K was achieved, which is about 18% higher than that of $Sb_{1.6}Bi_{0.4}Te_3$. On the basis of these results, the γ-ray irradiation method to synthesize the nanocomposite proved to be effective in reducing κ_{lat}, thereby enhancing the TE properties of the material. Since this method makes it relatively easy to control the particle size and amount, and besides, Pt or Ag could also be used as supporting materials,[31] this suggests that the approach can be applied not only to Sb-based materials but also to other TE materials. The present results thus indicate a new strategy for improvement of bulk TE material properties.

4.1.5 References

1) C. J. Vineis, A. Shakouri, A. Majumdar, and M. G. Kanatzidis, Adv. Mater. **22**, 3970 (2010).
2) J. R. Sootsman, R. J. Pcionek, H. Kong, C. Uher, and M. G. Kanatzidis, Chem. Mater. **18**, 4993 (2006).
3) B. Poudel, Q. Hao, Y. Ma, Y. C. Lan, A. Minnich, B. Yu, X. Yan, D. Z. Wang, A. Muto, D. Vashaee, X. Y. Chen, J. M. Liu, M. S. Dresselhaus, G. Chen, and Z. F. Ren, Science **320**, 634 (2008).
4) N. W. Gothard, T. M. Tritt, and J. E. Spowart, J. Appl. Phys. **110**, 023706 (2011).
5) M. S. Dresselhaus, G. Chen, M. Y. Tang, R. G. Yang, H. Lee, D. Z. Wang, Z. F. Ren, J. P. Fleurial and P. Gogna, Adv. Mater. **19**, 1043 (2007).
6) M. G. Kanatzidis, Chem. Mater. **22**, 648 (2009).
7) W. Kim, J. Zide, A. Gossard, D. Klenov, S. Stemmer, A. Shakouri and A. Majumdar, Phys. Rev. Lett. **96**, 045901 (2006).
8) Y. C. Lan, A. J. Minnich, G. Chen and Z. F. Ren, Adv. Funct. Mater. **20**, 357 (2010).
9) M. S. Toprak, C. Stiewe, D. Platzek, S. Williams, L. Bertini, E. C. Muller, C. Gatti, Y. Zhang, M. Rowe and M. Muhammed, Adv. Funct. Mater. **14**, 1189 (2004).
10) W. J. Xie, J. A. He, H. J. Kang, X. F. Tang, S. Zhu, M. Laver, S. Y. Wang, J. R. D. Copley, C. M. Brown, Q. J. Zhang and T. M. Tritt, Nano Lett. **10**, 3283 (2010).
11) X. B. Zhao, S. H. Yang, Y. Q. Cao, J. L. Mi, Q. Zhang and T. J. Zhu, J. Electron. Mater. **38**, 1017 (2009).
12) J. Zhou, X. B. Li, G. Chen and R. G. Yang, Phys. Rev. B: Condens. Matter Mater. Phys. **82**, 115308 (2010).
13) J. R. Sootsman, D. Y. Chung and M. G. Kanatzidis, Angew. Chem. **48**, 8616 (2009).
14) J. P. Heremans, C. M. Thrush and D. T. Morelli, Phys. Rev. B: Condens. Matter Mater. Phys. **70**, 115334 (2004).
15) H. Ohta, S. Kim, Y. Mune, T. Mizoguchi, K. Nomura, S. Ohta, T. Nomura, Y. Nakanishi, Y. Ikuhara, M. Hirano, H. Hosono and K. Koumoto, Nat. Mater. **6**, 129 (2007).
16) J. M. O. Zide, D. Vashaee, Z. X. Bian, G. Zeng, J. E. Bowers, A. Shakouri and A. C. Gossard, Phys. Rev. B: Condens. Matter Mater. Phys. **74**, 205335 (2006).
17) J. Martin, L. Wang, L. Chen and G. S. Nolas, Phys. Rev. B: Condens. Matter **79**, 1153111 (2009).
18) W. Kim, J. Zide, A. Gossard, D. Klenov, S. Stemmer, A. Shakouri, and A. Majumdar, Phys. Rev. Lett. **96**, 045901 (2006).

19) L. D. Zhao, B. P. Zhang, J. F. Li, M. Zhou, W. S. Liu, and J. Li, J. Alloys Compd. **455**, 259 (2008).

20) P. N. Alboni, X. Ji, J. He, N. W. Gothard, and T. M. Tritt, J. Appl. Phys. **103**, 113707 (2008).

21) X. Zhou, G. Wang, L. Zhang, H. Chi, X. Su, J. Sakamoto, and C. Uher, J. Mater. Chem. **22**, 2958 (2012).

22) D. Vashaee and A. Shakouri, Phys. Rev. Lett. **92**, 106103 (2004).

23) J. P. Heremans, C. M. Thrush and D. T. Morelli, J. Appl. Phys. **98**, 063703 (2005).

24) A. J. Minnich, M. S. Dresselhaus, Z. F. Ren and G. Chen, Energy Environ. Sci. **2**, 466 (2009).

25) Y. Ma, Q. Hao, B. Poudel, Y. Lan, B. Yu, D. Wang, G. Chen, and Z. F. Ren, Nano Lett. **8**, 2580 (2008).

26) X. W. Wang, H. Lee, Y. C. Lan, G. H. Zhu, G. Joshi, D. Z. Wang, J. Yang, A. J. Muto, M. Y. Tang, J. Klatsky, S. Song, M. S. Dresselhaus, G. Chen, and Z. F. Ren, Appl. Phys. Lett. **93**, 193121 (2008).

27) R. Heijl, D. Cederkrantz, M. Nygren, and A. E. C. Palmqvist, J. Appl. Phys. **112**, 044313 (2012).

28) H. Wang, J. F. Li, C. W. Nan, M. Zhou, W. S. Liu, B. P. Zhang, and T. Kita, Appl. Phys. Lett. **88**, 092104 (2006).

29) S. K. Bux, M. T. Yeung, E. S. Toberer, G. J. Snyder, R. B. Kaner, and J. P. Fleurial, J. Mater. Chem. **21**, 12259 (2011).

30) L. D. Chen, X. Y. Huang, M. Zhou, X. Shi and W. B. Zhang, J. Appl. Phys. **99**, 064305 (2006).

31) S. Seino, T. Kinoshita, Y. Otome, T. Maki, T. Nakagawa, K. Okitsu, Y. Mizukoshi, T. Nakayama, T. Sekino, K. Niihara, and T. A. Yamamoto, Scripta Mater. **51**, 467 (2004).

32) S. Seino, T. Kinoshita, T. Nakagawa, T. Kojima, R. Taniguci, S. Okuda, and T. A. Yamamoto, J. Nanopart. Res. **10**, 1071 (2008).

33) A. J. Minnich, M. S. Dresselhaus, Z. F. Ren, and G. Chen, Energy Environ. Sci. **2**, 466 (2009).

34) J. Belloni, M. Mostafavi, H. Remita, J. L. Marignier, and M. O. Delcourt, New J. Chem. **22**, 1239 (1998).

35) E. Gachard, H. Remita, J. Khatouri, B. Keita, L. Nadjo, and J. Belloni, New J. Chem. **22**, 1257 (1998).

36) J. Ritter, National Inst. of Standards and Technology (Gaithersburg, MD, USA, 1997).

37) T. Thonhauser, G. S. Jeon, G. D. Mahan, and J. O. Sofo, Phys. Rev. B **68**, 205207 (2003).

38) D. M. Rowe, V. S. Shukla, and N. Savvides, Nature **290**, 765 (1981).

39) G. J. Snyder and E. S. Toberer, Nat. Mater. **7**, 105 (2008).

40) A. Mavrokefalos, A. L. Moore, M. T. Pettes, L. Shi, W. Wang, and X. Li, Journal of applied physics **105**, 104318 (2009).

41) D.H. Kim et al., Journal of alloys and compounds **399**, 14(2005).

42) J. Y. Yang et al., Journal of alloys and compounds **312**, 326 (2000).

43) A. I. Hochbaum, R. Chen, R. D. Delgado, W. Liang, E. C. Garnett, M. Najarian, A. Majumdar and P. Yang, nature **451**, 163 (2008).

44) C. Kang, H. Kim, S. Park, and W. Kim, Applied physics letter **96**, 213114 (2010)

45) Y. Lan, B. Poudel, Y. Ma, D. Wang, M. S. Dresselhaus, G. Chen, and Z. F. Ren, Nano Lett. **9**, 1419 (2009).

46) H. A. Schwarz, and R. W. Dodson, J. Phys. Chem. **93**, 409 (1989).

4.2 Mechanical Properties of Au nanoparticle-supported $Sb_{1.6}Bi_{0.4}Te_3$ Nanocomposite

As I have already explained in chapter 4.1, the Au and $AuTe_2$ nanoparticles into the $Sb_{1.6}Bi_{0.4}Te_3$ matrix contributed to reduce the lattice thermal conductivity, thereby enhancing the TE performance. This section is focused on mechanical properties such as Vickers hardness, fracture toughness, Young's modulus, and thermal expansion of Au nanoparticles-supported $Sb_{1.6}Bi_{0.4}Te_3$ nanocomposite. I evaluated the effect of the Au and $AuTe_2$ nanoparticles on such mechanical properties in this chapter.

4.2.1 Introduction

TE materials usually work under a cyclic temperature gradient, which would cause an inhomogeneous thermal expansion. This induces serious stress and strain within the device that could result in crack and consequently degradation of the TE performance. The TE module consists of semiconductor legs connected electrically in series. As shown in Figure 4.19(a), these legs are usually soldered to copper interconnects. These connections create thermally conductivity but mechanically brittle metallic bond. The large temperature gradients across TE modules and the large number of thermal cycles during operation lead to performance degradation and device failure at this interfaces.[1] For example, Barako *et al*. showed experimental evidence using a Bi_2Te_3-alloys for modern commercial module.[2] When one side of TE module is exposed to 420 K and cools to 250 K over a period of 60 seconds during thermal cycling, after 45,000 cycles, the TE module showed a partial crack at the soldered interface as shown in Figures 4.19(b) and (c). Consequently, the crack formation at the interface resulted in the degradation of TE performance due to the increase in ρ.

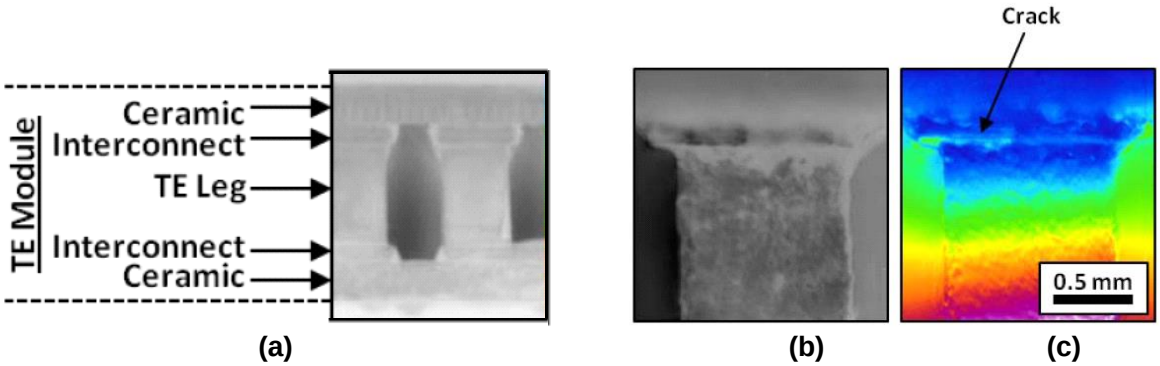

Figure 4.19 (a) Grayscale intensity image of TE module, (b) optical and (c) infrared image of a damaged solder interface between the interconnect and TE leg.[2]

For the reason, TE materials in TE module need to be mechanically strong and the comparison of the thermal expansion coefficient between the TE materials and interconnect should be considered to withstand such condition. Therefore, knowledge of mechanical properties about TE materials is also essential at the point of machining reliability and system integration.[3] The cleavage problem in a single crystalline Bi_2Te_3-based ingot fabricated by a Bridgman, Czochralski and zone melting technics[4-6] is an example of unsatisfactory performance due to mechanical unreliability.[7] They exhibit poor mechanical properties such as Vickers hardness, Young's modulus and fracture toughness due to the existence of the van der Waals bonding between Te(1)–Te(1) layers in the crystal structure.[7] However, recently, nanostructuring of Bi_2Te_3-based polycrystalline bulk materials has been proven to be effective way to improve not only the TE properties but also the mechanical properties.[8-10] For instance, Zhao et al. showed the enhancement of mechanical properties including Vickers hardness, Young's modulus and fracture toughness for the nano-SiC-dispersed Bi_2Te_3.[10] With this background, the mechanical properties such as Vickers hardness, Young's modulus, fracture toughness, and thermal expansion of the Au nanoparticles-supported $Sb_{1.6}Bi_{0.4}Te_3$ nanocomposite were examined and the results will be discussed in this chapter.

4.2.2 Experimental Procedures

For the measurements of mechanical properties, the same samples which were fabricated in chapter 4.1.2 were used. Hardness (H) and Young's modulus (E) were determined by indentation tests using a dynamic ultra microhardness tester(DUH-211S, Shimadzu) at room temperature. The maximum load was chosen to be 10, 30, 50, 100, 200, 500, 980 mN under a loading and unloading times of 15 s. The Vickers hardness was also measured using a Vickers hardness tester (MHT-1, Matsuzawa) under the maximum load of 980 mN. The fracture toughness (K_{IC}) was evaluated from the obtained Vickers hardness and lengths of cracks propagated from four corners of Vickers indentation mark. The thermal expansion was measured by a dilatometer in the temperature range between room temperature and 473K in an argon atmosphere, with the heating rate 5 K/min. The average linear thermal expansion coefficient, α_{ave}, was calculated from the equation 2.27.

4.2.3 Results and Discussion

The microstructure of the $Sb_{1.6}Bi_{0.4}Te_3$_Au polycrystalline bulk samples were investigated by FE-SEM, TEM, and HAADF-STEM in chapter 4.1. These nanoparticles form a great number of interfaces between the nanoparticles and $Sb_{1.6}Bi_{0.4}Te$ matrix phase which can impede the movement of dislocations. Thus, the *H* is expected to increase for the $Sb_{1.6}Bi_{0.4}Te_3$_Au composite.

Figure 4.20(a) show the *H* of $Sb_{1.6}Bi_{0.4}Te_3$ without and with Au and $AuTe_2$ nanoparticles. The *H* of $Sb_{1.6}Bi_{0.4}Te_3$_Au was larger than that of $Sb_{1.6}Bi_{0.4}Te_3$ in the whole measured ranges. And the Vickers hardness (H_V) value (indicated by open marks) measured at 980 mN is almost corresponding to the value of measured by micro indentation hardness method. When the load of 980 mN was pressured on the $Sb_{1.6}Bi_{0.4}Te_3$_Au and $Sb_{1.6}Bi_{0.4}Te_3$, the *H* showed 1.66 GPa and 1.42 GPa respectively. These values are much higher than that of single crystalline bulk sample of Bi_2Te_3. (0.6 GPa)[11] This enhanced hardness of $Sb_{1.6}Bi_{0.4}Te_3$_Au compared to the $Sb_{1.6}Bi_{0.4}Te_3$ and single crystalline bulk sample of Bi_2Te_3 is considered by two reasons as are listed below:

(i) The both polycrystalline bulk samples of $Sb_{1.6}Bi_{0.4}Te_3$ and $Sb_{1.6}Bi_{0.4}Te_3$_Au showed larger value of *H*, compared to that of single crystalline bulk sample of Bi_2Te_3. This implies that the increased grain boundaries act as pinning points impeding dislocation motion. This phenomenon is more pronounced in the case of high angle grain boundaries. Since the lattice structure of adjacent grains differs in orientation, it requires more energy for a dislocation to change directions and move into the adjacent grain. Moreover, the grain boundary also prevents the dislocations from moving in a continuous slip plane. Impeding this dislocation movement will hinder the onset of plasticity and hence increase the yield strength of the material.[12,13]

(ii) From the results of enhanced *H* of $Sb_{1.6}Bi_{0.4}Te_3$_Au compared to $Sb_{1.6}Bi_{0.4}Te_3$, the Au and $AuTe_2$ nanoparticles into the $Sb_{1.6}Bi_{0.4}Te_3$ matrix would impede the propagation of dislocation efficiently in similar way to precipitation hardening acting,[14] Consequently, it can be clearly concluded that the grain boundary and nanoparticle into the matrix enhance the *H*.

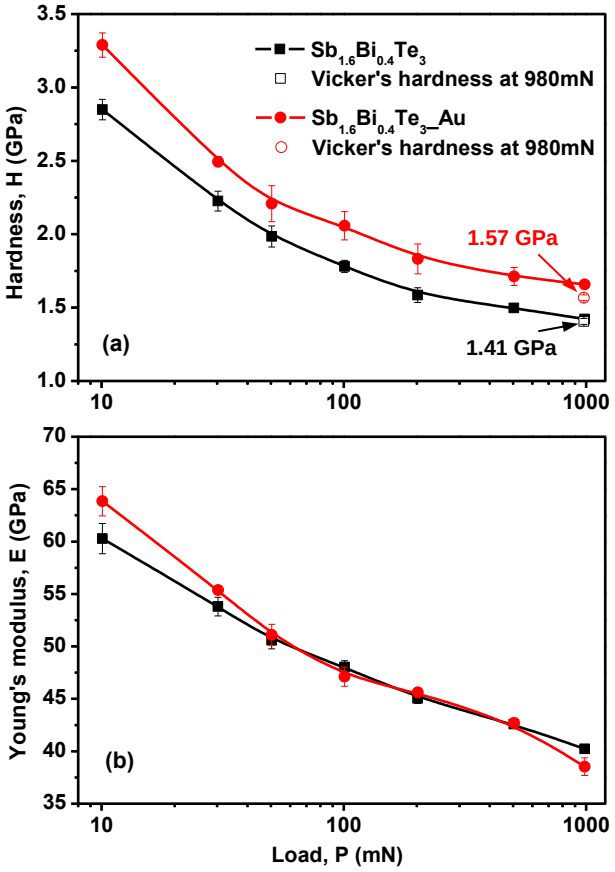

Figure 4.20 (a) Hardness and (b) Young's modulus $Sb_{1.6}Bi_{0.4}Te_3$_Au as compared to those of $Sb_{1.6}Bi_{0.4}Te_3$. Open marks represent the results of measured by Vickers hardness at 980 mN.

Figure 4.20 (b) represents the Young's modulus (E) of both samples as a function of load. As seen in the Figure, when the load is below 50 mN, E of $Sb_{1.6}Bi_{0.4}Te_3$_Au is slightly larger than that of $Sb_{1.6}Bi_{0.4}Te_3$. However, both samples show almost same values above 50 mN. It is well-known that E of polycrystalline materials is dependent on atom interaction, preferential orientation, temperature and stain.[15] It can be described as following equation:

$$E = \frac{k}{a^m} \tag{4.8}$$

where, a is the atom distance represented by the lattice constants in this chapter, k and m are constant. To compare the change in lattice constants of both samples, lattice constants of $Sb_{1.6}Bi_{0.4}Te_3$_Au and $Sb_{1.6}Bi_{0.4}Te_3$ were calculated from the XRD peaks and the results are listed

Table 4.4 Lattice parameters of $Sb_{1.6}Bi_{0.4}Te_3$ and $Sb_{1.6}Bi_{0.4}Te_3$_Au

Crystal system		Hexagonal (space group *R-3m*)	
		$Sb_{1.6}Bi_{0.4}Te_3$	$Sb_{1.6}Bi_{0.4}Te_3$_Au
Lattice parameters	a (nm)	0.42728	0.42736
	b (nm)	0.42728	0.42736
	c (nm)	3.03642	3.03694

in Table 4.4. Although the lattice parameters of $Sb_{1.6}Bi_{0.4}Te_3$_Au are slightly increased because of the impurities (Au and $AuTe_2$ nanoparticles), there are no much effect on the change of *E* above 50 mN of load. However, in the case of increased *E* below 50 mN, there should be other factors (such as preferential orientation of crystalline, non-equilibrium grain boundaries caused by the Au and $AuTe_2$ nanoparticles in the matrix phase,[16] etc.) that might also influence the *E* of $Sb_{1.6}Bi_{0.4}Te_3$_Au.

Figures 4.21(a) and (b) show the indentation images of the H_V test of $Sb_{1.6}Bi_{0.4}Te_3$ and $Sb_{1.6}Bi_{0.4}Te_3$_Au at the load of 980 mN, respectively. The H_V represented in Figure 4.20(a) was calculated from the two diagonals of the indentation left in the surface of the samples after removal of the load. Then arithmetic mean of the two diagonals is measured using a microscope and their average calculated. The area of the sloping surface of the indentation is calculated with following equation:

$$H_V = \frac{F}{S} = \frac{2F\sin\theta/2}{d^2} = 1.8544\frac{F}{d^2} \tag{4.9}$$

where *F* is the load, *d* is the arithmetic mean of the two diagonals, *d1* and *d2*, and θ is the angle of 136 degrees between opposite faces. The H_V calculated using above equation are 1.41 GPa and 1.57 GPa for the $Sb_{1.6}Bi_{0.4}Te_3$ and $Sb_{1.6}Bi_{0.4}Te_3$_Au, respectively, which are in good agreement with the results of micro indentation test as shown in Figure 4.20(a).

The fracture toughness (K_{IC}) was calculated from the obtained H_V and lengths of cracks propagated from four corners of Vickers indentation mark with following equation.[17]

$$K_{IC} = 0.0889\left(\frac{H_v P}{L_i}\right)^{\frac{1}{2}}, \quad L_i = \sum_i^4 a_i \tag{4.10}$$

where *P* and L_i are the Vickers load, and total crack length, respectively. The crack lengths (a_i) are represented in Figure 4.21(a). The measurement was performed ten times at the load of 980mN.

The crack lengths are measured using a microscope and the average value was used for calculating the value of fracture toughness. Among the obtained experimental results, the largest values of the deviation and experimental error such as unclear crack marks were excluded. The results for $Sb_{1.6}Bi_{0.4}Te_3$ and $Sb_{1.6}Bi_{0.4}Te_3$_Au are listed in Table 4.5 and 6, respectively.

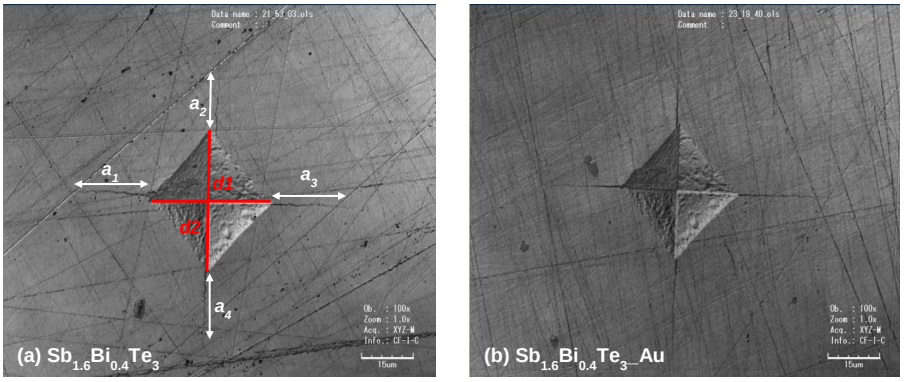

Figure 4.21 Indentation images of (a) $Sb_{1.6}Bi_{0.4}Te_3$ and (b) $Sb_{1.6}Bi_{0.4}Te_3$_Au when the load of 980 mN. *a* and *d* are the length of crack and diagonals, respectively.

Table 4.5. Fracture toughness of $Sb_{1.6}Bi_{0.4}Te_3$

	Li (μm)	*P* (N)	H_V(GPa)	K_{IC} (MPam$^{1/2}$)
No.1	80.27			**0.37**
No.2	84.58			**0.36**
No.3	83.35	0.98	1.41	**0.36**
No.4	78.78			**0.37**
No.5	76.78			**0.38**
Average	80.75			**0.37**
error	3.21			**0.008**

Table 4.6. Fracture toughness of $Sb_{1.6}Bi_{0.4}Te_3$_Au

	Li (μm)	*P* (N)	H_V(GPa)	K_{IC} (MPam$^{1/2}$)
No.1	75.39			**0.40**
No.2	83.27			**0.38**
No.3	78.25	0.98	1.57	**0.39**
No.4	72.45			**0.41**
No.5	81.32			**0.39**
Average	78.14			**0.39**
error	4.36			**0.011**

In the nanocomposite system, it has shown that the main crack propagation was impeded by particles and a damage zone was formed at the crack tip region in the particle filled matrix due to crack diversion of particle/matrix interface.[18] In the present study, the average K_{IC} of $Sb_{1.6}Bi_{0.4}Te_3$_Au is slightly better than that of $Sb_{1.6}Bi_{0.4}Te_3$ as seen in Table 4.5 and 6. I expected to decrease the total crack length (L_i) of $Sb_{1.6}Bi_{0.4}Te_3$_Au because of the Au and $AuTe_2$ nanoparticles in the matrix phase which hamper the main crack propagation. However, the L_i of $Sb_{1.6}Bi_{0.4}Te_3$_Au and $Sb_{1.6}Bi_{0.4}Te_3$ have similar values. The main reason for the enhanced K_{IC} of $Sb_{1.6}Bi_{0.4}Te_3$_Au comes from the high H_V. It is considered that the Au and $AuTe_2$ nanoparticles did not have a great effect on the main crack deflection on the surface of the $Sb_{1.6}Bi_{0.4}Te_3$_Au as described in Figure 4.22. Instead, small crack tip derived from main crack could be hampered by the Au and $AuTe_2$ nanoparticles, therefore the total crack length of $Sb_{1.6}Bi_{0.4}Te_3$_Au measured by a microscope might show almost same values with those of $Sb_{1.6}Bi_{0.4}Te_3$.

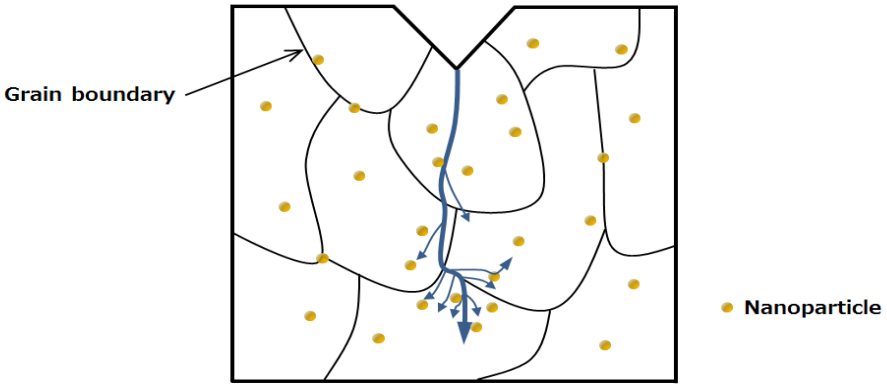

Figure 4.22 Indentation images of (a) $Sb_{1.6}Bi_{0.4}Te_3$ and (b) $Sb_{1.6}Bi_{0.4}Te_3$_Au when the load of 980 mN. *a* and *d* are the length of crack and diagonals, respectively.

Previously, Duan *et al*. has been reported the enhanced K_{IC} by dispersing TiN nanoparticles into $CoSb_3$ skkutterudite.[19] The K_{IC} of $CoSb_3$ + *x* vol.% (*x* = 0.0, 0.3, 0.6, 1.0) nano-TiN particles (50 nm) gradually increased with increasing TiN content mainly due to the deflection of crack propagation by nanoparticles. The K_{IC} of nanocomposite were improved by 40 % for the *x* = 1.0 sample, compared with the TiN-free sample. In the present study, the average nanoparticle size and vol. % in $Sb_{1.6}Bi_{0.4}Te_3$_Au were about 25 nm and 1.0 %, respectively, and the K_{IC} of $Sb_{1.6}Bi_{0.4}Te_3$_Au was enhanced only 7 % which is relatively small, compared to that of $CoSb_3$ + 1.0 vol.% nano-TiN particles sample. From the result, it can be concluded that the particle size in the matrix would have more influence on the K_{IC}.

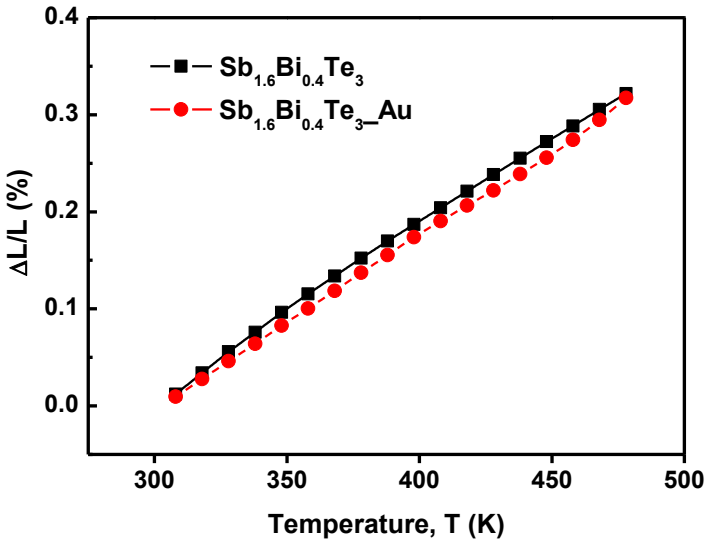

Figure 4.23 Thermal expansion of $Sb_{1.6}Bi_{0.4}Te_3$ and $Sb_{1.6}Bi_{0.4}Te_3$_Au obtained from the dilatometer measurements.

The thermal expansion data obtained by using the dilatometer are shown in Figure 4.23. The thermal expansion curves of both $Sb_{1.6}Bi_{0.4}Te_3$ and $Sb_{1.6}Bi_{0.4}Te_3$_Au increased linearly with increasing temperature. In the temperature range from 308 to 478 K, the linear α_{ave} was calculated based on Equation 2.27, and the results are summarized in Table 4.7, together with reference data.[20-23] The linear α_{ave} values for $Sb_{1.6}Bi_{0.4}Te_3$ and $Sb_{1.6}Bi_{0.4}Te_3$_Au determined by the dilatometer method were 18.2×10^{-6} and 18.1×10^{-6} K^{-1}, respectively. The thermal expansion values obtained in present study were slightly higher than the values of reference data. One of the reasons of this difference would be the difference of the measurement method and the temperature range in each measurement.

Table 4.7 Linear α_{ave} of $Sb_{1.6}Bi_{0.4}Te_3$_and $Sb_{1.6}Bi_{0.4}Te_3$_Au together with reference data.

No.	Sample	Temperature range	Measurement method	$\alpha(10^{-6}K^{-1})$
1	$Sb_{1.6}Bi_{0.4}Te_3$, (This study)	308~478 K	dilatometer	**18.2**
2	$Sb_{1.6}Bi_{0.4}Te_3$_Au, (This study)	308~478 K	dilatometer	**18.1**
3	Bi_2Te_3, single crystal[20]	300~808 K	dilatometer	15.0
4	Bi_2Te_3, single crystal[21]	1.2~600 K	X-ray	16.7
5	Bi_2Te_3, polycrystalline[22]	273~850 K	dilatometer	12.2
6	Bi_2Te_3, polycrystalline[23]	363~843 K	dilatometer	13.8

As I already mentioned in chapter 4.2.1, the comparison of thermal expansion coefficient (TEC) between the TE materials and the interconnect copper in the TE module is very important. According to the report of Furukawa,[24] they synthesized the TE module consisted of CoSb-based skutterudite as a TE legs and the copper as an interconnect. The mismatch of TEC between them was about 32 ~ 39%. The TE module was broken in 1 hour at 823 K due to the mismatch of TEC at the interface. To prevent this problem, they made a new material having a similar TEC with the CoSb-based skutterudite, a high Young' s modulus and hardness. These materials were inserted between the TE legs and interconnect. As a result, the mismatch of TEC between this material and TE leg was reduced to 7 ~ 8 %, led to the stability at 823 K over 8000 hours. Table 4.8 showed the mechanical properties of copper, $Sb_{1.6}Bi_{0.4}Te_3$ and $Sb_{1.6}Bi_{0.4}Te_3$_Au. As listed in Table 4.8, the mismatch of TEC between copper and $Sb_{1.6}Bi_{0.4}Te_3$ was about 33 %, meaning that it could be unstable in the TE module under heating and cooling cycles from the basis of the Furukawa's research. However, the $Sb_{1.6}Bi_{0.4}Te_3$_Au shows a lower value of TEC compared to that of $Sb_{1.6}Bi_{0.4}Te_3$. This reduced TEC is considered to be caused by the discrepancy of thermal expansion coefficient between the nanoparticle and matrix phase. As a result, the mismatch of TEC between copper and $Sb_{1.6}Bi_{0.4}Te_3$ was reduced to about 5 % due to the effect of the Au and $AuTe_2$ nanoparticles. Therefore, it can be concluded that the Au and $AuTe_2$ nanoparticles in the $Sb_{1.6}Bi_{0.4}Te_3$ matrix have a great effect on decreasing the TEC of $Sb_{1.6}Bi_{0.4}Te_3$, led to the stability in the TE module.

Table 4.8 Mechanical properties of copper, $Sb_{1.6}Bi_{0.4}Te_3$ and $Sb_{1.6}Bi_{0.4}Te_3$_Au

		α ($\times 10^{-6}$ K^{-1}) at RT	H_V (GPa)	Young's modulus, E (GPa)
Interconnect	Copper	16.5	0.39	110-128
TE materials (present study)	$Sb_{1.6}Bi_{0.4}Te_3$	21.9	1.41	64
	$Sb_{1.6}Bi_{0.4}Te_3$_Au	17.4	1.57	61

4.2.4 Conclusion

In this chapter, the effect of Au and $AuTe_2$ nanoparticles into the $Sb_{1.6}Bi_{0.4}Te_3$ on the mechanical properties such as hardness, Young's modulus, fracture toughness, and thermal expansion was evaluated. The hardness and fracture toughness of $Sb_{1.6}Bi_{0.4}Te_3$_Au increased by impeding the propagation of dislocation and crack, which were achieved about the 11 % and 7 % increased values. However, Young's modulus $Sb_{1.6}Bi_{0.4}Te_3$_Au showed almost same values because the nanoparticles have not remarkably influenced on the interatomic bonding in the $Sb_{1.6}Bi_{0.4}Te_3$ structure. The TEC of $Sb_{1.6}Bi_{0.4}Te_3$_Au close to the interconnect, copper meaning that the TE module could be stable when the $Sb_{1.6}Bi_{0.4}Te_3$_Au was used due to the reduced mismatch of TEC between them.

From the basis of these results, the nanoparticles incorporated in matrix phase have been proven to be effect on the enhancement not only of TE properties but also mechanical properties. And the one of the most serious crack problem at the interface caused by the mismatch of TEC between copper and $Sb_{1.6}Bi_{0.4}Te_3$ in the TE module could be improved by the Au and $AuTe_2$ nanoparticles.

4.2.5 References

1) E. Hatzikraniotis, K. T. Zorbas, I. Samaras, T. Kyratsi, and K. M. Paraskevopoulos, Journal of Electronic Materials **39**, 2112 (2009).
2) M. T. Barako, W. Park, A. M. Marconnet, M. Asheghi, and K. E. Goodson, 13th IEEE Itherm Conference (2012).
3) G. Li, K. R. Gadelrab, T. Souier, P. L. Potapov, G. Chen and M. Chiesa, Nanotechnology **23**, 065703 (2012).
4) O. Yamashita, S. Tomiyoshi, and K. Makita, J. Appl. Phys. **93**, 368 (2003).
5) J. Jiang, L. Chen. Q. Yao, S. Bai, and Q. Wang, Mater. Chem. Phys. **92**, 39 (2005).
6) V. Zemskov, A. Belaya, U. Beluy, and G. Kozhemyakin, J. Cryst. Growth **212**, 161 (2000).
7) J. Drabble and C. Goodman, J. Phys. Chem. Solids **5**, 142 (1958).
8) X. Zao, X. Ji, Y. Zhang, T. Zhu. J. Tu, and X. Zhang, Appl. Phys. Lett. **86**, 062111 (2005).
9) Y. Cao, X. Zhao, T. Zhu, X. Zhang, and J. Tu, Appl. Phys. Lett. **92**, 143106 (2008).
10) L. D. Zhao, B. P. Zhang, J. F. Li, M. Zhou, W. S. Liu, and J. Li, J. Alloys Compd. **455**, 259 (2008)
11) S. Augustine, and E. Mathai, Mater. Charact. **52**, 253 (2004).
12) N. Hansen, Scr. Mater. **51**, 801 (2004).
13) M. Furukawa, Z, Horita, M. Nemoto, R. Valiev, and T. Langdon, Acta Mater. **44**, 4619 (1996).
14) R. E. Smallman, and A. Ngan, Physical Metallurgy and Advanced Materials (Amsterdam: Elsevier 2007)
15) E. Robert, and Newnham, Structure–property relations, Springer (1975).
16) R.Z. Valiev, E.V. Kozlov, Yu.F. Ivanov, J. Lian, A.A. Nazarov, and B. Baudelet, Acta Metal. Mater. **42**, 2467 (1994).
17) D. K. Shetty, I.G. Wright, P.N. Mincer, and A.H. Clauer, J. Mater. Sci. **20**, 1873 (1985).
18) J. T. Han, and K. Cho, J. Mater. Sci. **41**, 4239 (2006).
19) B. Duan, P. Zhai, P. Wen, S. Zhang, L. Liu and Q. Zhang, Scripta Materialia **67**, 372 (2012).
20) K. N. R. Taylor, Br. J. Appl. Phys. **12**, 717 (1961).
21) J. O. Barnes, et. al, Phys. Lett. A **46** 317 (1974)
22) A. S. Timoshin, et. al, Izv. Akad. Nauk. SSSR. Neorg. Mater. **24** 1286 (1988)
23) S. B. Evgen'ev, Candidate's Dissertation in Technical Science, Moscow; Moscow Institute of Steel and Alloys, 1967.
24) T. Ochi et al., Material research laboratory, R&D division, Furukawa Co., Ltd, ICT (2013).

CHAPTER V

Summary

The main purpose of this thesis was broadly classified into three categories.

i) Investigation of effect of Ag ion conduction in Ag_2Te on the phonon scattering.

ii) Enhancement of TE properties for $Sb_{1.6}Bi_{0.4}Te_3$ by reducing lattice thermal conductivity.

iii) Evaluation of mechanical properties for Ag_2Te and $Sb_{1.6}Bi_{0.4}Te_3$.

First, the ion conductivity of Ag_2Te increased about 10^2 times after the phase transition at around 420 K. However, electronic contribution dominates over the ionic contribution even if the ion conductivity is increased after the phase transition. Ag_2Te is considered an electronic conductor (with the charge carriers being electrons or holes) rather than ion conductor. As a result, it is concluded that the increased ion conductivity has not remarkably influenced on the formation of Frenkel defect or on increasing anharmonicity of lattice vibration that is closely associated with the phonon scattering, therefore the lattice thermal conductivity of β–phase showed no reduction.

Second, the $Sb_{1.6}Bi_{0.4}Te_3$– Au nanocomposite was synthesized by a combined method of γ-ray irradiation, ball-milling, and hot-pressing. Through these synthesizing methods, nano-sized Au particles were successfully dispersed in the $Sb_{1.6}Bi_{0.4}Te_3$ matrix uniformly without aggregation. Although the Au reacted with the Te during hot-pressing process and led to the formation of $AuTe_2$, the Au and $AuTe_2$ particles sustained their nano-size in the $Sb_{1.6}Bi_{0.4}Te_3$ matrix. These nanoparticles scattered phonons effectively, resulted in the reduction of lattice thermal conductivity, thereby enhancement of *ZT*. The γ-ray irradiation which is synthesized nanocomposite is proven to be effective on the phonon scattering. However, this method is proposed to be applied to TE materials, which do not contain the Te element, for avoiding the formation of second phase then both the increase of power factor and decrease of lattice thermal conductivity are expected to be achieved simultaneously and also further enhanced *ZT*.

Lastly, for reducing the thermal expansion of Ag_2Te, Te site was substituted by I (iodine) in the Ag_2Te system. The average linear thermal expansion coefficient of Ag_2Te was significantly decreased about 48 % and 36 % for the $Ag_2Te_{0.9}I_{0.1}$ and $Ag_2Te_{0.8}I_{0.2}$ in the measured temperature range, respectively due to the effect of Ag-I (iodine) bonding having a negative thermal expansion. And as for $Sb_{1.6}Bi_{0.4}Te_3$_Au, the hardness was enhanced about 14 % in which Au and $AuTe_2$ nanoparticles would impede the propagation of dislocation, led to the improvement of harness. From the basis of these results, it can be concluded that the reduction of linear thermal expansion coefficient and improvement of hardness for Ag_2Te and $Sb_{1.6}Bi_{0.4}Te_3$_Au were fulfilled the requirements when utilizing these materials in TE device.

RESEARCH ACHIEVEMENTS

List of Publications

Research Articles

1. Thermal expansion and melting temperature of the half-Heusler compounds: *M*NiSn (*M* = Ti, Zr, Hf).
   Journal of Alloys and Compounds **489**, 328-331 (2010).
   Do-young Jung, Ken Kurosaki, Chang-eun Kim, Hiroaki Muta, and Shinsuke Yamanaka.

2. Effect of phase transition on the thermoelectric properties of Ag_2Te.
   Materials Transaction **53**, 1216-1219 (2012).
   Do-young Jung, Ken Kurosaki, Hiroaki Muta, and Shinsuke Yamanaka.

3. Thermoelectric properties of Au nanoparticle-supported $Sb_{1.6}Bi_{0.4}Te_3$ synthesized by a γ-ray irradiation method.
   Physica Status Solidi (B) (in pressed).
   Do-young Jung, Ken Kurosaki, Satoshi Seino, Manabu Ishimaru, Kazuhira Sato, Yuji Ohishi, Hiroaki Muta, and Shinsuke Yamanaka.

Other Research Article

1. Effect of periodicity of the two-dimensional vacancy planes on the thermal conductivity of bulk Ga_2Te_3.
   Phys. Status Solidi RRL **3**, 221-223 (2009).
   Chang-eun Kim, Ken Kurosaki, Manabu Ishimaru, **Do-young Jung**, Hiroaki Muta, and Shinsuke Yamanaka.

List of Presentations

International Conference

1. Effect of silver ion conduction on the thermoelectric properties of Ag_2Te.
   International Conference on Thermoelectrics, Aalborg, Denmark, July 9-12, (2012).
   Do-young Jung, Ken Kurosaki, Yuji Ohishi, Hiroaki Muta, and Shinsuke Yamanaka.

2. Change in the thermoelectric properties of Ag_2Te before and after the phase transition.
   IUMRS-International Conference on Electronic Materials, Yokohama, Japan, September 23-28, (2012).
   Do-young Jung, Ken Kurosaki, Yuji Ohishi, Hiroaki Muta, and Shinsuke Yamanaka.

3. Effect of silver ion conductivity on thermoelectric properties of Ag_2Te.
   Powder Metallurgy World Congress, PM2012 Yokohama, Yokohama, Japan, October 14-18, (2012).
   Do-young Jung, Ken Kurosaki, Yuji Ohishi, Hiroaki Muta, and Shinsuke Yamanaka.

Domestic Conference

1. Thermal expansion of the half-Heusler type *M*NISn (*M* = Ti, Zr, Hf).
   Annual Meeting of the Thermoelectrics Society of Japan, Tohoku University, Sendai, Japan, August 10-11, (2009).
   Do-young Jung, Ken Kurosaki, Chang-eun Kim, Hiroaki Muta, and Shinsuke Yamanaka.

2. Thermal expansion and melting temperature of half-Heusler type *M*NiSn (*M* = Ti, Zr, Hf)
   Japan Society of Powder and Powder Metallurgy, Nagoya, Japan, October, (2009).
   Do-young Jung, Ken Kurosaki, Chang-eun Kim, Hiroaki Muta, and Shinsuke Yamanaka.

3. Effect of ionic conduction on the thermoelectric properties of Ag_2Te.
   Annual Meeting of the Thermoelectrics Society of Japan, Tokyo University, Tokyo, Japan, August 19-20, (2010)
   Do-young Jung, Ken Kurosaki, Yuji Ohishi, Hiroaki Muta, and Shinsuke Yamanaka.

ACKNOWLEDGEMENTS

A man's mind plans his way, but the Load directs his step and makes them sure.

(Proverbs 16 : 9)

First, I thank the Load for the talents He has bestowed upon me. The Load will be with me forever, and I will follow the Load for everlasting. I hope what the Load would want is to be what I want, and what the Load would see is to be what I see.

I would like to give many thanks to my Professor Dr. Shinsuke Yamanaka for his support and guidance in may research. He always encouraged and believed in me when I was in trouble or sick last 2011 year. It is a great pleasure to be his student.

I hereby express my appreciation to my committee member, Professor Dr. Takao Yamamoto, Associate Professor Dr. Hiroshi Nishikawa for the precious suggestion.

I would like to greatly express my sincere gratitude to Associate Professor Dr. Ken Kurosaki for his informative suggestions, encourage when I had a hard time in the research, and he went out of his way to help me. I think it is very lucky I was able to study under Dr. Ken Kurosaki.

I also would like to thank to Assistance Professor Dr. Hiroaki Muta, Assistance Professor Dr. Yuji Ohishi and Dr. Yoshinobu Miyazaki for great advice when my research could not progress. I am very thankful to Dr. Yusufu Aikebaier for kind discussion and support of experiment.

I am very grateful to Dr. Satoshi Seino for the devoted help in the preparation of samples for γ-ray irradiation and kind discussion or suggestion, and Dr. Takao Kojima for carrying out the γ-ray irradiation for many times, and Dr. Manabu Ishimaru for the helpful investigation on the transmission electron microscopy (TEM) and Dr. Kazuhira Sato for the decisive investigation on the high angle annular dark-filed (HAADF) scanning transmission electron microscopy (STEM) and energy dispersive X-ray (EDX) spectroscopy line scan analysis.

I would especially like to thank to office administrator Ms. Kazuko Terasoma for her backup in everything. I am very appreciating to Ms. Kazuko Terasoma.

I do like to express my great thanks to Mr. Donghun Kim and Mr. Seongho Choi and Mr. Guanghe Lee. Mr. Kim is my best friend and we went through a hard and dark time together, especially last 3 months. I hope he have a wonderful time with his lovely son, Ryeonho, and his adorable wife in Korea. Mr. Choi gave me unexpectable sparking idea and food. I really

appreciate to him. Mr. Lee is Chinese. He gave me a burst of laughter always. We were crazy about playing tennis at once. Someday, I really enjoy playing tennis again with all members inviting Dr. Yonghee Lee.

I do appreciate Mr. Shuto and Mr. Kumagai. I talked to them comfortably not only thermoelectrics but also many things about girls.., girls...., girls..... and so on. They helped my life in Yamanaka laboratory. Arigato!

My thankfulness is also expanded to all members in Yamanaka laboratory for cooperation, kind friendship and helping to understand Japanese culture. I will never forget to spend time in Yamanaka laboratory.

Finally, I do like to express my special thanks to my family in my heart. My family always trusts me whatever I do. They have given me counsel and an understanding ear throughout the years. I will do my best to live my life for replying their kindness.

June 2013

Doyoung Jung